MICROWAVE AND MILLIMETER WAVE IMAGING USING SYNTHETIC APERTURE FOCUSING AND HOLOGRAPHICAL TECHNIQUES

by

JOSEPH TOBIAS CASE

A THESIS

Presented to the Faculty of the Graduate School of the

UNIVERSITY OF MISSOURI-ROLLA

In Partial Fulfillment of the Requirements for the Degree

MASTER OF SCIENCE IN ELECTRICAL ENGINEERING

2005

Approved by

Dr. Reza Zoughi

Dr. R. Joe Stanely

Dr. Paul E. Parris

ABSTRACT

Microwave and millimeter wave nondestructive testing and evaluation (NDT&E) methods have shown great potential for determining material composition in composite structures, determining material thickness or debond thickness between two layers, and determining the location and size of flaws, defects, and anomalies. The same testing methods have also shown great potential to produce relatively high-resolution images of voids inside Spray On Foam Insulation (SOFI) test panels using real focused methods employing lens antennas. An alternative to real focusing methods are synthetic focusing methods. The essence of synthetic focusing is to match the phase of the scattered signal to measured points spaced regularly on a plane. Many variations of synthetic focusing methods have already been developed for radars, ultrasonic testing applications, and microwave concealed weapon detection. Two synthetic focusing methods were investigated; namely, a) frequency-domain synthetic aperture focusing technique (FD-SAFT), and b) wide-band microwave holography. These methods were applied towards materials whose defects were of low dielectric contrast like air void in SOFI. It is important to note that this investigation used relatively low frequencies from 8.2 GHz to 26.5 GHz that are not conducive for direct imaging of the SOFI. The ultimate goal of this work has been to demonstrate the capability of these methods before they are applied to much higher frequencies such as the millimeter wave frequency spectrum (e.g., 30-300 GHz).

ACKNOWLEDGMENTS

I would like to thank the NASA Marshall Space Flight Center for their funding for this work through a Cooperative Agreement and the University of Missouri-Rolla for the Chancellor's Fellowship. I would also like to thank:

- Everybody at the *amntl* for an atmosphere conducive to research and friendship.
- Dr. Joe Stanley and Dr. Paul E. Parris for serving on my committee.
- Greg Cartee and Trung Dam for providing me a place to live in Huntsville.
- Mr. James L. Walker for many insightful discussions on the nature of SOFI.
- Josh Robbins for making many scans that provided me with initial understanding.
- My "secondary" boss, Frank Hepburn, who provided the equipment and the challenge to succeed as I helped begin to build the microwave lab at Marshall.
- Mr. Joe Barnes for his great taste in music and his terrific attitude. We made a great team and without him the scanner would have been impossible.
- Dr. Reza Zoughi, my advisor and friend. I thank him for his careful attention to detail, support towards my research, and the support for my well-being.
- Mr. Gabe Freiburger for our many deep conversations about each of our projects, life, and much more. I wish you the best of fortune in all your endeavors.
- Dad, Mom, Gabe, Matt, Tabi, little Keira, and family for their support, positive you-can-do-it attitudes, cookies, and love.
- Last but not least, God, who already knows what I am going to thank him for… Everything.

TABLE OF CONTENTS

LIST OF ILLUSTRATIONS

LIST OF TABLES

1. INTRODUCTION

1.1. BACKGROUND OF MICROWAVE NDT&E

Microwave and millimeter wave nondestructive testing and evaluation (NDT&E) methods have shown great potential for determining material composition in composite structures. For instance, these NDT&E methods have been applied to concrete and mortar specimens to quantify the mixture properties [1, 2]. They may also be applied to stratified media to determine material thickness or debond thickness between two layers [3].

The same microwave and millimeterwave testing methods may be used to detect and locate flaws, defects, and anomalies. This is because the physical structure and its interior may reflect microwaves at dielectric interfaces pertaining to a flaw. Microwave NDT&E methods have been used to detect chlorides [4-7] and determine the effects of loading [8-10] on concrete and mortar structures. These methods have also been applied to the detection of grout in masonry and the detection of corrosion under paint [11, 12].

The same testing methods have also shown great potential to produce relatively high-resolution images of voids inside Spray On Foam Insulation (SOFI) test panels using real focused methods employing lens antennas [13, 14]. For such a case, defects can be localized in the two dimensional space of a raster scanned image. Real focused methods require relatively high frequency to provide for the use of a smaller lens and the required increase in resolution, namely operating in V-band (50-75 GHz), W-band (75-110 GHz), or higher. Also, for raster scanning it is necessary to increment the scanner sampling points on the order of the footprint or beam spot-size.

An alternative to real focusing methods are synthetic focusing methods. The essence of synthetic focusing is to match the phase of the signal originating at an

arbitrarily located target to measured points spaced regularly on a plane [15]. For a signal originating at that target processed signals add constructively and for all surrounding points they add destructively, consequently providing significant spatial discrimination and resulting in a high-resolution image.

At times it is more advantageous to use synthetic focused methods as opposed to real focused methods, and vice versa. A summary of the advantages and disadvantages of both methods are listed in Table 1.1. In observance of the advantages and disadvantages of synthetic focusing, this thesis investigates synthetic focusing methods and its use on materials whose defects are of low relative dielectric contrast, such as an air void in SOFI.

After a thorough literature search, two synthetic focusing methods were selected, namely; a) frequency-domain synthetic aperture focusing technique (FD-SAFT), and b) wide-band microwave holography [16, 17]. Many variations of synthetic focusing methods have already been developed for radars, ultrasonic testing applications, and microwave concealed weapon detection. How the aforementioned synthetic focusing methods were chosen is best described in the summary of the literature search, which documents the evolution of the preliminary research.

1.2. LITERATURE SEARCH

The two main topics of the literature search were real focusing techniques and synthetic focusing techniques that would yield images with higher spatial resolution. Also, it was important to satisfy the following two specific conditions: 1) detection of small signals for low dielectric contrast cases and 2) detection in the far-field.

Table 1.1. Advantages and disadvantages to real and synthetic focusing imaging methods.

Real Focusing Imaging	**Synthetic Focusing Imaging**
Advantages	**Advantages**
• No image processing necessary • Coherent data not necessary	• Cheaper probe construction • May provide for full three dimensional representation • Focal point can be moved synthetically • May be able to produce the same resolution with larger sampling increment
Disadvantages	**Disadvantages**
• More expensive probe construction • Provides poor range resolution • Must relocate focal point manually • Lens diameter is large at lower frequencies • Must increment sampling on the order of the footprint/spot-size	• Coherent data required • May require broad band measurements • Image decipherable only after processing

The research into real focusing techniques incorporated topics such as dielectric lenses [18, 19], artificial lenses [20, 21], negative refractive index lens [22-25], diffractive lenses [26, 27], reflectors [28, 29], and dielectric loaded horns [30- 32]. The

most difficult part of real focusing techniques is the manufacturing of the lens or the reflector, which takes time, precision, and manufacturing resources. This is especially true for artificial, negative refractive index, and diffractive lenses. Microwave microscopy was also researched, which provides very fine spatial resolution. However, these techniques utilize the near-field properties of a probe whereas the object under detection would commonly be in the far-field of the probe [33-35].

The research into mathematical methods of increasing image resolution included topics such as arrays [36-40], synthetic aperture focusing techniques (SAFT) [16, 41-45], synthetic aperture radar (SAR) [46], reconstruction techniques [47, 48], and holography [17, 49, 50]. Arrays have a lower theoretical resolution at the focal point compared to SAFT and so they were not investigated further. Reconstruction techniques were not adequate due to the low dielectric contrast nature of the application and the inclusion of noise in the measurements. SAR was quickly dismissed in favor of SAFT due to the nature of the available measuring equipment. SAR is performed from a moving probe with respect to a stable target where not only the time shift of the received signal is used but also the Doppler shift, which requires specialized time domain equipment. The equipment available for this thesis did not include such measurement setups that could incorporate SAR. However, the equipment available could support a specific method of SAFT called frequency-domain synthetic aperture focusing technique (FD-SAFT) [16]. This proved easy to implement and provided successful initial results. However, FD-SAFT does not provide range resolution. Consequently, methods of holography were also pursued, and one method that particularly matched the frequency swept complex dataset was wide-band microwave holography [17]. Therefore, this thesis focuses primarily on

the use of FD-SAFT and wide-band microwave holography on low contrast defects in dielectric materials.

1.3. OVERVIEW OF SPRAY ON FOAM INSULATION (SOFI)

The material used to provide low contrast defects in a media was spray on foam insulation (SOFI), used as part of the Thermal Protection System of the Space Shuttle's external tank, which is mainly composed of a lightweight aluminum alloys. SOFI is used to insulate the external tank of the Space Shuttle in order to maintain the storage temperature of the fuel, liquid hydrogen and liquid oxygen, at cryogenic temperatures and to help keep other regions warm enough so that ice and frost do not form on the surface of critical sections [51].

SOFI is sprayed onto the aluminum body of the external tank in successive layers where the aluminum body is referred to as the substrate. The SOFI is only allowed to partially cure before the next layer is applied forming what is referred to as a knit-line between successive layers. During the application process, specific temperatures must be maintained for SOFI consistency. If fresh SOFI is applied to fully cured SOFI, Conathane must be first applied as an adhesion enhancer to improve the bond between the foam layers [51]. For the vast majority of the surface of the external tank, SOFI is applied mechanically resulting in high quality uniform SOFI. However, SOFI must be manually applied to some parts of the external tank due to the complexity of the application and the surrounding structure. For example, consider the bipod struts that join the orbiter and the external tank. In these regions SOFI application may generate internal air voids or debond between SOFI layers or between the aluminum substrate and SOFI [51]. The

presence of an interior small void or debond in SOFI provides for higher internal pressure in the void during the high speed launch and may cause surrounding SOFI to break and dislodge from the tank.

Consequently, during a launch, pieces of the SOFI may break off ranging in size from a few cubic millimeters to thousands of cubic centimeters. Upon breaking off, SOFI decelerates rapidly with respect to the Space Shuttle. Although SOFI disintegrates upon impact, large enough volumes contain enough kinetic energy to severely damage the orbiter. One such piece of SOFI fell from the left bipod ramp of the external tank and struck the reinforced carbon/carbon panels on the wing of the orbiter Columbia at 625 to 840 feet per second [51]. Upon re-entry, the internal structure of the orbiter was left unprotected and caused the loss of the left wing and its inevitable breakup. Therefore, a robust nondestructive testing and evaluation (NDT&E) method is desired that is capable of detecting small voids in SOFI prior to a launch.

1.4. OVERVIEW OF EXTERNAL TANK GEOMETRY

Defects in SOFI may also be accompanied by strong scatterers on the external tank of the Space Shuttle. For this reason, it is necessary to discuss the more complex geometries common to the external tank and understand terms used to refer to these geometries.

Some regions of the external tank of the Space Shuttle are covered with stringers and flange, as shown in Figure 1.1. One such region on the external tank is where either the liquid oxygen tank or the liquid hydrogen tank joins the intertank. The flange must hold these sections of the external tank together [51]. The flange extends around the

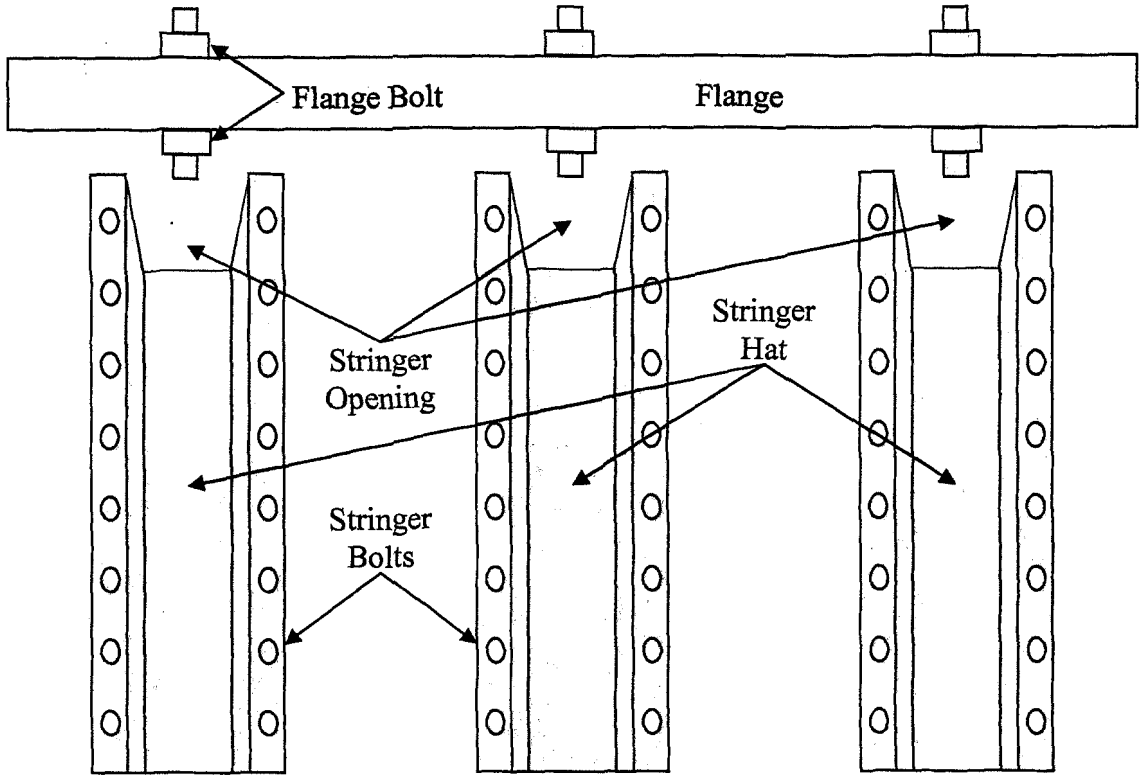

Figure 1.1. Stinger part definitions.

external tank cylindrical sections. Strong flange bolts hold two adjacent sections together and they are spaced regularly around the external tank with the stringers.

Stringers are bolted down longitudinally along the external tank in order to increase the lateral and axial strength of the external tank [51]. Stringers are very long and the cross-section of one is trapezoidal with a narrow top and a wide base. Attached to the base is sufficient material on the sides to bolt the stringer down to the external tank. The top of the stringer is called the hat. The stringers must terminate at the flange and their termination is such that the cut of the stringer starts at the base and moves up and away from the flange bolt. This termination is called the stringer opening.

1.5. CURRENT INVESTIGATION

Two methods of synthetic focusing are presented in this thesis, namely; frequency domain synthetic aperture focusing technique (FD-SAFT) [16] and wide-band microwave holography [17], described in Sections 2 and 3, respectively. It is important to note that this investigation uses relatively low frequencies in X-band (8.2-12.4 GHz), Ku-band (12.4-18 GHz), and K-band (18-26.5 GHz) that are not conducive for direct imaging of the SOFI [13, 14]. However, as will be seen later, when using the image processing algorithms mentioned above, reasonably high resolution images are obtained even at these relatively low frequencies. The ultimate goal of this thesis is to demonstrate the capability of these methods before they are applied to much higher frequencies such as the millimeter wave frequency spectrum (e.g., 30-300 GHz).

The results of frequency-domain synthetic aperture focusing technique (FD-SAFT) is presented in Section 2 [16]. This section gives a summary of the algorithm, the theoretical resolution, and different fundamental experiments that establish the strengths and weaknesses of this image processing method. Results are divided into categories that are also chronological and increasingly test the method with more difficult specimens to analyze.

Section 3 presents the wide-band microwave holography method [17]. This section gives a summary of the immediate benefits of three dimensional representation, the algorithm, the theoretical resolution, and the results. The results are divided into the same categories as FD-SAFT to show the immediate capabilities where FD-SAFT fails.

Section 4 of the thesis summarizes the advantages and disadvantages of both image processing methods and compares and contrasts the two. In addition, a discussion of future work to improve both methods for applications beyond the scope of this thesis is presented.

2. SYNTHETIC APERTURE FOCUSING TECHNIQUE (SAFT)

2.1. INTRODUCTION

Synthetic aperture focusing technique (SAFT) has been primarily used in the field of ultrasonic testing to synthetically focus a single frequency or multiple frequency measurement to a specific focal plane [16, 52]. Extensions of this method may also provide range resolution. In this section, the specific method of narrow-band frequency-domain synthetic aperture focusing technique (FD-SAFT) by Busse is extended to be used with microwave signals, and subsequent experimental data is also presented [16].

One may note the immediate difference between pressure waves and electromagnetic waves, namely pressure waves are not polarized and electromagnetic waves are. For calculation purposes, the sample under test was assumed not to depolarize the incident wave. By assuming this, microwave energy does not transfer from one polarization to another. Additionally, the sample under test was assumed not to disperse the incident wave to or reflect different frequencies differently.

Two other assumptions are made in order to simplify the backward wave propagator, a necessary step taken in FD-SAFT. The first assumption is that only single reflections occur and no multiple reflections exist. Therefore, no compensation is made for a reflection occurring at a target and reflecting off of another. The second assumption is particular to the dielectric, SOFI, that was scanned for internal air voids. It is assumed that SOFI does not significantly delay the wave traveling through it, because the dielectric properties of SOFI and air are quite similar. This assumption allows us to use the existing algorithms with no modification regarding traveling waves through a higher

dielectric. This is valid since SOFI has a permittivity of only 1.05 at X-band (8.2-12.4 GHz) as compared to air with a relative permittivity of 1.00 [14, 53].

Section 2.2 of this section illustrates the measurement setups used to gather the microwave data. Section 2.3 discusses the FD-SAFT algorithm and its theoretical resolution. Section 2.4 illustrates the sensitivity of the algorithm to both frequency and height displacement. Sections 2.5 through 2.9 provide results of several examples demonstrating the performance of FD-SAFT for increasingly complex cases. The first case involves several SOFI cubes in air, for the purpose of verifying the fact that the air-to-SOFI reflection could be detected. The second case is of several flat bottom holes in SOFI carried out for three different configurations serving as evidence of detecting air voids in SOFI. The third case involves twenty flat bottom holes of varying diameters and depths used to test the limitations of the method. The fourth case presents the results of a complex sample that is more representative of the external fuel tank of the Space Shuttle. This sample contains artificial defects including rubber pads and SOFI void inserts. The last case, involves a sample similar to the previous case with the exception of several natural voids intentionally generated by improper spraying of the foam. Section 2.10 summarizes what was learned from all of these cases and describes the advantages and disadvantages of the FD-SAFT algorithm leading to the wide-band microwave holography method discussed in Section 3.

2.2. MEASUREMENT SETUP

The imaging process consisted of raster scanning a sample with an open-ended rectangular waveguide probe, as shown in Figure 2.1. Data was acquired by using a

vector network analyzer where the magnitude, $|\Gamma|$, and phase, ϕ, of the microwave reflection coefficient at the aperture of the waveguide probe were recorded for every data point at a height of h above the sample. If the sample consisted of a defect embedded in a material other than air, the term liftoff was used to refer to the distance of the measurement plane over that material . The step size or scanning increment, Δ, between adjacent measurements was on the order of half of the narrow dimension of the waveguide probe. Two different scanning facilities were used during the course of these experiments as described below.

The first setup was located at the Applied Microwave Nondestructive Testing Laboratory (*amntl*) at the University of Missouri-Rolla. The facilities provided a moving table or fixed head scanner in conjunction with an HP8510C Network Analyzer. The scanning table has the distinct advantage of being able to measure at higher frequencies. This is because the coaxial cables used do not need to be moved in the process of scanning. Such movements may cause magnitude and phase variations in the measured

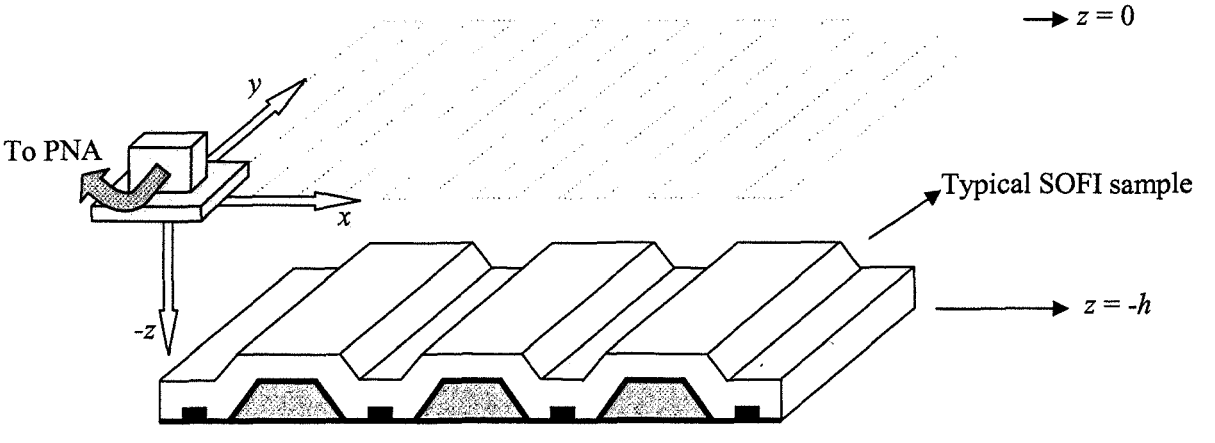

Figure 2.1. Illustration of scanning procedure with open-ended rectangular waveguide probe on an underlying SOFI sample.

signal. However, the highest measurable frequency at this location was 18 GHz. Measurements conducted at this location were either at X-band (8.2-12.4 GHz) or Ku-band (12.4-18 GHz). Measurements were conducted at the highest power available; specifically, 0 dBm. This system did not provide for an automatic, internal compensation for the waveguide-to-air boundary. Instead, the mean of the measured complex reflection coefficient was subtracted after the measurement, as will be explained later.

The second measurement setup was located at the NASA Marshall Space Flight Center in Huntsville, Alabama. This facility provided a moving head or fixed table scanner in conjunction with the Agilent E8361A PNA Series Network Analyzer. The network analyzer at this location is capable of performing coherent measurements up to 325 GHz and has a maximum dynamic range of 94 dB specified up to 67 GHz. However, cables and connectors were not available to support the whole frequency range for scanning. Instead, all measurements at this location were performed at K-band (18-26.5 GHz) with an IF Bandwidth of 10 kHz, which provided a reasonably stable and quick sweep. Measurements were made at the highest power available, typically 0 dBm and later at -6 dBm due to phase instability issues associated with the source. For this measurement setup, internal coherent subtraction of the reflection at the waveguide-to-air boundary was readily available. However, the mean of the reflection coefficient was still subtracted to be consistent with previous measurements as well as to effectively subtract the contribution of the flat metal substrate and make small scatterers more pronounced.

2.3. FD-SAFT ALGORITHM

This section describes the formulation of the narrow-band version of frequency-domain synthetic aperture focusing technique (FD-SAFT) developed by L.J. Busse [16]. This method of FD-SAFT can be described as the synthesis of a large and narrow beam antenna made possible using measurements at regular points on a grid using a real small and broad beam antenna, resulting in in images with high spatial resolution. This is done by matching the phase between the measured points, g, and focused points, s, using the two-way travel phase delays represented by the following exponential terms, see Figure 2.2:

$$s(x_n, y_n : z = -h) = \sum_{i=1}^{4} g(x_m, y_m : z = 0)\exp(j2kR_{mn}), \tag{1}$$

where $k = \omega/c$. However, the above expression is rather simplistic, since FD-SAFT utilizes angular spectrum decomposition as described later [54].

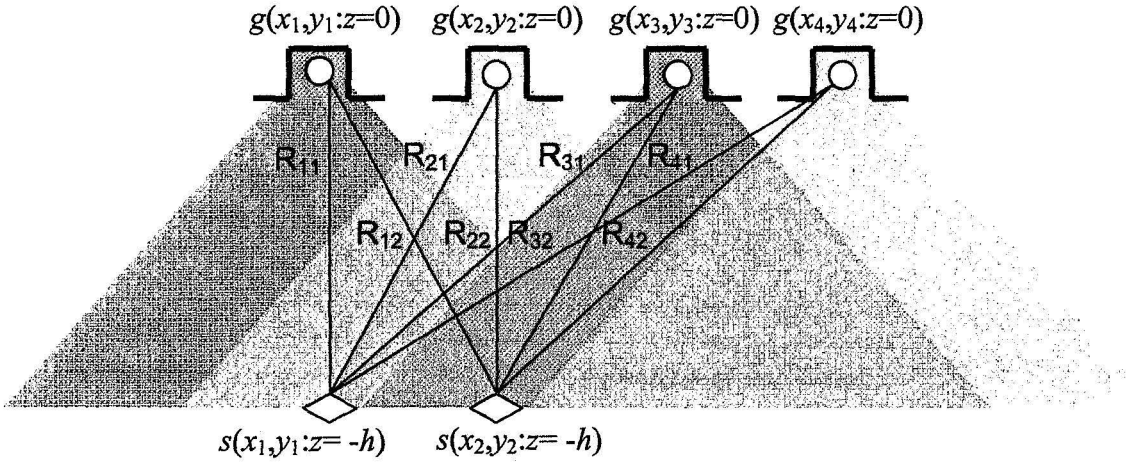

Figure 2.2. Illustration of phase matching for FD-SAFT.

The unprocessed microwave data, g, is a discrete sampling of the full microwave reflection coefficient over a two dimensional array. The reflection coefficient consists of magnitude, $|\Gamma|$, and phase, ϕ, at a single radial frequency, ω. This is measured at $z = 0$ and is contained in:

$$g(x, y : z = 0) \tag{2}$$

such that:

$$0 \le x \le x_{\max} \text{ and } 0 \le y \le y_{\max} \tag{3}$$

where $x_{\max}$ and $y_{\max}$ are referred to as the scanning dimensions along the x-axis and y-axis, respectively (see Figure 2.1). The unprocessed data, g, is sampled at the same interval along the x and y axes at the scanning increment, Δx, which must satisfy the Nyquist sampling rate. Therefore, the phase difference between two sampling points separated by Δx must be less than π. However, the maximum phase difference for a measurement of a scatterer very near the measurement plane is $2k\Delta x$ rather than $k\Delta x$ for a real array. Therefore:

$$\Delta x < \frac{\lambda}{4} \tag{4}$$

where λ is the wavelength corresponding to the radial operating frequency ω. Most systems will not include scatterers this close to the array, thus a sampling increment of $\Delta x = \lambda/2$ is considered practical. The raw data, g, must subsequently be decomposed onto a plane-wave spectrum using the 2D Fast Fourier transform, such that:

$$G(k_x, k_y : z = 0) = FFT_{2D}\{g(x, y : z = 0)\} \tag{5}$$

After performing the 2D Fast Fourier transform, the ranges for k_x and k_y must be centered about $k_x = 0$ and $k_y = 0$, which is assumed hereon. Next, the data is propagated to the plane of $z = -h$ in order to bring the sample under test into focus at this height (see Figure 2.1). This is done by using the two-way backward wave propagator:

$$B(z, \omega) = \exp\left[j2kz\left(1 - \left(k_x/2k\right)^2 - \left(k_y/2k\right)^2\right)\right] \tag{6}$$

The intermediate quantity, G', after applying the backward wave propagator is defined as:

$$G'(k_x, k_y : z = -h) = G(k_x, k_y : z = 0) \times B(z = -h, \omega) \tag{7}$$

The remaining step is to project the data back to spatial coordinates using the inverse 2D Fast Fourier transform; namely:

$$s(x,y:z=-h)=FFT_{2D}^{-1}\{G'(k_x,k_y:z=-h)\} \tag{8}$$

The processed data, $s(x,y:z=-h)$, is now a single frequency high-resolution focused image at height $z=-h$. The spatial resolution of this image is roughly one half of the dimension of the antenna aperture similar to a focused synthetic aperture radar (SAR) for targets far from a large measurement plane but not for targets close to a small measurement plane [15]. A more accurate expression for the spatial resolution is given by:

$$\delta_x \approx \frac{\lambda}{4\sin(\theta_b/2)} \tag{9}$$

where θ_b is either the full beamwidth of the microwave probe or the angle subtended by the measurement plane, whichever is less [17]. Referring to Figure 2.2, the angle subtended by the measurement plane for point $s(x_2,y_2:z=-h)$ is the angle between R_{12} and R_{42}. There is no appreciable range resolution associated with this image processing method, since there is no bandwidth in a single frequency measurement.

Extensions of this method to provide range resolution include averaging multiple frequencies together when the data was distributed either in the spatial or frequency domain. However, neither average improved the image quality especially if the object exceeded the depth of focus [16]. Another method investigate for providing a better focused image was the multiple frequency auto-focusing technique (MF-AFT), which transforms frequency-domain data to the time-domain data and focuses on the largest

reflection available [52]. This method was not pursued since the goal of this investigation was to find small reflections rather than large ones. Despite the lack of range resolution, the benefit of FD-SAFT is that it can significantly increase the spatial resolution associated with a microwave image. Additionally, FD-SAFT requires only a short processing time (fraction of a second), which is made possible by the extensive use of efficient Fast Fourier transform algorithms. Furthermore, upon bringing an image of a defect into focus by varying the height h, that height can be used as an estimate for the depth of the defect.

2.4. SENSITIVITY TO HEIGHT AND FREQUENCY

An attempt was made to understand the sensitivity of the FD-SAFT method to height and frequency. To this end, two 10 mm by 10 mm square rubber pads with a thickness of approximately 2 mm were cut and placed 10 mm apart on an aluminum substrate. The pads were expected to provide a relatively strong reflection compared to SOFI and be easily detectable by the network analyzer. The test was performed in X-band (8.2-12.4 GHz) at a frequency of 12.4 GHz using a power level of 0 dBm and the scanning increment, Δx, was 2.5 mm or approximately one quarter the narrow dimension of the waveguide. The scan was performed over a square region of size w, such that w was 160 mm for this case

The first experiment aimed at investigating the sensitivity of FD-SAFT to the height of the measurement plane. Three different scanning heights, h, were chosen for this experiment: 25 mm, 100 mm, and 200 mm. Two parameters affect the performance of FD-SAFT significantly; namely, 1) measurable power, 2) the maximum available

spatial frequency of the image. The power level of the received signal reflecting off of the pad and back towards the waveguide probe changes as a function of distance. The difference between the signal power levels received from $h = 100$ mm compared to $h = 25$ mm is approximately 24 dB lower. This value is 36 dB comparing $h = 200$ mm and $h = 25$ mm. However, rubber pads were chosen for this experiment so that their reflection would be large, thereby making measurable power level not an issue.

Aside from measurable power, the impact of maximum available spatial frequency must be considered. For a given scan width and height, the maximum measurable spatial frequency along the x-axis is given by:

$$k_{x\max} = 2k\frac{w/2}{\sqrt{(w/2)^2 + h^2}} = 2k\sin(\theta_a/2) \tag{10}$$

such that θ_a is the angle subtending the measurement plane. The above expression assumes that the radiating antenna is isotropic. This is important since FD-SAFT sums over k_x and k_y in the last step of the method, see Equation 8. The summation interval over k_x is $(-k_{x\max}, k_{x\max})$ providing a summation length of $2k_{x\max}$, which is inversely proportional to the resolution along the x-axis as determined in Section 2.3:

$$\delta_x \approx \frac{2\pi}{2k_{x\max}} \tag{11}$$

Therefore, increasing h for a given w will decrease the available spatial frequency content of the image and adversely affect the resolution. For analysis purposes, parameter $\eta = k_{x\max}/2k$ is defined to compare the maximum available spatial frequency to the physical limit for a synthetic array, $2k$, which accounts for two-way propagation. For example, when $\eta = 1$ the spatial resolution reaches the physical limit for FD-SAFT, which is $\lambda/4$, see Equation 9. However, when $\eta = 0.25$ the spatial resolution is λ. Therefore, an image with high η will have a good resolution and an image with low η will have a poor resolution.

The results of the first experiment clearly demonstrate the dependency on height. For the case of h = 25 mm, the unprocessed data consisting of the magnitude of the microwave reflection coefficient, $|\Gamma|$, indicates that two 10 mm by 10 mm square rubber pads are present, but the size and the 10 mm separation of the pads cannot be determined (Figure 2.3a). Figure 2.3b shows the image after FD-SAFT processing where both pads are easily distinguished, and the size and the separation can be determined. In this case, the targets are very close to the measurement plane corresponding to an η of 0.95, and the theoretical resolution for this case is 9 mm (using Equation 9). Note that this example demonstrates the sub-wavelength resolution capability of the method since λ = 24 mm. For h = 100 mm in Figure 2.3c, the unprocessed data shows that the evidence of two samples has disappeared. However, Figure 2.3d shows the image after FD-SAFT processing where both targets are easily recognized as before in Figure 2.3b even though η has reduced to 0.62 and the theoretical resolution for this case is 10 mm, which corresponds to the dimension of separation between the pads. For h = 200 mm in Figure 2.3e, the unprocessed data again shows no indication of two pads and the noise is more

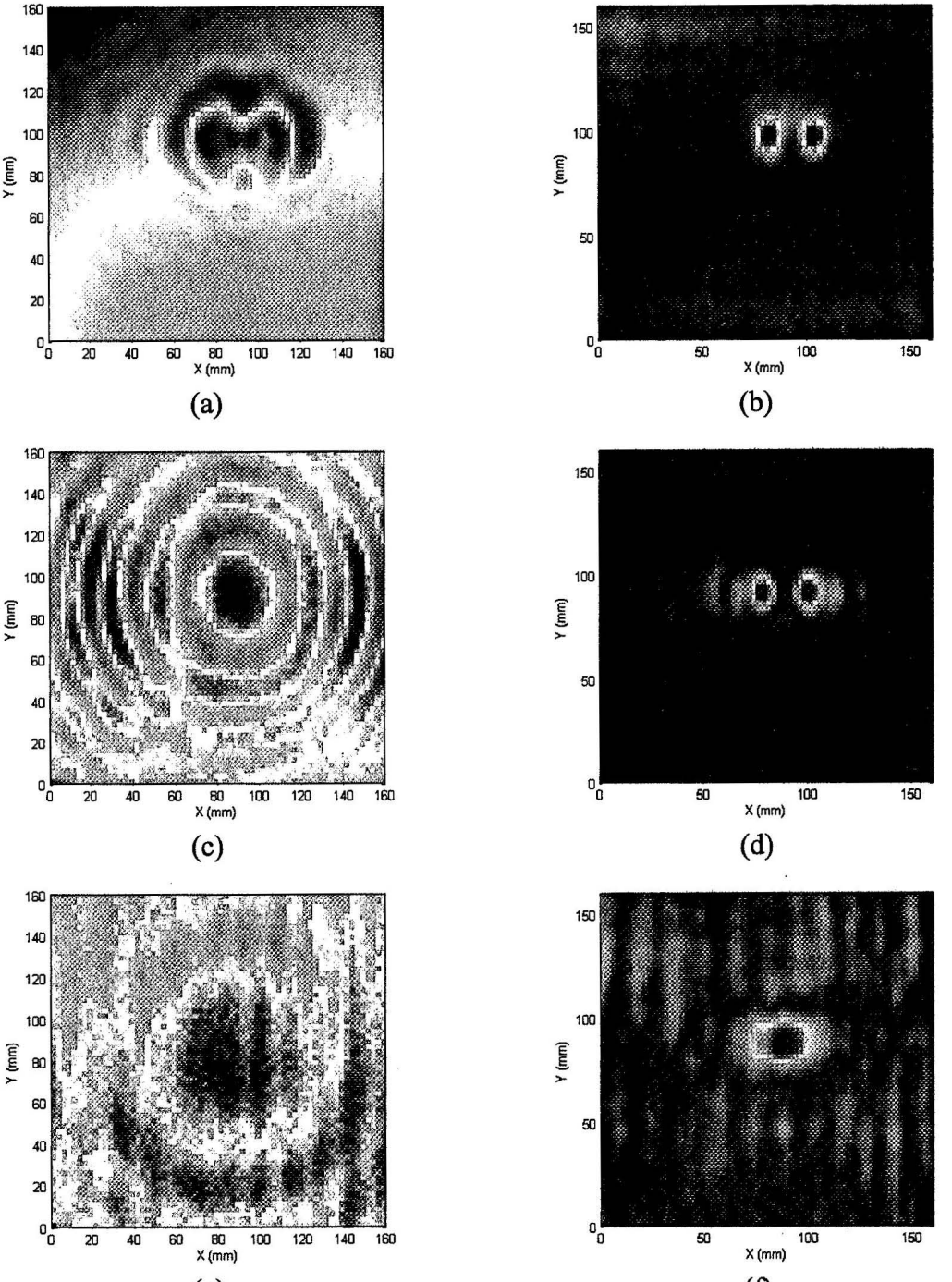

Figure 2.3. Height dependence of FD-SAFT at 12.4 GHz: at 25 mm, (a) |Γ|, (b) FD-SAFT; at 100 mm, (c) |Γ|, (d) FD-SAFT; at 200 mm, (e) |Γ|, (f) FD-SAFT.

noticeable since the signal strength from the pads has decreased due to larger h. In this case, η is 0.37 and the corresponding theoretical resolution becomes 16 mm, which is greater than the separation between the pads. Figure 2.3f confirms this fact and shows that processing can no longer differentiate the two pads on the substrate due to the decrease in resolution. However, one should note that the separation of h = 200 mm is greater than the scanning dimension, 160 mm. If the scanning width w were extended substantially, η would increase and the FD-SAFT image of the two pads would significantly improve. However, these results provide two important lessons: 1) the signal strength may drop below noise for increasing scanning height, 2) the scan setup must provide a the scanned region wide enough for a given height to provide a sufficient value of η.

The second experiment aimed to investigate the influence of the frequency of operation for a given height of h = 100 mm and a scan width of w = 160 mm. The same experimental setup was used with two 10 mm by 10 mm rubber pads separated by 10 mm on an aluminum substrate. The frequency of operation has a direct bearing on the maximum spatial frequency, which has a significant influence on spatial resolution. k_{xmax} remains the same as before. Therefore, as ω increases k_{xmax} also increases, and it is expected that resolution will increase as frequency of operation increases.

The results of this experiment show that as frequency increases resolution improves for a given scan width and height. This experiment was performed for frequencies, f, of 8.2, 10.3, and 12.4 GHz, such that $f = \omega/2\pi$. Figure 2.4a shows the unprocessed data at f = 8.2 GHz (λ =37 mm), and it can be seen that there is no indication of the two pads. The processed image in Figure 2.4b also cannot discriminate

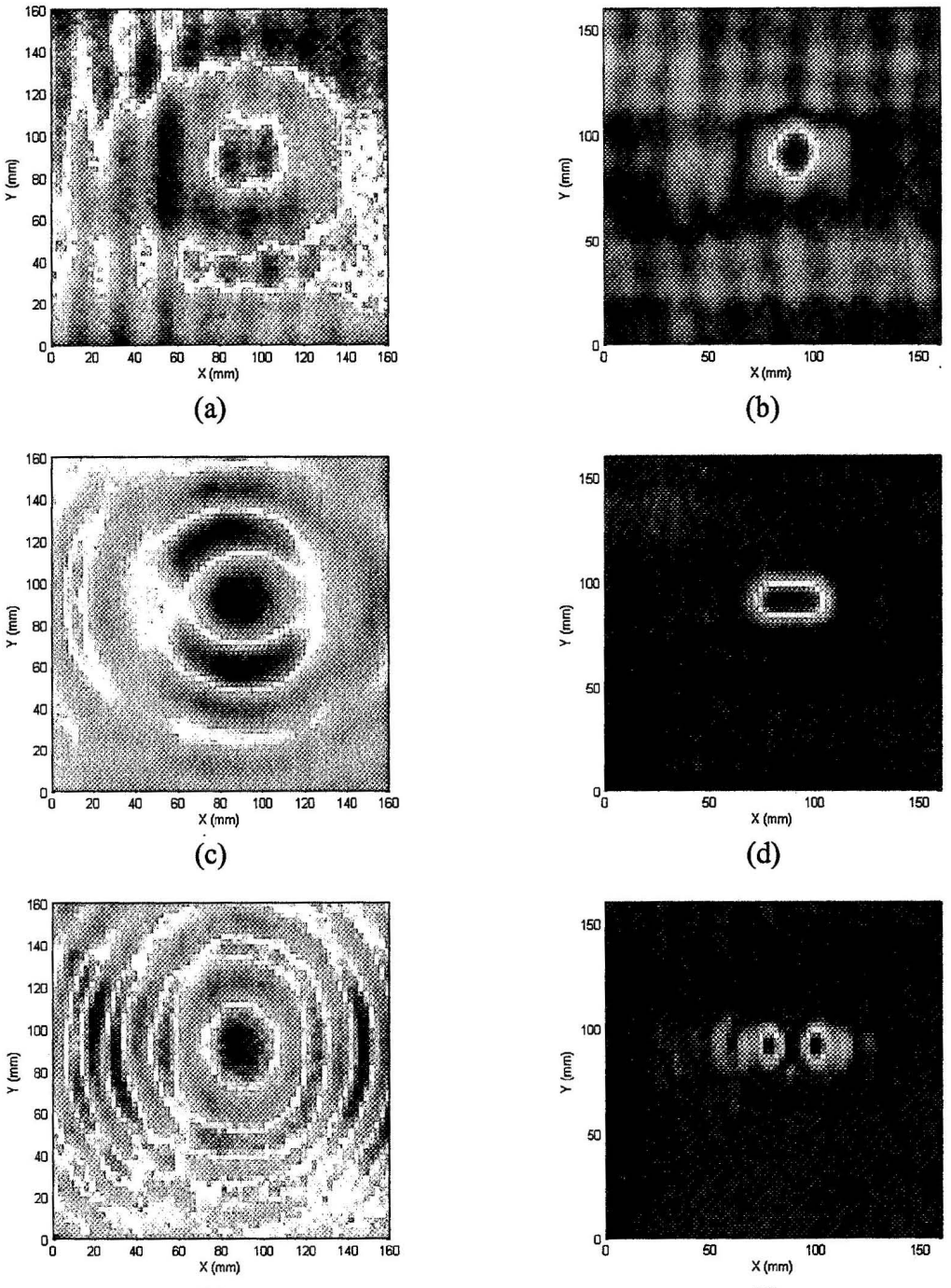

Figure 2.4. Frequency dependence of FD-SAFT: at 8.2 GHz, (a) |Γ|, (b) FD-SAFT; at 10.3 GHz, (c) |Γ|, (d) FD-SAFT; at 12.4 GHz, (e) |Γ|, (f) FD-SAFT.

between the two pads since the theoretical resolution is only 15 mm, which is greater than the dimension of the pads and the separation between them. Figure 2.4c shows the unprocessed data at f = 10.3 GHz (λ =29 mm), midway in the X-band frequency range. FD-SAFT processing in Figure 2.4d still does not show the two individual pads, but discrimination and the image resolution improves with an improved theoretical resolution of 12 mm. Figure 2.4e shows the unprocessed image for f = 12.4 GHz (λ =24 mm), and Figure 2.4f finally shows two pads of equal dimension spaced by 10 mm. Thus, it can be seen that higher frequency of operation provides higher spatial resolution. The theoretical resolution for the last case was 10 mm. The antenna pattern of the X-band waveguide adapter changes as a function of frequency, but the effect of antenna pattern is less than that of the actual frequency of operation. This is due to the fact that the half-power beamwidths of a rectangular aperture antenna with TE_{10} mode distribution do not change greatly between minimum and maximum frequencies in the band [55]. The next section will now apply the method of FD-SAFT to SOFI rather than small rubber pads.

2.5. SOFI CUBES

2.5.1. Description/Purpose. The goal is to ultimately apply FD-SAFT to SOFI samples rather than rubber pads. The primary difference between the two is that SOFI samples are far weaker scatterers than rubber pads. To test whether the network analyzer at the *amntl* could detect such weak reflections, experiments on SOFI cube samples were performed. Cube size was varied to change the effective scattering strength and further test the ultimate capabilities of the network analyzer and the algorithm. The data for all experiments was expected to be visually more noisy as compared the cases of the rubber

pads because the reflections of the air-to-SOFI boundary are about 15 dB less than air-to-rubber.

Three specific experiments with SOFI cubes are described in this section: 1) one 1-inch SOFI cube scanned at Ku-band (12.4-18 GHz with 201 points), 2) two 0.5-inch SOFI cubes separated by 0.5 inch scanned at Ku-band, and 3) one 1-inch SOFI cube and two-0.5 inch SOFI cubes scanned together at X-band (8.2-12.4 GHz with 201 points). Two different frequency bands were used to compare their respective resolutions.

The setups for experiments 1, 2, and 3 included a square scan area of 260 mm by 260 mm ($w = 260$ mm) with a scanning increment of $\Delta = 5$ mm. The height from the sample to the measurement plane was $h = 105$ mm. The power setting of the network analyzer was set at 0 dBm. All datasets were interpolated once along the x and y axes to synthesize a scanning increment of $\Delta = 2.5$ mm and make the images less pixelated.

2.5.2. Results. The first experiment of a single 1 inch SOFI cube at Ku-band showed that the cube could be detected, as shown in Figure 2.5. The image produced from the magnitude of the reflection coefficient, $|\Gamma|$, at 18 GHz shows the presence of a scatterer, as shown in Figure 2.5b. The relative noise level to the measured signal is considerably higher as compared to Figure 2.3c, which is a strongly reflecting rubber pad at nearly the same distance. After FD-SAFT processing, the resulting image shows a small red square region corresponding to the 1-inch cube, as shown in Figure 2.5c. It is important to note that the dimensions of the red square region match well with the actual dimensions of the cube. At other frequencies, not shown, the apparent noise in $|\Gamma|$ was much higher and the associated sharpness of the FD-SAFT processed image was degraded significantly. Returning to Figure 2.5c, the variations in the blue background of

the processed image indicate a non-level aluminum substrate, which is more evident in the next experiment. The light blue region, near $y = 0$, corresponds to the edge of the aluminum substrate.

The second experiment involved two 0.5-inch SOFI cubes. This was more challenging in two ways: 1) the SOFI cubes were smaller providing less scattered signal, 2) the SOFI cubes had to be not only detected but also distinguished from one another. A picture of the SOFI cubes is provided in Figure 2.6a and an approximate schematic of the setup can be seen in Figure 2.6b. The unprocessed $|\Gamma|$ image at 18 GHz can be seen in

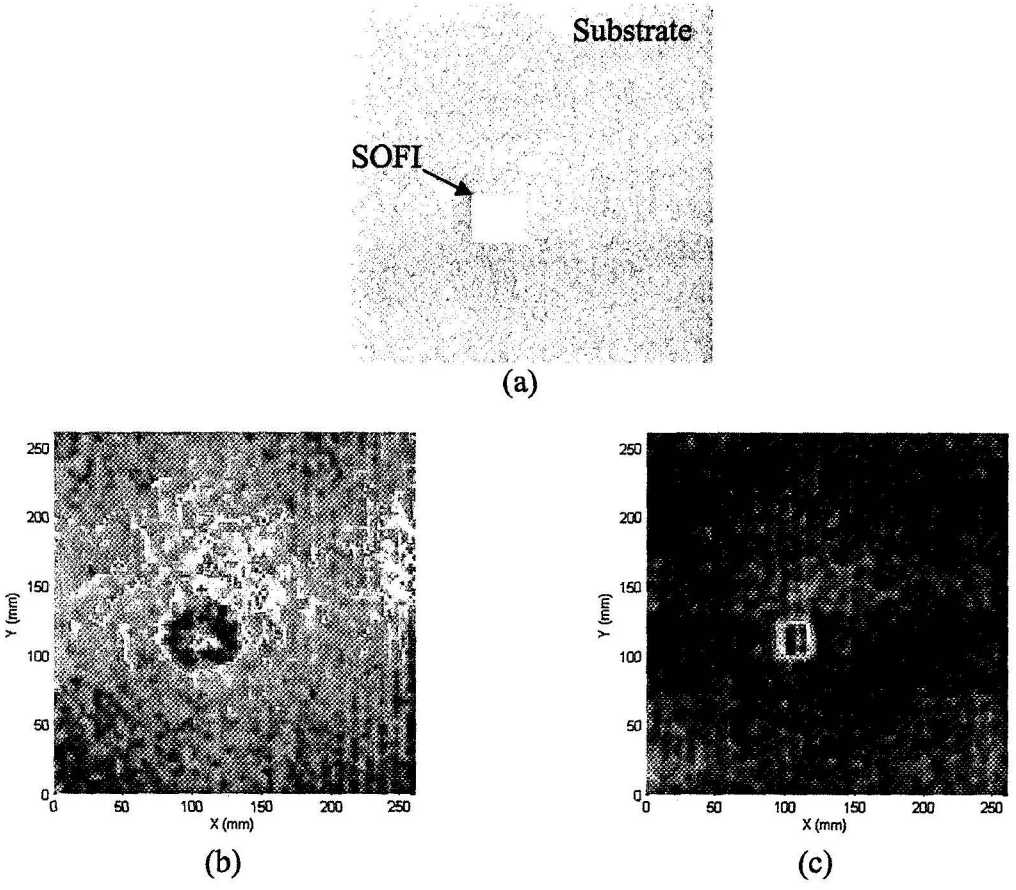

Figure 2.5. One 1-inch SOFI cube scanned at Ku-band (18 GHz): (a) arrangement schematic, (b) $|\Gamma|$, (c) FD-SAFT.

Figure 2.6c where the image does not visibly indicate that there is even a scatterer present. The lower edge, near $y = 0$, shows the largest values of $|\Gamma|$ corresponding to the edge of the aluminum substrate. The result of FD-SAFT processing can be seen in Figure 2.6d where both cubes are clearly shown in yellow and red patches. It is important to note that the apparent size of the cubes are close to the physical size of 0.5 inch or 13 mm. Also, apparent in Figure 2.6d is the same non-level nature of the aluminum substrate, as shown in the yellow and light blue region to the right of the 0.5-inch SOFI cubes. It

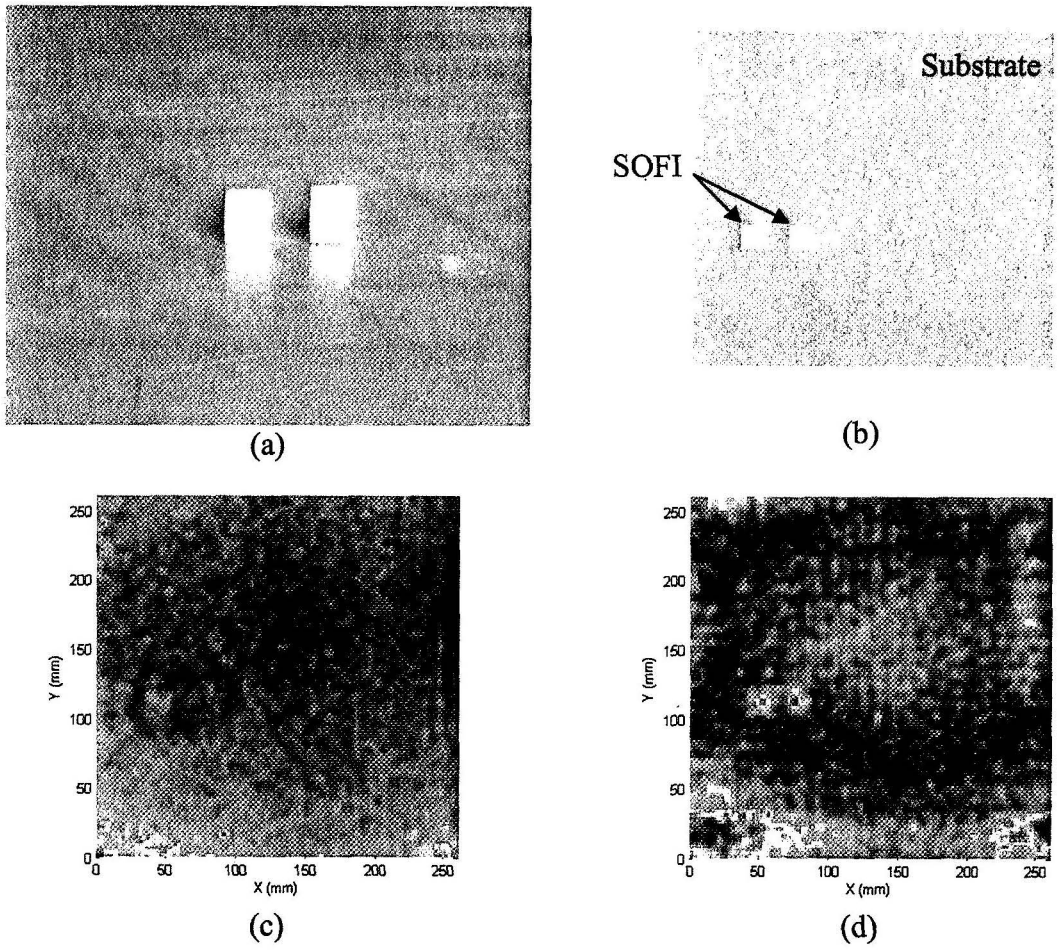

Figure 2.6. Two 0.5-inch SOFI cubes separated by 0.5-inch at Ku-band (18 GHz): (a) picture of SOFI cubes, (b) arrangement schematic, (c) $|\Gamma|$, (d) FD-SAFT.

appears brighter as compared to the previous experiment seen in Figure 2.5c. This is because the scale is relative to the brightest scatterer present, and the substrate appears that much brighter because the two 0.5-inch cubes scatter so much less than that of the 1-inch cube.

It is important to note that the frequency of 18 GHz was chosen to show the best possible resolution available in the Ku-band (12.4-18 GHz) frequency range. However, this experiment is different from the former in that some frequencies (not shown) did not show the cubes in either in $|\Gamma|$, ϕ, or FD-SAFT processing. This is because reflections from the lower edge of the plate, visible at $y = 0$, dominated the image for these frequencies. Still, the majority of measured frequencies showed evidence of the SOFI cubes on top of the substrate.

The third experiment consisted of a combination of the first and the second experiments and it was meant to show not only that both sizes of the cubes can be detected in the same image but also to show the relative strength of the cubes with respect to each other. Figure 2.7a shows a picture of the SOFI cubes. However, this is not the actual setup, rather the 0.5-inch SOFI cubes were separated from the 1-inch cube by approximately 70 mm. This is better demonstrated in Figure 2.7b. This experiment was performed in X-band at a frequency of 10.3 GHz, which provides a lower available resolution due to waveguide size and more importantly frequency.

The unprocessed $|\Gamma|$ image is shown in Figure 2.7c where apparently only the signal from the 1-inch cube can be observed near the center of the image and there is no immediate evidence of the two smaller 0.5-inch cubes. Also, shown in this image is a strong contribution from the right edge of the substrate. The FD-SAFT processed image

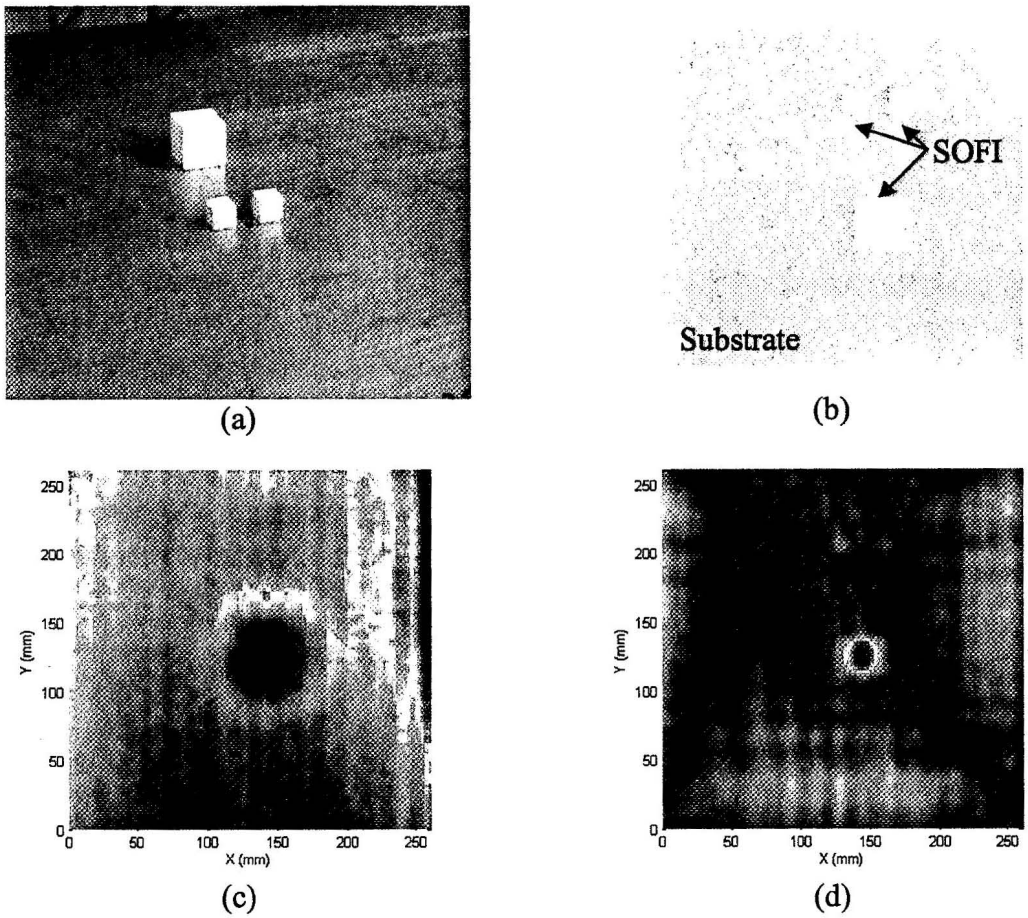

Figure 2.7. One 1-inch cube and two 0.5-inch cubes at X-band (10.3 GHz): (a) approximate picture of setup, (b) arrangement schematic, (c) $|\Gamma|$, (d) FD-SAFT.

in Figure 2.7d achieves the goal of detecting all three cubes present in the image despite the fact that edge effects fill the surroundings in colors of light blue and yellow. The 1-inch cube shows up very bright with shades of red and yellow compared to the much dimmer two 0.5-inch cubes that show up in a pale blue color. Evidence of edge effects appear brighter than the 0.5-inch cubes as well.

2.6. FLAT-BOTTOM HOLES IN SOFI – ONE INCH-DIAMETER HOLES

2.6.1. Description/Purpose. After the successful detection of SOFI in air, it was time to detect air voids in SOFI. One of the first experiments performed was the case of five 1 inch-diameter flat-bottom holes in SOFI, and this was performed using the NASA facilities. Two 70 mm-thick SOFI slabs had been prepared, one with a set of five 1 inch-diameter holes and one without. The slab without holes was called the blank slab. The holes had been drilled right to left to the following depths: 1/8 inch (3 mm), 1/4 inch (6 mm), 1/2 inch (13 mm), 3/4 inch (19 mm), and 1 inch (25 mm), as shown in Figure 2.8a. The slabs as described above were arranged in three different configurations for three different experiments: 1) slab with holes face down and backed by an aluminum substrate (Figure 2.8a), 2) slab with holes face down and backed by a blank slab and substrate (Figure 2.8b), 3) slab with holes face down and sandwiched by the blank slab on top and the substrate on the bottom (Figure 2.8c). Scans for each experiment were taken at a frequency of 22.25 GHz that is in the K-band (18-26.5 GHz) frequency range using a power level of 0 dBm, liftoff of 10 mm above the SOFI, and a sampling increment of Δx = 2 mm.

1 inch-diameter holes were thought to be strong enough scatterers given that the 1 inch cube provided a relatively strong reflection at Ku-band (see Section 2.5 for details). The purpose of the first two experiments was to analyze the behavior of moving the substrate away while retaining the height of the holes. It was expected that the results of these two cases would be the same if the holes were detected. The purpose of experiments 1 and 3 were to observe moving the holes away from the measurement

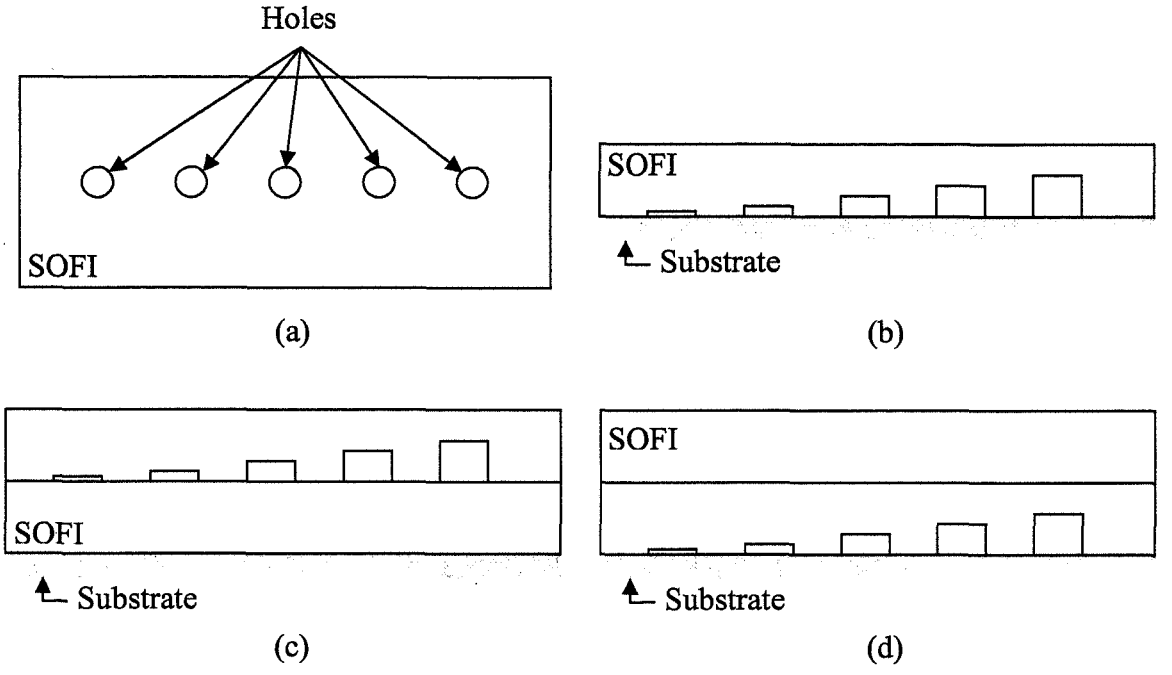

Figure 2.8. One inch-diameter flat-bottom holes schematic: (a) top view for all cases; schematics for (b) experiment 1, (c) experiment 2, (d) experiment 3.

plane. This can significantly reduce the signal strength associated with the holes until they are undetectable by the network analyzer.

2.6.2. Results. Experiment 1 was the case of the SOFI slab with holes laid face down on the aluminum substrate, as shown in Figure 2.8b. The unprocessed $|\Gamma|$ image shows evidence of the three deepest holes on the right, as shown in Figure 2.9a. Figure 2.9b shows the data after processing with FD-SAFT where four of the holes can be distinguished. FD-SAFT was focused at 76 mm from the measurement plane. The only hole that cannot be seen is the 1/8 inch-deep hole. Rather than the signal level from the 1/8 inch deep hole dropping below the noise of the system it may be that the edge effects dominated the hole and masked its indication. Edge effects are the result of the edge of the metal plate and they are more dramatic for edges cross-polarized to the incident wavefront. The signal level associated with the 1 inch-deep hole on the right is strong

enough to overcome the edge effects, however the signal level from the 1/8 inch-deep hole on the left is not.

Experiment 2 is where the SOFI slab with holes is backed by the blank slab and the substrate, as shown in Figure 2.8c. To aid in target recognition and contrast, the outer border of the dataset was cropped to omit part of the edges. The unprocessed $|\Gamma|$ image can be seen in Figure 2.9c where two of the deepest holes can be recognized. However,

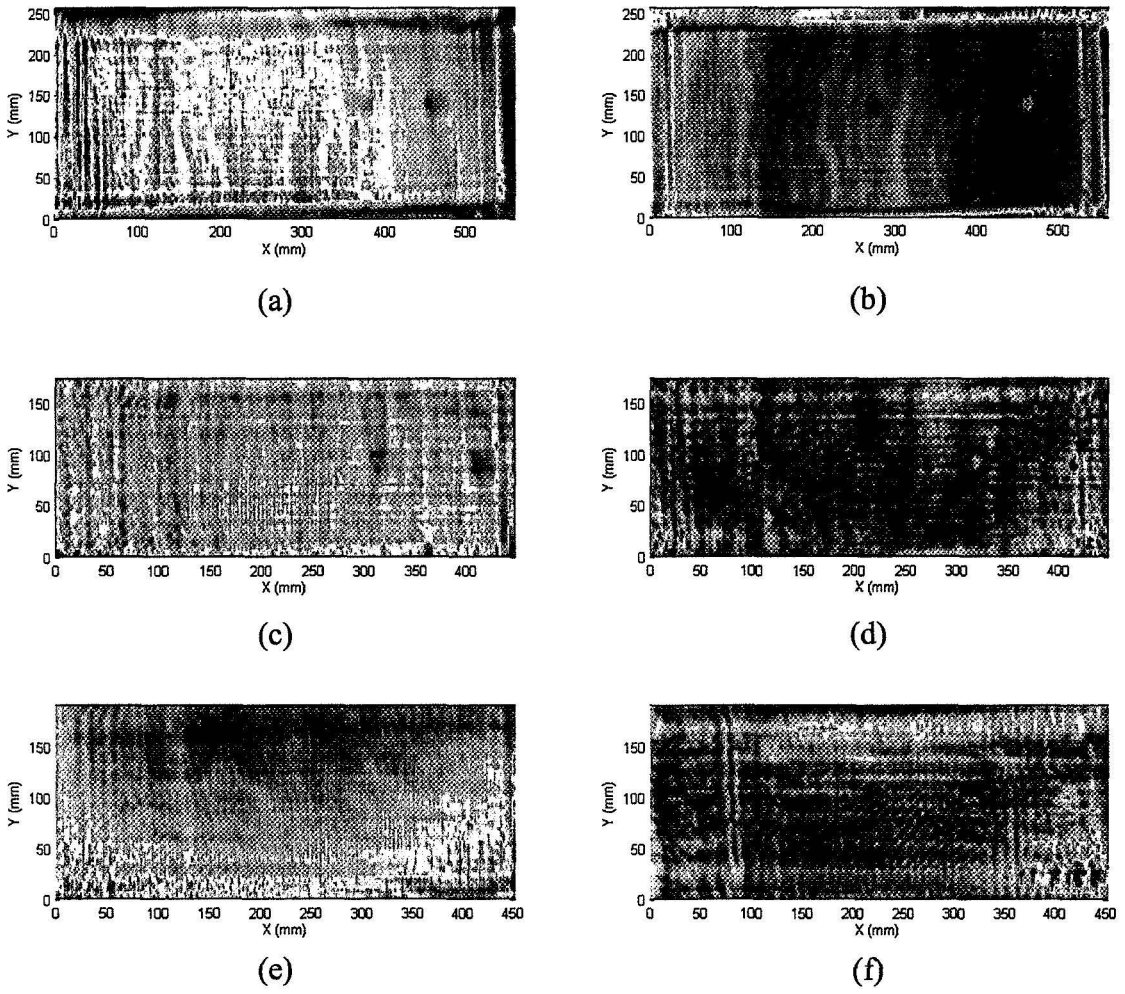

Figure 2.9. One inch-diameter flat-bottom holes image results: experiment 1, (a) $|\Gamma|$, (b) FD-SAFT $h = 76$ mm; experiment 2, (c) $|\Gamma|$, (d) FD-SAFT $h = 76$ mm; experiment 3, (e) $|\Gamma|$, (f) FD-SAFT $h = 152$ mm.

the FD-SAFT processed data, seen in Figure 2.9d, only shows the deepest hole when focused at 76 mm. FD-SAFT seemed to make the image worse in this case. Edge effects are also visible. It is important to note that only the backing was changed between this experiment and experiment 1. It was thought that experiments 1 and 2 would provide similar results in detecting the holes in SOFI, but they did not, and three of the previously detectable holes were not detected in experiment 2. Therefore, the detection of the holes does not indicate the detection of the first SOFI-to-air boundary corresponding to the top of the hole. The signal level from that reflection is too low to detect.

Experiment 3 is where the SOFI slab with holes was sandwiched by the blank slab and the aluminum substrate. This effectively moved the holes away an additional 70 mm below SOFI as compared to experiment 1. The dataset for this experiment was also cropped as in experiment 2 to aid in target recognition. For this experiment, the power of the received signal was near the end of the range of the particular network analyzer. The power was so low that the signal from the holes cannot be seen visually. Figure 2.9e shows the unprocessed $|\Gamma|$ image where no visual indication of the holes can be seen. Unfortunately, FD-SAFT also provides no indication of the holes, as shown in Figure 2.9f. For this case, FD-SAFT was focused to 152 mm away from the measurement plane corresponding to the substrate. For a single frequency with no averaging, the noise seemed to overwhelm the available and relatively low level signal from the holes.

2.7. FLAT-BOTTOM HOLES IN SOFI – TEST GRID

2.7.1. Description/Purpose. It was learned in Section 2.6, for the case of 1 inch-diameter flat-bottom holes in SOFI, that FD-SAFT was greatly dependent on the received signal level. This experiment aimed to investigate the available resolution for FD-SAFT with a fixed substrate height and fixed hole distance. To this end a 12 inch by 12 inch (305 mm by 305 mm) and 3 inch (76 mm) thick flat-bottom hole sample was produced with hole diameters ranging from 1/8 to 1 inch and depths ranging from 1/8 to 3/4 inch, as shown in Figure 2.10. Reflected signal strength from the holes is expected to drop for decreasing hole diameter and decreasing hole depth. From the results it is possible to determine the minimum detectable defect size of an air void in SOFI for FD-SAFT processing given the frequency of operation, antenna type, displacement of substrate to the measurement plane, and measurement plane dimensions.

The schematic of the sample is shown in Figure 2.10 where rows labeled 1 through 4 determine hole depths and columns labeled A through E determine hole diameters. The hole depths are: 1) 1/8 inch (3 mm), 2) 1/4 inch (6 mm), 3) 1/2 inch (13 mm), and 4) 3/4 inch (19 mm). The hole diameters are: A) 1/8 inch (3 mm), B) 1/4 inch (6 mm), C) 1/2 inch (13 mm), D) 3/4 inch (19 mm), and E) 1 inch (25 mm). Measurements were performed at the NASA facilities using a K-band rectangular waveguide probe operating at a frequency of 22.25 GHz, a scanning increment of $\Delta x = 4$ mm, a liftoff of 10 mm, and a power level of -6 dBm. The probe orientation was such that the polarization of the signal was aligned along the top and bottom edges of the sample. For processing, the dataset was interpolated along the x and y axes to simulate a scanning increment of $\Delta x = 2$ mm, and the dataset was cropped to mitigate signals from the edges.

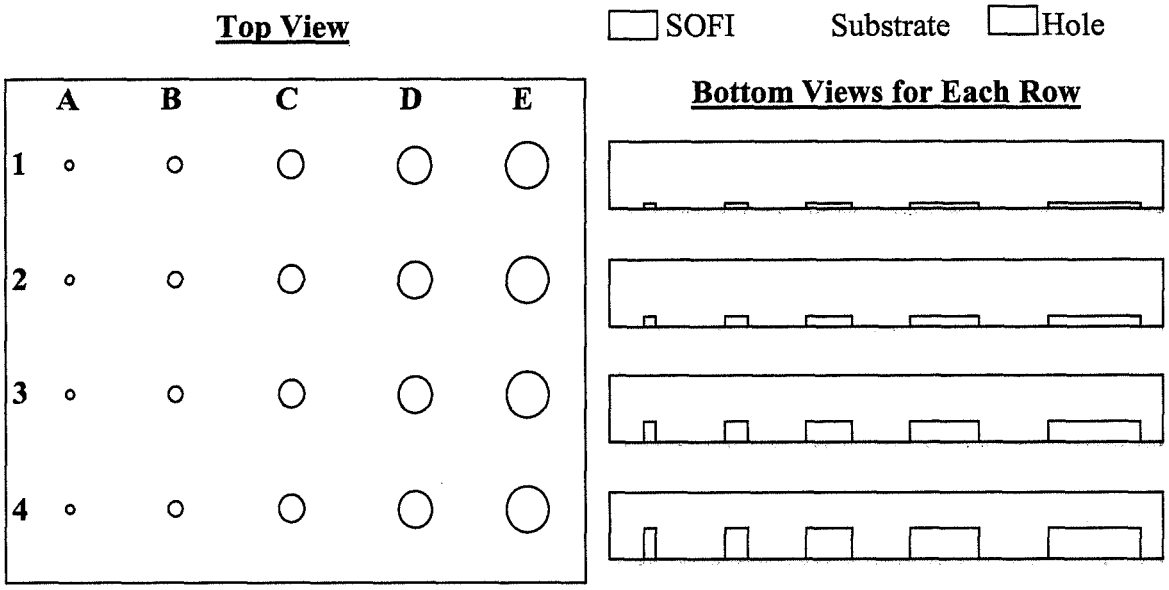

Figure 2.10. Schematic of the flat-bottom hole test grid in SOFI.

2.7.2. Results. Using these results it is possible to determine the dimensions of the smallest detectable air void in SOFI using FD-SAFT given the previously defined measurement setup. Figure 2.11a shows the unprocessed $|\Gamma|$ image and two of the deepest holes can be seen in the lower right. The FD-SAFT processed data is shown in Figure 2.11b. Here, the dataset was focused at 110 mm from the measurement plane to provide the result with the least noise variation. Note that 110 mm is actually beyond the substrate. If FD-SAFT had been focused at the substrate, that height would have been 86 mm. The height of 110 mm is more indicative of measuring the same holes in the mirror reflection that the substrate provides. Figure 2.11c shows the detected holes in white circles. The smallest diameter detected was 1/2 inch and the shallowest depth was 1/4 inch. The smallest volume detected was the 3/4 inch-diameter and 1/4 inch-deep hole corresponding approximately to a volume of 0.1 in^3 or 1.6 cm^3.

The holes near the edges were again dominated by edge effects much like the case for Section 2.6. This is especially true for the smallest diameter holes (1/8 inch) on the far left. The attempt taken to reduce edge effects by cropping the dataset proved insufficient to mitigate the edge effects, and only a larger substrate would provide for a sufficient remedy.

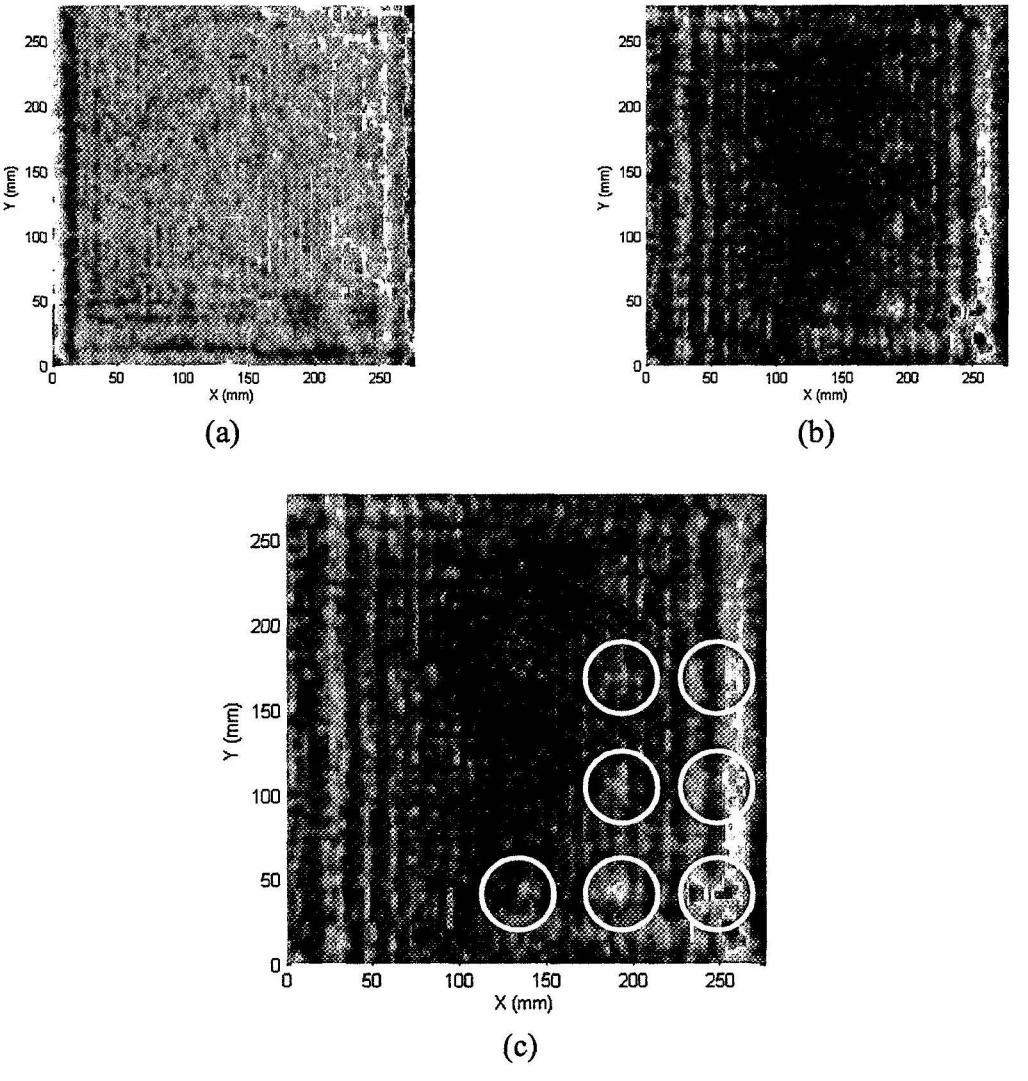

Figure 2.11. Test grid of flat-bottom holes in SOFI: (a) $|\Gamma|$, (b) FD-SAFT $h = 110$ mm, (c) FD-SAFT $h = 110$ mm with circles indicating distinguished holes.

2.8. STRINGER PANEL – POD 50-R

2.8.1. Description/Purpose. Subsequent to establishing the minimum detectable size of defect was 0.1 in^3 (1.7 cm^3) for an operating frequency of 22.25 GHz, height h of 86 mm, and scan dimension w of 305 mm, it was important to apply FD-SAFT to a more real-world sample like a SOFI specimen constructed similarly to the external tank of the Space Shuttle (Section 1.4). The specimen selected for this experiment was referred to as the POD 50-R panel. This panel provided for a far more complex geometry than those investigated thus far. POD 50-R was designed to resemble a region on the external tank where either the liquid oxygen tank or the liquid hydrogen tank joins the intertank. The panel contained stringers, flanges, their corresponding bolts, and several embedded voids in the SOFI.

The POD 50-R panel measured 2 by 2 feet (610 mm by 610 mm) and was covered in at least an inch of SOFI. The SOFI rind was machined until smooth, as shown in Figure 2.12. The measurements were performed at the NASA facilities using a K-band rectangular waveguide probe operating at a frequency of 22.25 GHz, a scanning increment of $\Delta x = 4$ mm, a liftoff of 10 mm, and a power level of 0 dBm. Due to complexities associated with the panel, the scan was performed for two different orientations of the probe: one where the signal polarization of the probe was parallel to the length of the stringer or stringer axes and another perpendicular to that. These two orientations are referred to as parallel to the stringer axes and perpendicular to the stringer axes, respectively.

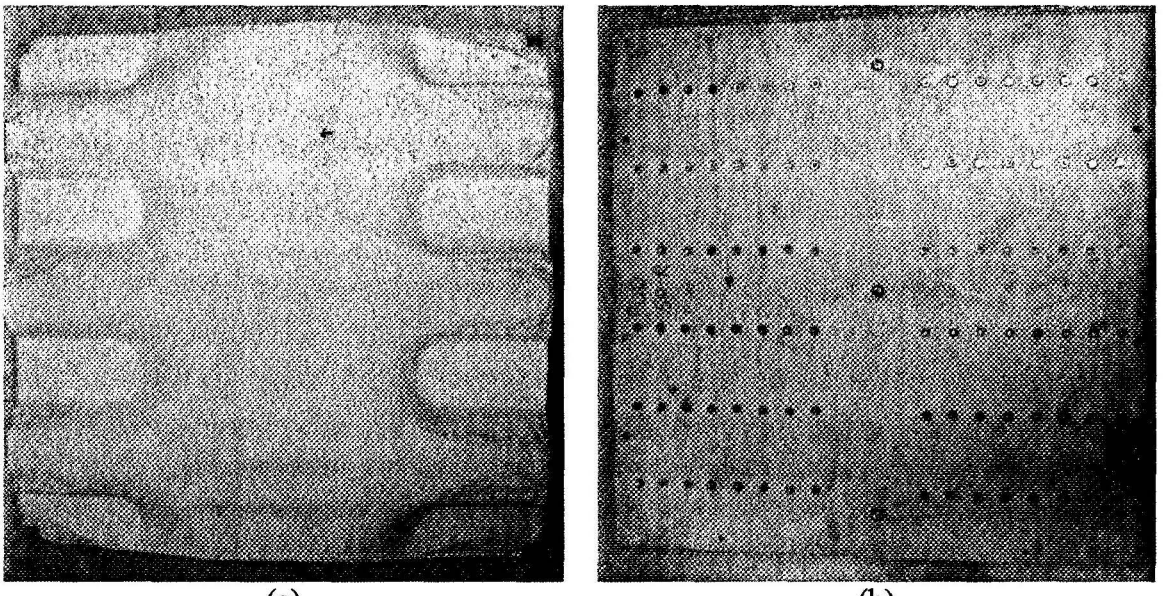

(a) (b)

Figure 2.12. SOFI sample POD 50-R: (a) top view, (b) bottom view.

2.8.2. Results. The unprocessed $|\Gamma|$ image parallel to the stringer axes shows the flange and stringer hats, as shown in Figure 2.13a. The regions not identified with stringer hats or flange are full of variations that are attributed to the substrate. These variations disappear after FD-SAFT processing focuses at the substrate 110 mm away, as shown in Figure 2.13b. The stringer hats are more pronounced as well as the flange edges, which are cross-polarized to the incident wavefront. Also, every stringer bolt can be seen. However, the stringer sides cannot be seen since they deflect the beam away from the point of measurement. Only indirect evidence of the flange bolts can be seen as they interfere with the signal from the flange edge. None of the SOFI void inserts can be seen in this image since the metal structure is a strong reflector. It is thought that an analysis software could bring out these features, but that is reserved for future work.

The case where the incident wavefront is perpendicular to the stringer axes provides different results. The unprocessed $|\Gamma|$ image again shows the stringer hats and

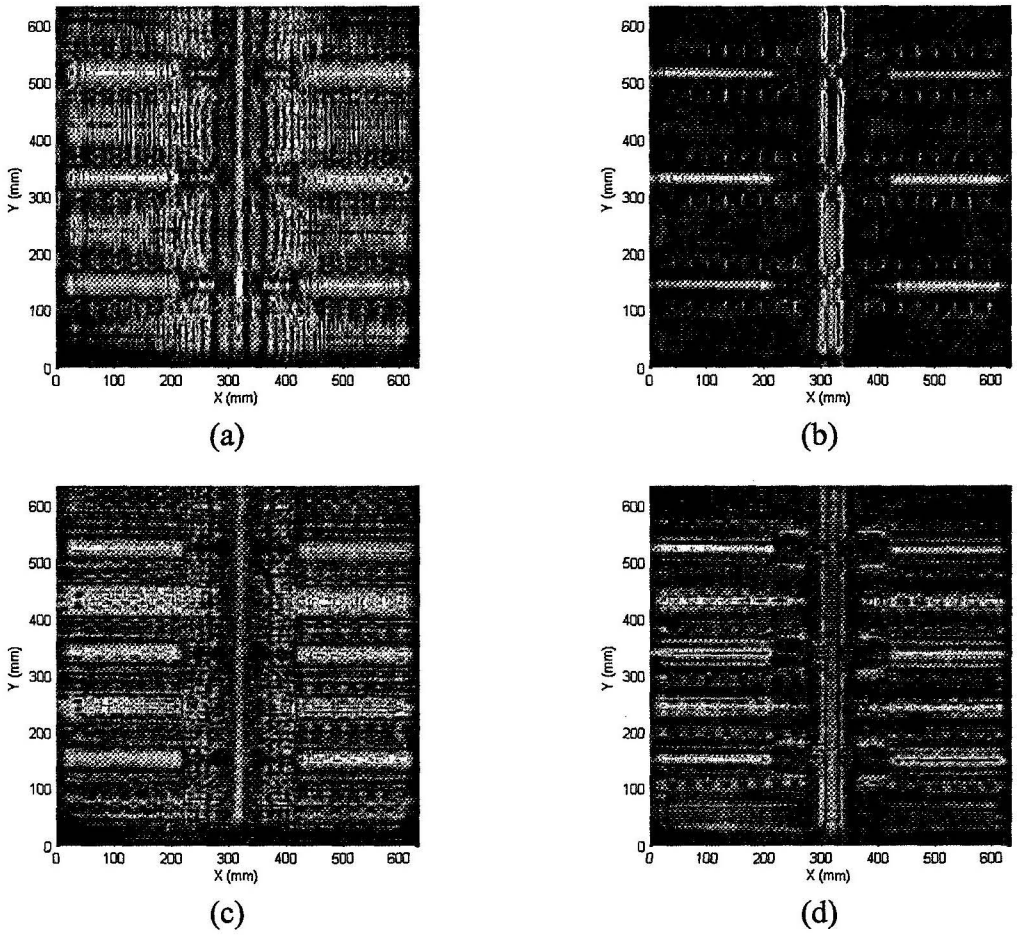

Figure 2.13. SOFI panel POD 50-R at 22.25 GHz focused at h = 110 mm: parallel to stringer axes, (a) |Γ|, (b) FD-SAFT; perpendicular to stringer axes, (c) |Γ|, (e) FD-SAFT.

the flange, as shown in Figure 2.13c. Different from before is that the region between the stringers is brighter, represented by yellow and red indications. These regions are still pronounced in the FD-SAFT processed image, as shown in Figure 2.13d, and they seem to interfere with the stringer bolts. Also, evident in Figure 2.13d is the flange top, stringer hats, stringer bolts, and the sides of the stringer opening.

An important lesson was learned while scanning this panel. Using two polarizations of the incident wavefront in combination resulted in more features being detected than a single polarization and different features were pronounced depending on

the polarization. For this reason, the next experiment also consisting of a SOFI panel with stringer was measured the same way using two orthogonal polarizations.

2.9. STRINGER PANEL – NATURAL VOID

2.9.1. Description/Purpose. This panel with natural voids was similar to POD 50-R in that it was supposed to model a section of the external tank joining with the intertank. However, the natural void panel differed from the former in the fact that it was devoid of embedded air voids. Instead, the construction of the natural void panel simply involved spraying on the foam insulation poorly. This was expected to result in a SOFI sample full of irregular voids some of them being bubble-like, some long and thin, and some irregularly shaped.

As seen in Figure 2.14, this panel is different from the POD 50-R panel in that it is supposed to resemble a ramp that rises along the flange length. The ramp provides a substantial increase in SOFI material that signal must pass through before reaching the internal metal structure. Results shown here are limited to a comparison to POD 50-R and the effect of increased height of SOFI over the detectable metal structure. Therefore, FD-SAFT is focused at 220 mm corresponding to the level of the substrate. Note that the upper left corner of the SOFI sample depicted in Figure 2.14 corresponds to $x = 0, y = 0$ coordinates.

This natural void panel measured 2 by 2 feet (610 mm by 610 mm), and the SOFI rind was machined until smooth, as shown in Figure 2.14. The scan was performed at the NASA facilities using a K-band rectangular waveguide probe operating at 22.25 GHz, a scanning increment of $\Delta x = 4$ mm, a liftoff of 10 mm from the highest point measured,

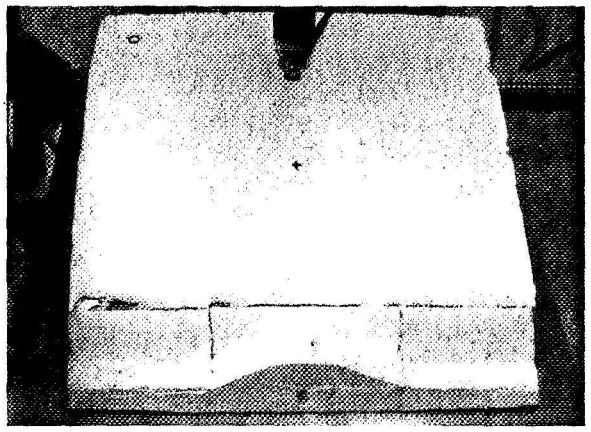

Figure 2.14. Picture of SOFI stringer sample with natural void.

and a power level of 0 dBm. The scan was performed using two orthogonal polarizations as before.

2.9.2. Results. The results are similar to the case of POD 50-R, however, for this case noise begins to dominate. For both polarizations, only the stringer can be identified from the unprocessed $|\Gamma|$ image, as shown in Figures 2.15a and 2.15c. FD-SAFT processing can only distinguish some of the stringer bolts, flange edge, stringer hats, and indirect evidence of the flange bolts, as shown in Figures 2.15b and 2.15d. However, the stringer hats are far less pronounced as compared to the corresponding image of POD 50-R since the stringer hats were farther away, as shown in Figures 2.13b and 2.15b. The case where the incident wavefront polarization is perpendicular to the stringer axes is particularly noisy, as shown in Figure 2.15d. The signal levels of the scatterers in FD-SAFT processed image are significantly reduced as compared to Figure 2.13d due to the increased height of SOFI over the internal metal structure.

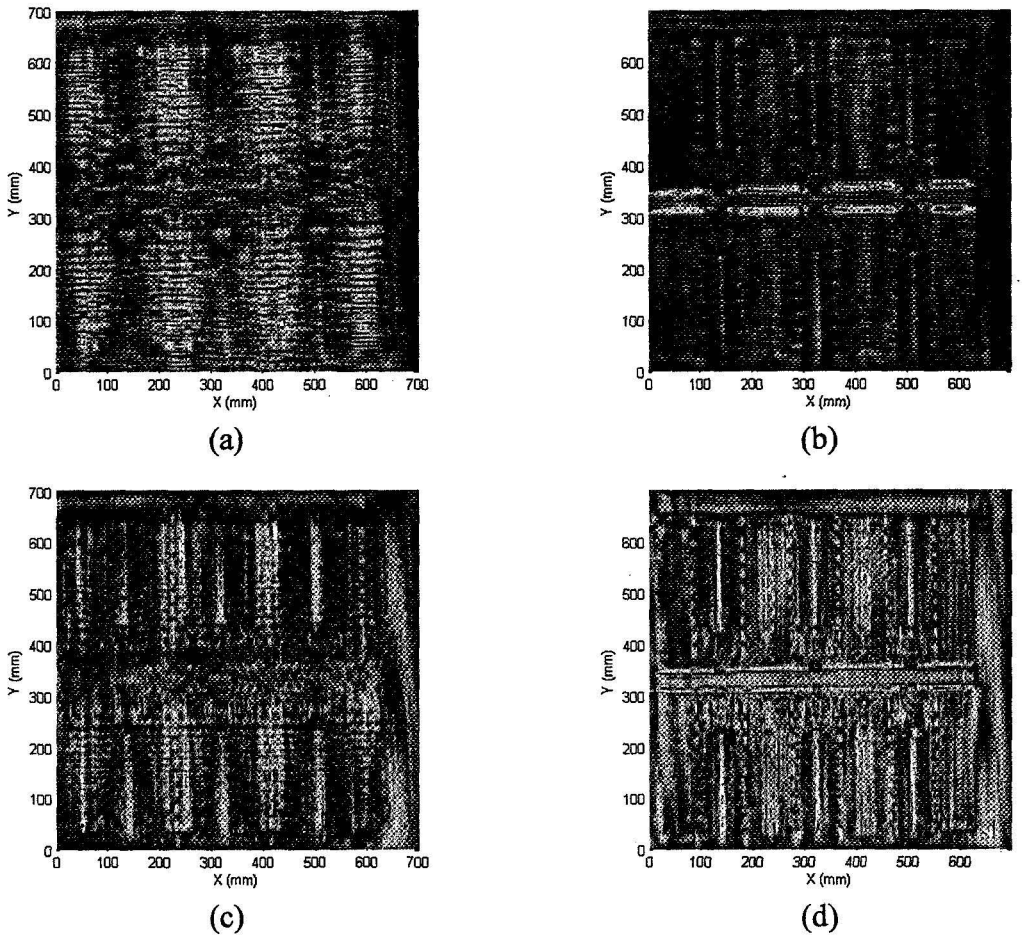

Figure 2.15. SOFI stringer sample with natural void at 22.25 GHz focused at $h = 220$ mm: (a) $|\Gamma|$ parallel to stringer, (b) FD-SAFT parallel to stringer, (c) $|\Gamma|$ perpendicular to stringer, (d) FD-SAFT perpendicular to stringer.

2.10. SUMMARY AND LIMITATIONS

Much was learned from the application of FD-SAFT to several cases as described in Sections 2.5 – 2.9. The scans of SOFI cubes showed that the SOFI-to-air boundary was detectable. The case of 1 inch-diameter flat-bottom holes showed that air voids could be seen in SOFI. It also showed that FD-SAFT could not see the SOFI-to-air boundary at long distances due to insufficient reflected signal power and that the holes were more easily found when occurring just above the substrate. The scan on the flat-bottom hole

test grid showed that the smallest detectable volume was a 0.1 in^3 (1.6 cm^3) volume with a 3/4 inch (19 mm) diameter and depth of 1/4 inch (6 mm) at an operating frequency of 22.25 GHz, a rectangular waveguide probe, the substrate 86 mm away, and a scan dimension *w* of 305 mm. The last two cases included stringer panels similar to the external tank of the Space Shuttle where one panel had embedded voids (POD 50-R) and the other had natural voids. These cases showed that measuring at two orthogonal polarizations can reveal more information. It was also shown that the metal structure could mask out defects in the SOFI, since the strength of the reflected signal from metal surface is much stronger than reflected signal from the SOFI. The defects, being so weakly scattering, would have to be brought out in an analysis software looking for small local variations. It was also shown that increased height significantly reduces signal strength since the rectangular waveguide probes used to measure the reflection are low gain and less detail can be seen in FD-SAFT images focused for long distances.

The advantages of FD-SAFT is that it is single frequency, not requiring wide-band measurements, and it is fast by virtue of the extensive use of efficient two dimensional Fast Fourier transform algorithms. Additional advantages include that it is relatively easy to implement compared to other synthetic focusing methods and it requires little computer memory. However, a few disadvantages are attributable to FD-SAFT. There are three main disadvantages to FD-SAFT. First, the focus height must be known *a priori* or guessed, which cannot always be possible. Secondly, the method performs poorly for low signal power levels. The discrimination of objects in the image decreases greatly for increased distance away from the measurement plane, as evident in the images in Section 2.6 and a comparison between Sections 2.8 and 2.9. Thirdly, there

is no appreciable range resolution. Although not immediately beneficial to a two dimensional image, range resolution would provide a significant signal increase for a scatterer some distance away from the measurement plane. This is due to the fact that without range resolution the scatterer is blurred and stretched in the z-direction. If the signal were compressed in the z-direction, the signal of the scatterer would add constructively and it could be more readily seen in an image focused at the proper height. The next section discusses wide-band microwave holography, which will overcome these three disadvantages of FD-SAFT.

3. MICROWAVE HOLOGRAPHY

3.1. INTRODUCTION

Microwave holography, can be used to generate a full three dimensional (3D) representation of an object or embedded defect [17]. Thus, the three dimensional position and shape of the defect may be determined. Applications that have already used microwave holography include surveillance and concealed weapon detection.

The specific method used in this investigation is the wide-band microwave holography developed by Sheen, McMakin and Hall [17]. This method utilizes a swept frequency measurement over the measurement plane resulting in a dataset of (x, y, f). After processing, the resulting dataset is a volumetric representation of an object and can be graphically illustrated as such. In this thesis, slices of the volume dataset are provided along with full 3D views corresponding to the nature of a particular sample used.

The method of wide-band microwave holography will be used to remedy the three weaknesses of FD-SAFT discussed in Section 2. Firstly, the focal height need not be known *a priori* since wide-band microwave holography provides depth information through frequency. Secondly, the ability to detect small signals is better for this method as compared to FD-SAFT since this method inherently requires measurements conducted at many frequencies. Noise tends to be averaged out since the algorithm requires a summation over all frequencies for every point generated in the hologram. Lastly, microwave holography, implied by its name, provides appreciable range resolution thereby augmenting small signals at their locations in three dimensions. Therefore, much improved processed images are expected from this method as compared to FD-SAFT.

This section provides the algorithm and results for the same examples used in Section 2 so that the results may be directly compared.

Section 3.2 illustrates the measurement setups used to gather data, which is nearly identical to those used for the FD-SAFT. Section 3.3 discusses the algorithm of wide-band microwave holography and its theoretical resolution. Section 3.4 shows how wide-band microwave holography is sensitive to height of the measurement plane above the sample. Sections 3.5 through 3.9 provide results for same examples shown in Section 2, indicating the performance of wide-band microwave holography and its advantages over FD-SAFT. Section 3.10 summarizes the results from all cases and describes the advantages and disadvantages of wide-band microwave holography as compared to FD-SAFT.

3.2. MEASUREMENT SETUP

The measurement setup used is identical to the setup illustrated in Section 2.2, except for the fact that wide-band microwave holography is inherently swept frequency data as opposed to FD-SAFT, which uses only a single frequency. In fact, all data taken previously for FD-SAFT was measured for a swept frequency range to provide data for a future method that would use all of the available bandwidth. For this reason, measured data for FD-SAFT and wide-band microwave holography are identical, and only the image processing method is different. The spatial sampling increments for this data were identical to the FD-SAFT cases. The number of frequency points met or exceeded the criterion needed for this method, as described in Section 3.3.

3.3. WIDE-BAND MICROWAVE HOLOGRAPHY ALGORITHM

This section describes the algorithm and theoretical resolution of wide-band microwave holography [17]. This method is initially similar in concept to FD-SAFT, and it also uses angular spectrum decomposition and uses the same assumptions as listed in Section 2.1. The unprocessed data measured at $z = 0$ is contained in:

$$g(x, y, \omega) \tag{12}$$

such that:

$$0 \le x \le x_{\max} \text{ and } 0 \le y \le y_{\max} \tag{13}$$

and such that g is sampled at discrete locations in x and y and at discrete radial frequencies, ω. The goal is to transform the raw data into the 3D holographic representation; namely:

$$s(x, y, z) \tag{14}$$

The first step is to decompose the data onto a plane wave spectrum as before, and this must be done independently for every frequency using the 2D Fast Fourier transform:

$$G(k_x, k_y, \omega) = FFT_{2D}\{g(x, y, \omega)\} \tag{15}$$

Again, the ranges for k_x and k_y are assumed to be centered about $k_x = 0$ and $k_y = 0$. Using the dispersion relation:

$$k_x^2 + k_y^2 + k_z^2 = (2k)^2 = \left(2\frac{\omega}{c}\right)^2 \tag{16}$$

one can relate k_z to ω by:

$$k_z = k_z(\omega) = \sqrt{\left(2\frac{\omega}{c}\right)^2 - k_x^2 - k_y^2} \tag{17}$$

The complex values of k_z must be omitted since k_z is assumed to only have real values like k_x and k_y. This results in the following dataset:

$$G(k_x, k_y, k_z) \tag{18}$$

However, the spacing of data along k_z is nonlinear after this transformation and the dataset must be resampled unto a linear distribution of k_z using interpolation methods . Consequently, a fast linear interpolation scheme was used. Subsequent to the necessary resampling, the data is described by:

$$G'(k_x, k_y, k_z) \tag{19}$$

To attain the processed 3D holographic representation, $s(x,y,z)$, the inverse 3D Fast Fourier transform of the set must be obtained:

$$s(x,y,z) = FFT_{3D}^{-1}\{G'(k_x,k_y,k_z)\} \tag{20}$$

The spatial and frequency sampling intervals must be sufficient to accurately represent the processed object. This must satisfy the Nyquist rate such that the phase difference between two sample points must be less than π. The largest possible phase shift between sampling points is $2k\Delta x$ for the highest measured frequency [17]. Therefore:

$$2k\Delta x < \pi \tag{21}$$

and from this it can be determined that:

$$\Delta x < \frac{\lambda}{4} \tag{22}$$

However, the beamwidth of the antenna is less than 180°, and practical systems can use increments as much as $\lambda/2$. A similar restriction is imposed on the frequency sampling interval, Δf, such that $2\Delta k R_{\max}$ does not exceed π, where $\Delta k = 2\pi\Delta f/c$ and $R_{\max}$ is the maximum target range [17]. This requirement can also be expressed by:

$$N_f > \frac{2R_{\max}}{(c/2B)} \tag{23}$$

where N_f is the number of frequency points in the bandwidth, B, and c is the speed of light.

The spatial resolution, δ_x, is comparable to SAFT [17], more specifically:

$$\delta_x \approx \frac{\lambda_c}{4\sin(\theta_b/2)} \tag{24}$$

where λ_c is the center wavelength and θ_b is either the full beamwidth of the microwave probe or the angle subtended by the measurement plane, whichever is less [17]. The range resolution, δ_z, is related to the wavenumbers pertaining to the bandwidth of the system. Let $k_{\max}$ and $k_{\min}$ be the maximum and minimum wavenumbers corresponding to the maximum and minimum frequencies measured, respectively. Therefore, $2(k_{\max} - k_{\min})$ is the spatial frequency width in the k_z direction. Consequently, the range resolution associated with this holographic method is $c/2B$, where B is the transmitted signal bandwidth [17]:

$$\delta_z \approx \frac{2\pi}{2(k_{\max} - k_{\min})} = \frac{c}{2B} \tag{25}$$

3.4. SENSITIVITY TO HEIGHT

As with FD-SAFT, a better understanding of the sensitivity of this wide-band microwave holography method to height is required. The sensitivity to frequency was not pursued since the entire available frequency spectrum in X-band (8.2-12.4 GHz) was used for processing and another frequency band would require a different waveguide probe. Therefore, only the effect of height was studied for the X-band dataset.

The same experimental setup was used as before: two 10 mm square rubber pads were cut with a thickness approximately 2 mm. The rubber pads were placed 10 mm apart on an aluminum substrate. The test was performed at X-band with 201 sampled frequency points spaced regularly between 8.2 GHz and 12.4 GHz using a power level of 0 dBm. The scanning increment was $\Delta x = 2.5$ mm or approximately one quarter of the narrow dimension of the waveguide. The scan was performed over a square region of side length $w = 160$ mm. Three scanning heights, h, were used for this experiment: 25 mm, 100 mm, and 200 mm. All datasets were interpolated along the x and y axes to synthesize a scanning increment of $\Delta x = 1.25$ mm and make the images appear less pixelized.

The immediate impacts of height away from the sample is power level and the maximum available spatial frequency, identical to the impacts on FD-SAFT in Section 2.4. The pads scattered the signal strongly, therefore, the received power levels were sufficient. However, the maximum available spatial frequency is dependent on the measurement plane height away from the target and has a direct effect on spatial resolution, as defined in Equation 24 in Section 3.3. For analysis purposes, let η be

defined for the center frequency much like it was defined in Section 2.4, such that $k = 2\pi f_c / c$, where f_c is the center frequency of the measured frequency band.

The results of this experiment can be seen in Figure 3.1 for the selected heights. The first case was for $h = 25$ mm, making $\eta = 0.95$, $\delta_x = 10$ mm, and $\delta_z = 36$ mm. The spatial resolution is sufficient to distinguish the two 10 mm by 10 mm pads, as shown in Figure 3.1a. The theoretical range resolution is dependent on the frequency bandwidth, so δ_z is the same for all three cases and does not change with respect to h. As shown in Figure 3.1b, a 3D view of the hologram shows the pads to be centered about z = -25 mm. The coloring is such that cool, transparent colors represent dim regions and hot, opaque colors represent bright regions. Scatterers near the measurement plane wrap around to the most negative values of the z-axis since the scatterer has a nonzero length along the z-axis proportional to the range resolution. The length of the hologram along the z-axis was made to be at least twice that of the height of the substrate so that targets near the measurement plane would not be ambiguously attributed to the substrate. Images of scatterers observed past the aluminum substrate are false images resulting from the mirror reflection of a scatterer in the substrate. The substrate is not seen in the images because it was subtracted out by subtracting the mean reflection coefficient of the image.

In Figure 3.1b, the 3D view shows that there is a region between and below the pads where the signals from the pads add constructively thereby creating the appearance of a third target. The second case was for $h = 100$ mm, making $\eta = 0.62$ and $\delta_x = 12$ mm. The spatial resolution is no longer sufficient to individually distinguish the two pads. As shown in Figure 3.1c, the two pads now look like one rectangular target. The 3D view of the same arrangement in Figure 3.1d shows that the two pads look like one

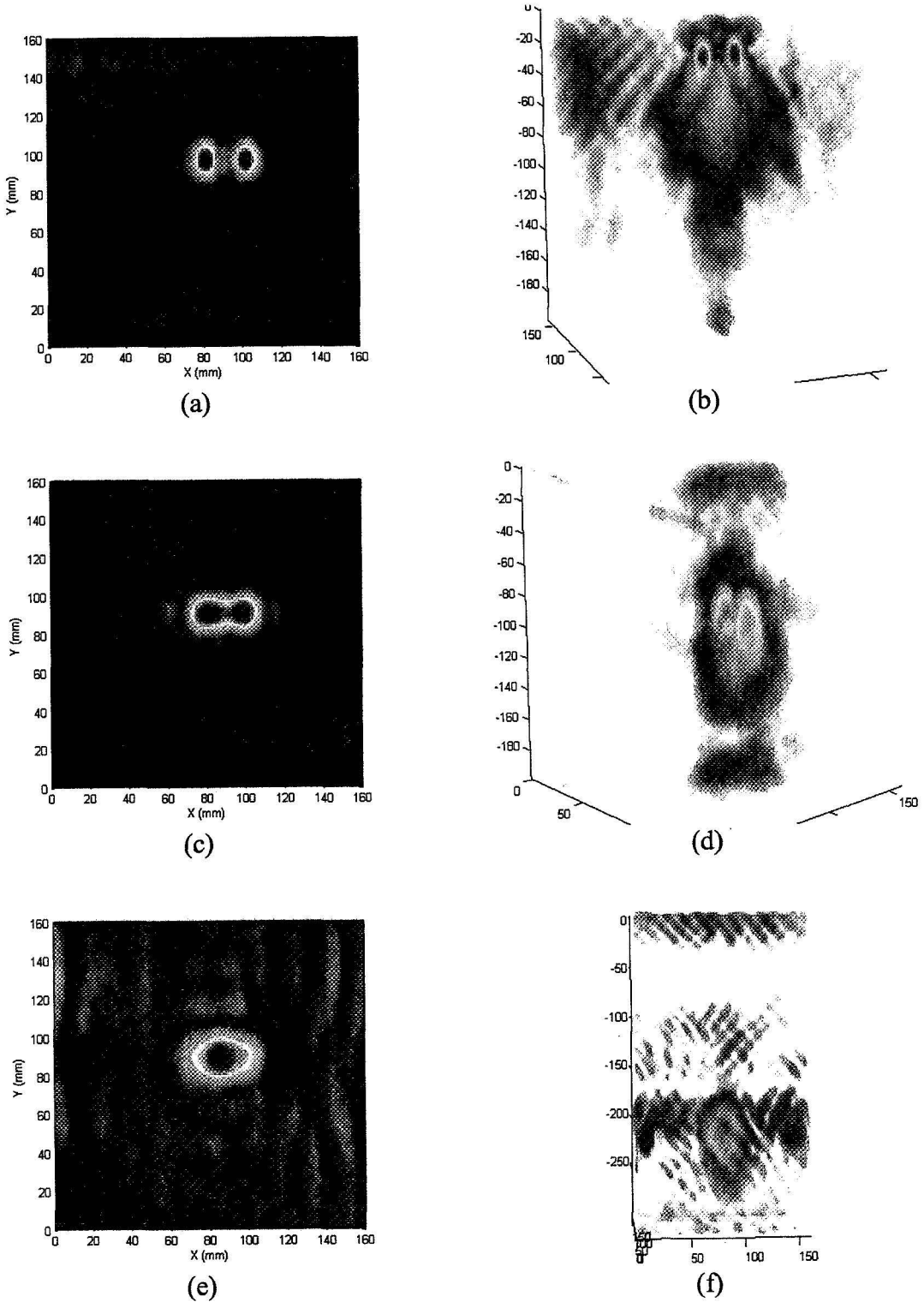

Figure 3.1. Height dependence of holography: pads at 25 mm, (a) slice, (b) 3D view; pads at 100 mm, (c) slice, (d) 3D view; pads at 200 mm, (e) slice, (f) 3D view.

irregularly shaped target, the height of which is indicative of the range resolution, δ_z, that is much greater than the 2 mm thickness of the pad. The third and last case was for h = 200 mm, making $\eta = 0.37$ and $\delta_x = 20$ mm. The resolution is so low that the images of the two pads are melded into one, as shown in Figure 3.1e. This is also evident in Figure 3.1f where the pads located at z = -200 mm appear as one large ellipsoidal target.

In summary, the results clearly show that wide-band microwave holography is affected by the height of the measurement plane from the target similarly to how FD-SAFT is affected: increasing h will lower η to decrease the maximum available spatial frequency. The strength of the signal will also decrease, however, wide-band microwave holography may reduce the noise floor of the measurement (compare Figures 2.3f and 3.1f). This is due to the fact that the method sums over all frequencies, and noise tends to be averaged out during the process, thereby making the signal of the target appear stronger. This is very important since weakly scattering SOFI cubes are used as targets instead of strongly scattering rubber pads as described in the next section.

3.5. SOFI CUBES

3.5.1. Description/Purpose. This section contains a series of experiments identical to those demonstrated in Section 2.5, except that the data is processed using wide-band microwave holography rather than FD-SAFT. The processed data contained in this section serves as a comparison between the two methods. As before, three specific experiments with SOFI cubes were performed: 1) one 1-inch SOFI cube scanned at Ku-band (12.4-18 GHz with 201 points), 2) two 0.5-inch SOFI cubes separated by 0.5-inch

scanned at Ku-band, and 3) one 1-inch SOFI cube and two 0.5-inch SOFI cubes scanned together at X-band (8.2-12.4 GHz with 201 points).

The setup of experiments 1, 2, and 3 included a square scan area of 260 mm by 260 mm with scanning increment $\Delta x = 5$ mm. The height from the sample to the measurement plane was fixed at $h = 105$ mm. The power level of the network analyzer was 0 dBm. All datasets were interpolated once along the x and y axes to synthesize a scanning increment of $\Delta x = 2.5$ mm and make the images less pixelized.

3.5.2. Results. The processed results using wide-band microwave holography and a schematic of the setup can be seen in Figure 3.2. This experiment consisted of a 1-inch SOFI cube scanned at Ku-band. A slice of the holographic dataset at the level of the substrate can be seen in Figure 3.2b, where the image of the cube is highly pronounced against the background, and the noise is suppressed as compared to Figure 2.5c. Figure 3.2c shows that the shape of the cube is rounded to a spherical shape whose dimensions are close to that of the original dimensions of the cube, 25.4 mm. The noise indicated by blue and transparent regions fills the space around the cube. These results and results following represent a significant improvement over FD-SAFT.

The next experiment was performed on two 0.5-inch SOFI cubes spaced 0.5 inches apart and was measured at Ku-band. The schematic and results of the experiment are shown in Figure 3.3. A slice of the holographic dataset at the level of the substrate can be seen in Figure 3.3c, where the two cubes are greatly pronounced above the level of noise as compared to Figure 2.6d. The 3D view also shows the two cubes well, which are circled in white, as shown in Figure 3.3d. Contributions from the edge of the aluminum substrate can be seen in regions along the bottom and right sides of the image.

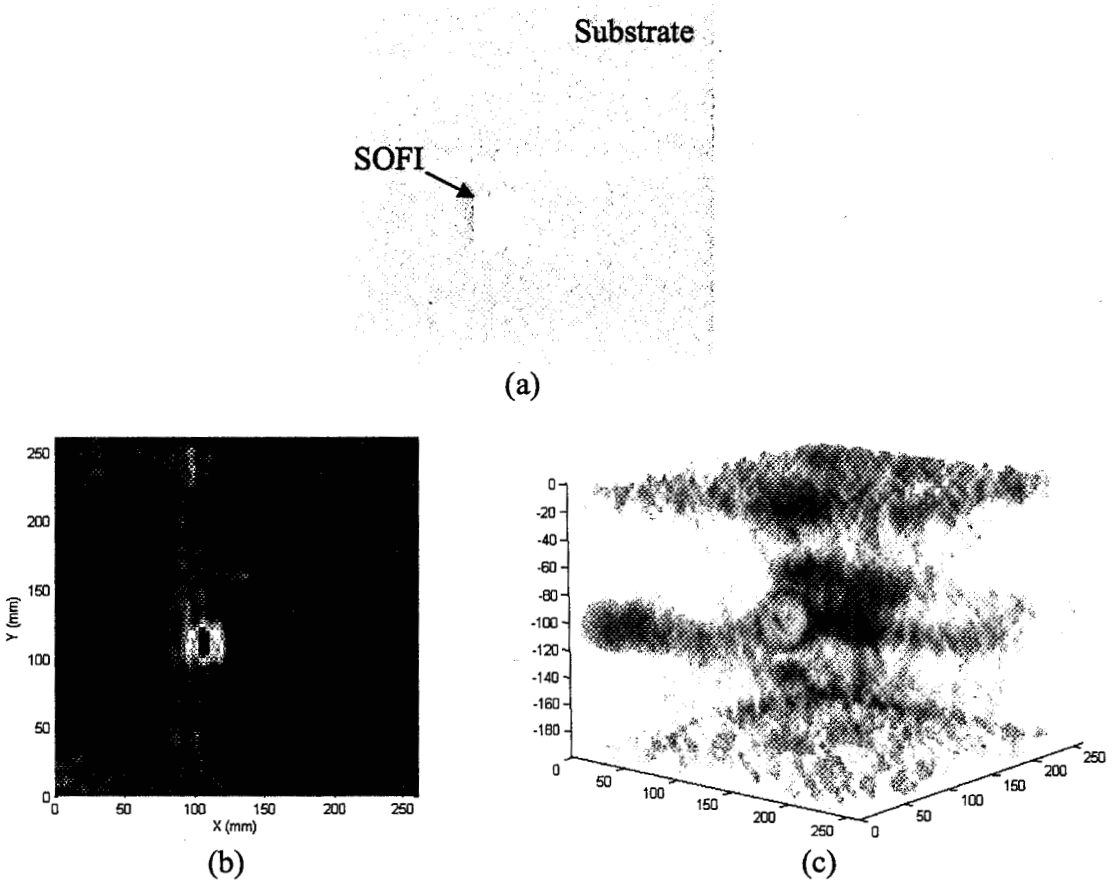

Figure 3.2. One 1-inch SOFI cube scanned at Ku-band (12.4-18 GHz): (a) arrangement schematic, (b) slice, (c) 3D view.

It is important to note that Figure 3.3d shows the cubes in shades of light blue and yellow, and the smaller SOFI cubes will scatter less. However, the SOFI cubes appearing dimmer in the image as compared to Figure 3.3c is not necessarily due to the fact that smaller cubes scatter less. For the hologram observed in Figure 3.3d, two pixels of red can be seen on the top edge nearest to the measurement plane. These are due to a relatively large and abnormal measurement variation not indicative of a reflection occurring at any point in space. This makes the variation appear as an apparition at $z = 0$, which wraps around to the other side of the hologram as seen in the lower edge of the cube near the observer.

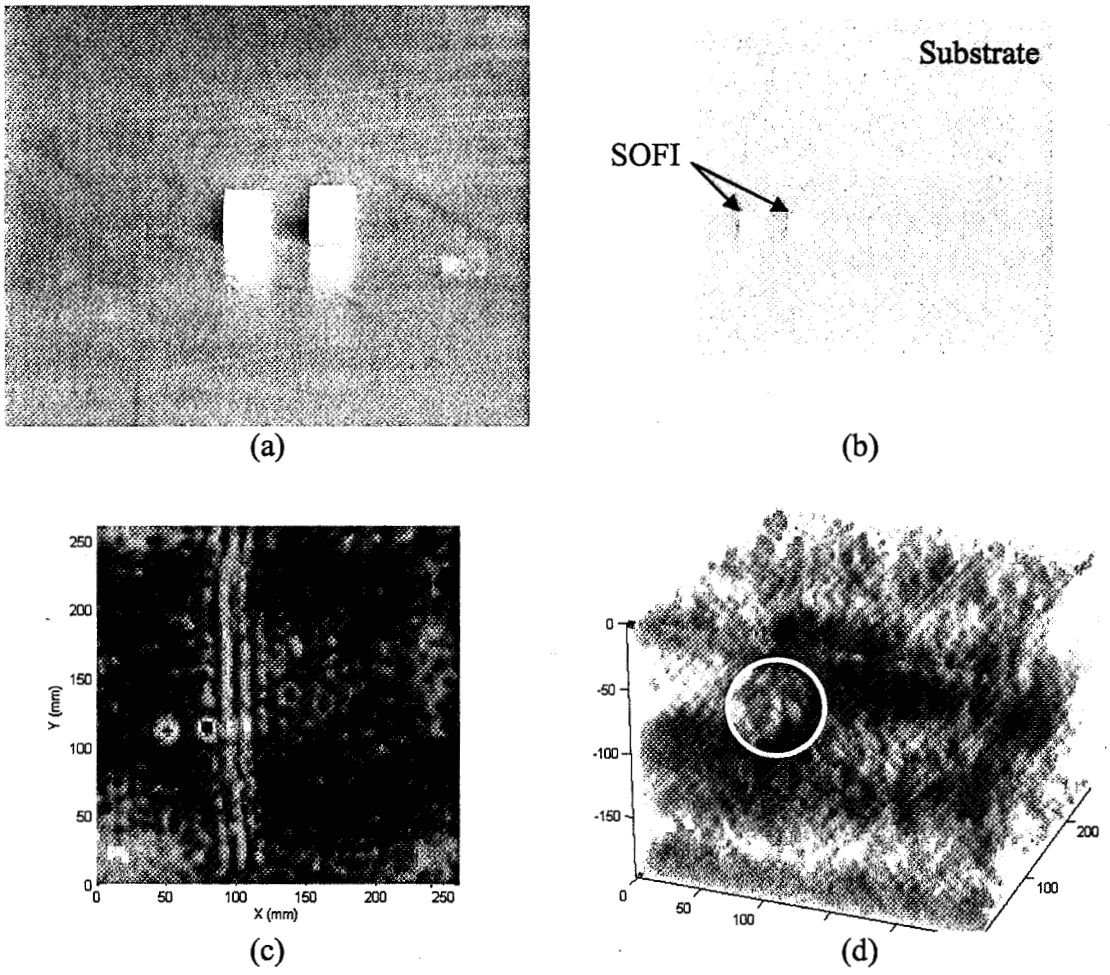

Figure 3.3. Two 0.5-inch SOFI cubes separated by 0.5-inch at Ku-band (12.4-18 GHz): (a) picture of SOFI cubes, (b) arrangement schematic, (c) slice, (d) 3D view.

The last experiment was of one 1-inch cube and two 0.5-inch cubes measured at X-band (8.2-12.4 GHz). Figure 3.4c shows the 1-inch cube distinguished well above the background, however, the two 0.5-inch cubes look like small variations in the background noise. This may be the consequence of the range resolution that at X-band is 36 mm rather than 27 mm due to the reduced bandwidth. The finer range resolution of Ku-band would make the small cubes more pronounced. However, the cubes can still be recognized in the 3D view, as shown in Figure 3.3d. The cubes as represented are locally

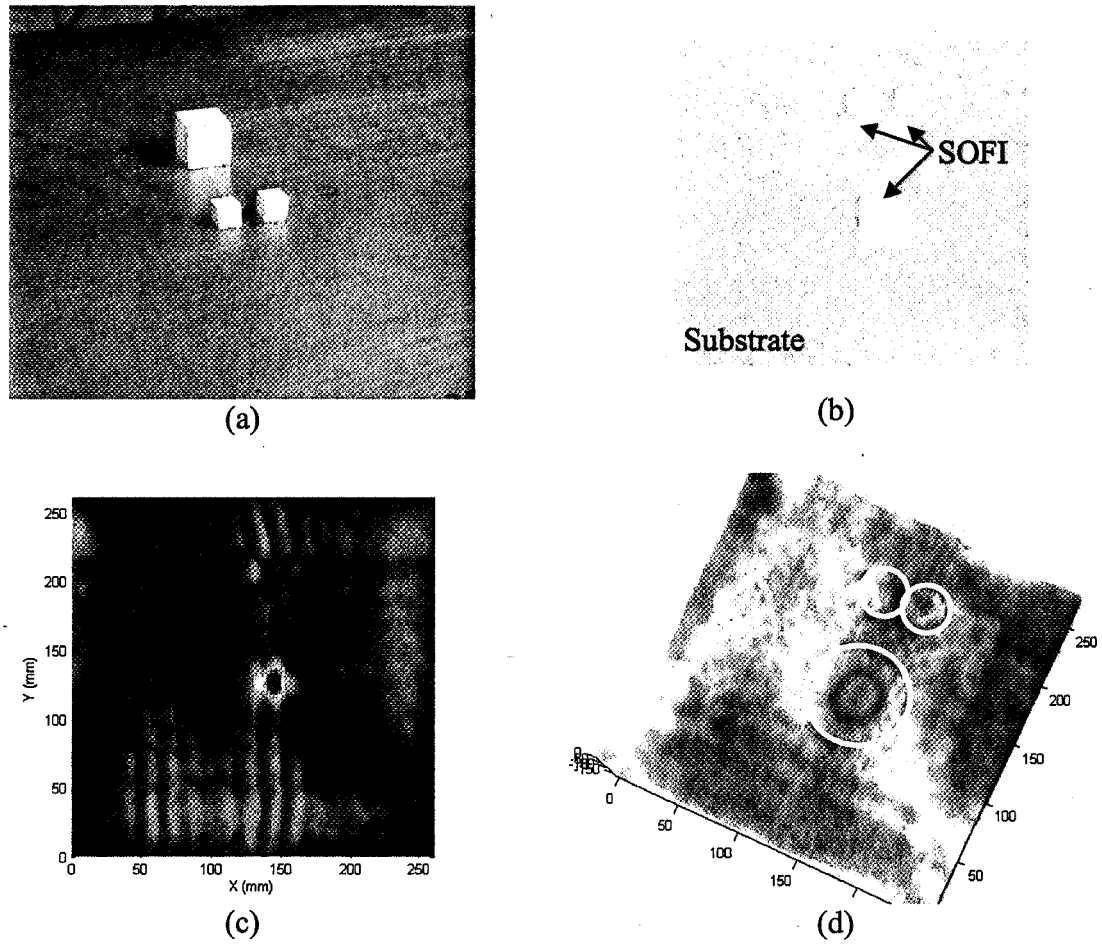

Figure 3.4. One 1-inch cube and two 0.5-inch cubes at X-band (8.2-12.4 GHz): (a) approximate picture of setup, (b) arrangement schematic, (c) slice, (d) 3D view.

opaque, which discriminates them from the background and from contributions of the edges of the aluminum substrate.

These three experiments demonstrated some of the advantages wide-band holography has over FD-SAFT; namely, range resolution and background noise suppression. These advantages provided for better discernment of the scatterers at their location in space and provided for better 2D images of slices of the hologram as compared to FD-SAFT. Consequently, microwave holography continues to outperform FD-SAFT in the coming sections.

3.6. FLAT-BOTTOM HOLES IN SOFI – ONE INCH-DIAMETER

3.6.1. Description/Purpose. After witnessing how microwave holography can outperform FD-SAFT in the detection of SOFI cubes, this section aims to test the method on the identical flat-bottom hole samples as described in Section 2.6.1. As before, the holes had been drilled right to left to the following depths: 1/8 inch (3 mm), 1/4 inch (6 mm), 1/2 inch (13 mm), 3/4 inch (19 mm), and 1 inch (25 mm), see Figure 2.8a. Scans for each experiment were taken at using a K-band rectangular waveguide probe sweeping through 201 frequency points between 18 and 26.5 GHz, at a power level of 0 dBm, a liftoff of 10 mm above the SOFI, and a sampling increment of $\Delta x = 2$ mm. The slabs were arranged in the same three configurations as before: 1) slab with holes face down backed by aluminum substrate (Figure 2.8a), 2) slab with holes face down backed by blank slab and substrate (Figure 2.8b), and 3) slab with holes face down sandwiched by the blank slab on top and the substrate on the bottom (Figure 2.8c). Experiments 1 and 2 would test the effect backing has on hole detection and experiments 1 and 3 would test the effect of adding more SOFI between the holes and the measurement plane, thereby moving the holes further away.

3.6.2. Results. Experiment 1 was the case of the SOFI slab with holes laid face down on the aluminum substrate. The results for microwave holography can be seen in Figure 3.5. A slice of the holographic dataset at 74 mm shows that the four deepest of the five holes can be distinguished, as shown in Figure 3.5a. The last hole was 1/8 inch deep and can only be distinguished after contrast enhancement. It also tends to be masked by edge effects occurring near the left edge. In comparison, the signal from the 1 inch-deep hole on the right is strong enough to overcome the influence of edge effects. Figure 3.5b

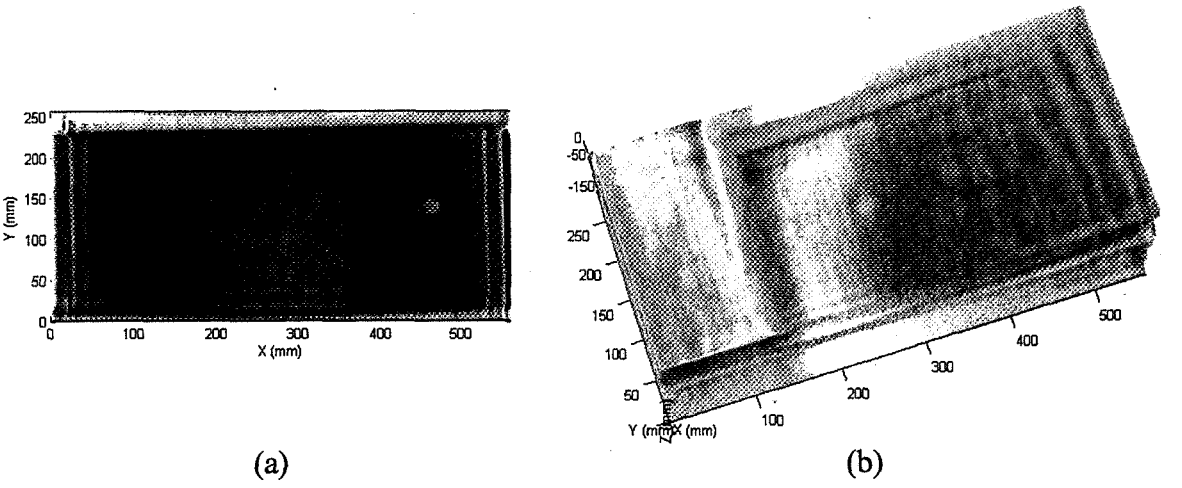

(a) (b)

Figure 3.5. One inch-diameter flat-bottom holes for experiment 1: (a) slice at 74 mm, (b) 3D view.

shows the 3D view of the hologram where the dominant holes can still be recognized. Also, a few of the knit lines near $z = 0$ can be recognized because of their closeness to the measurement plane.

Experiment 2 is where the SOFI slab with holes is backed by the blank slab and substrate. To aid in target recognition and contrast, the outer border of the dataset was cropped to omit part of the edges, as before. However, this has a negative impact of decreasing the width of the array, which was shown to degrade spatial resolution in Section 3.4. The FD-SAFT processed data, as shown in Figure 2.9d, only shows the deepest hole when focused at 76 mm. A slice at 76 mm of the hologram on the other hand shows none, as shown in Figure 3.6a. Only seemingly random variations are observable in the image along with the influence of the edges. However, the signature of the holes appeared in the hologram at a slice corresponding to the surface of the substrate, as shown in Figure 3.6c. For this reason, a slice of the hologram was taken at 152 mm, where the holes were the most distinguished. Four of the five holes can be seen in this

image albeit the hole edges are now blurred. It is important to note that the images of the holes were not best seen at their physical location. Instead, the holes were best seen as shadows cast onto the aluminum substrate. This is an important conclusion since the detection of the presence of a hole in SOFI is possible, however, the depth would not be known for this case. The last hole that was 1/8 inch deep could not be seen because of its apparent low signal and the complications of the edge. The effects of the edge became more pronounced after trimming the dataset as compared to Figure 3.5a.

Experiment 3 is where the SOFI slab with holes was sandwiched by the blank slab and aluminum substrate, which effectively moves the holes away an additional 70 mm

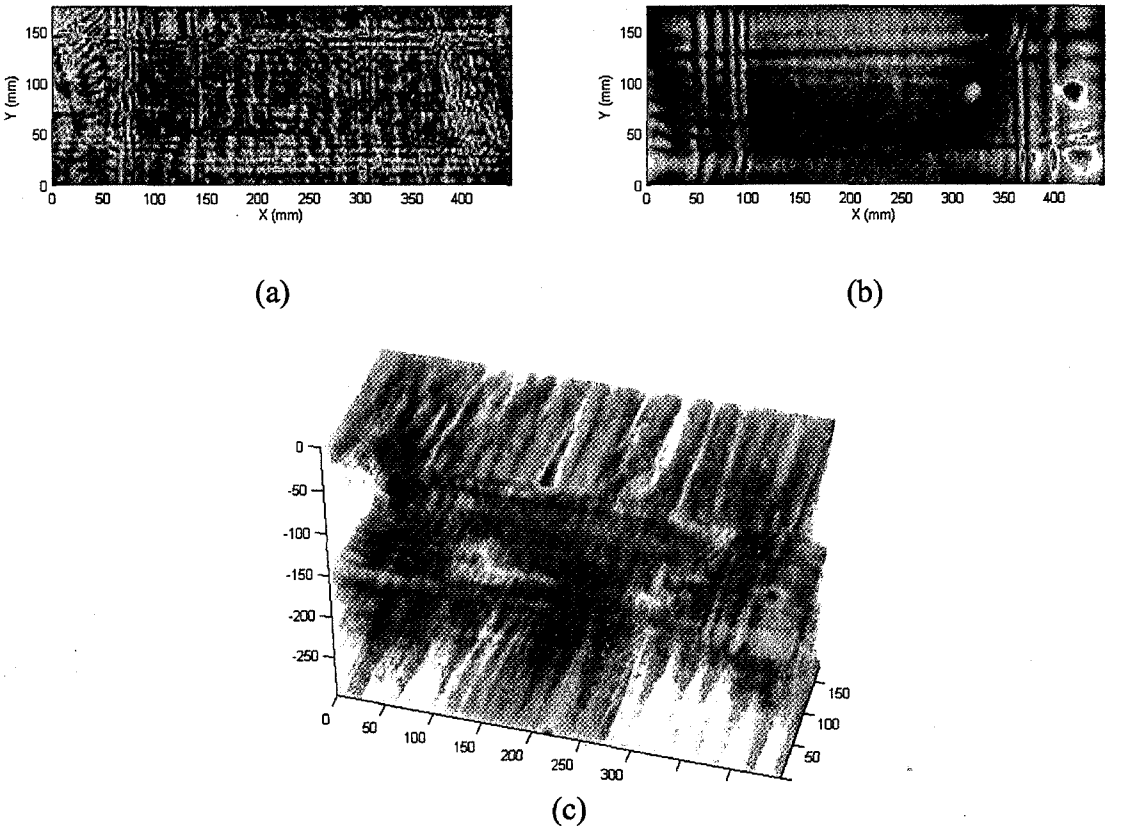

Figure 3.6. One inch-diameter flat-bottom holes for experiment 2: (a) slice at 74 mm, (b) slice at 152 mm, (c) 3D view.

below SOFI as compared to experiment 1. The dataset for this experiment was also cropped as in experiment 2 to aid in target recognition. For this experiment, the power of the received signal was near the end of the range of the particular network analyzer. Previously, FD-SAFT showed no indication of the holes and noise seemed to dominate, as shown in Figure 2.9f. In comparison, a slice of the hologram at 152 mm corresponding to the level of the substrate shows the four deepest of the five holes, as shown in Figure 3.7a. The 3D view also shows the holes in Figure 3.7b. This remarkable increase in target recognition is attributable to the fact that microwave holography has range resolution to compress and augment the signal from a scatterer.

This section demonstrated that the advantages of wide-band microwave holography provide for significant image improvement. This image improvement is remarkable for scatterers far away from the measurement plane where it was demonstrated in experiment 3 that four targets could be distinguished using this method as compared to FD-SAFT, which could distinguish none.

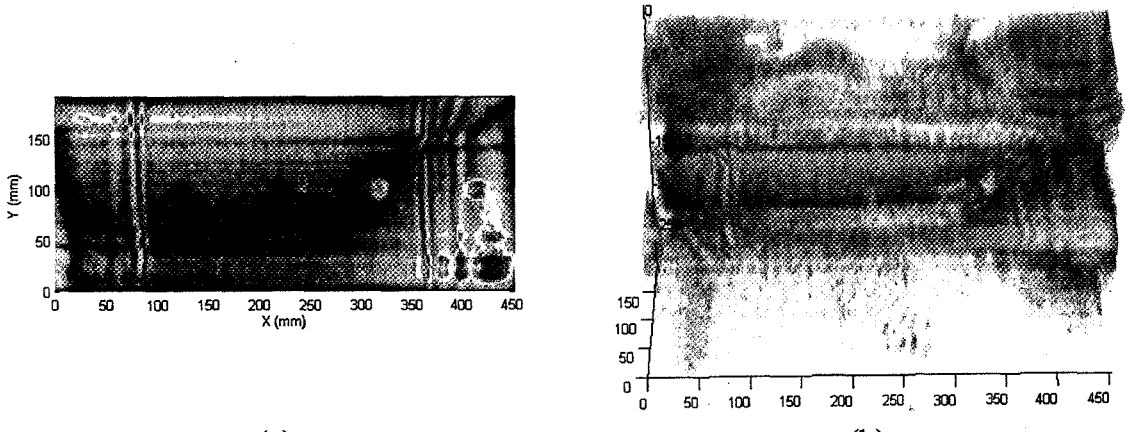

(a) (b)

Figure 3.7. One inch-diameter flat-bottom holes for experiment 3: (a) slice at 152 mm, (b) 3D view.

3.7. FLAT-BOTTOM HOLES IN SOFI – TEST GRID

3.7.1. Description/Purpose. The aim of this experiment was to determine the minimum detectable defect size of air void in SOFI for wide-band microwave holography processing given the frequency of operation (K-band), antenna type (rectangular waveguide probe), displacement of substrate to the measurement plane (86 mm), and dimension of the measurement plane (305 mm). The sample was the same as described in Section 2.7: a 12 inch by 12 inch (305 mm by 305 mm) and 3 inch (76 mm) thick flat-bottom hole sample made with hole diameters (left to right) increasing from 1/8 to 1 inch and drill depths (top to bottom) increasing from 1/8 to 3/4 inch, as shown in Figure 2.10. The strength of the signal reflected from a hole drops for decreasing hole diameter and decreasing hole depth.

Measurements were performed at the NASA facilities using a K-band rectangular waveguide probe sweeping through 201 frequencies between 18 and 26.5 GHz, a scanning increment of $\Delta x = 4$ mm, a liftoff of 10 mm, and a power level of -6 dBm. The probe orientation was such that the polarization of the signal was aligned along the top and bottom edges of the sample. For processing, the dataset was interpolated along the x and y axes to simulate a scanning increment $\Delta x = 2$ mm, and the dataset was cropped to mitigate signals from the edges.

3.7.2. Results. Using these results it is possible to determine the dimensions of the smallest detectable air void in SOFI using wide-band microwave holography at K-band, a rectangular waveguide probe, and a substrate 86 mm away from a measurement plane 305 mm wide. A slice of the hologram at 110 mm from the measurement plane shows the holes best, as shown in Figure 3.8a. Contrasted with Figure 2.11a, Figure 3.8a

has a lower noise level and more holes can be detected. Also, the edge effects on the left and right are more pronounced and less affected by noise. Figure 3.8c shows the distinguished holes in white circles. The location of the holes were known *a priori* so holes were determined to be distinguished so long as they locally disturbed the image. The smallest hole detected was 1/4 inch in diameter and 1/4 inch deep corresponding to a

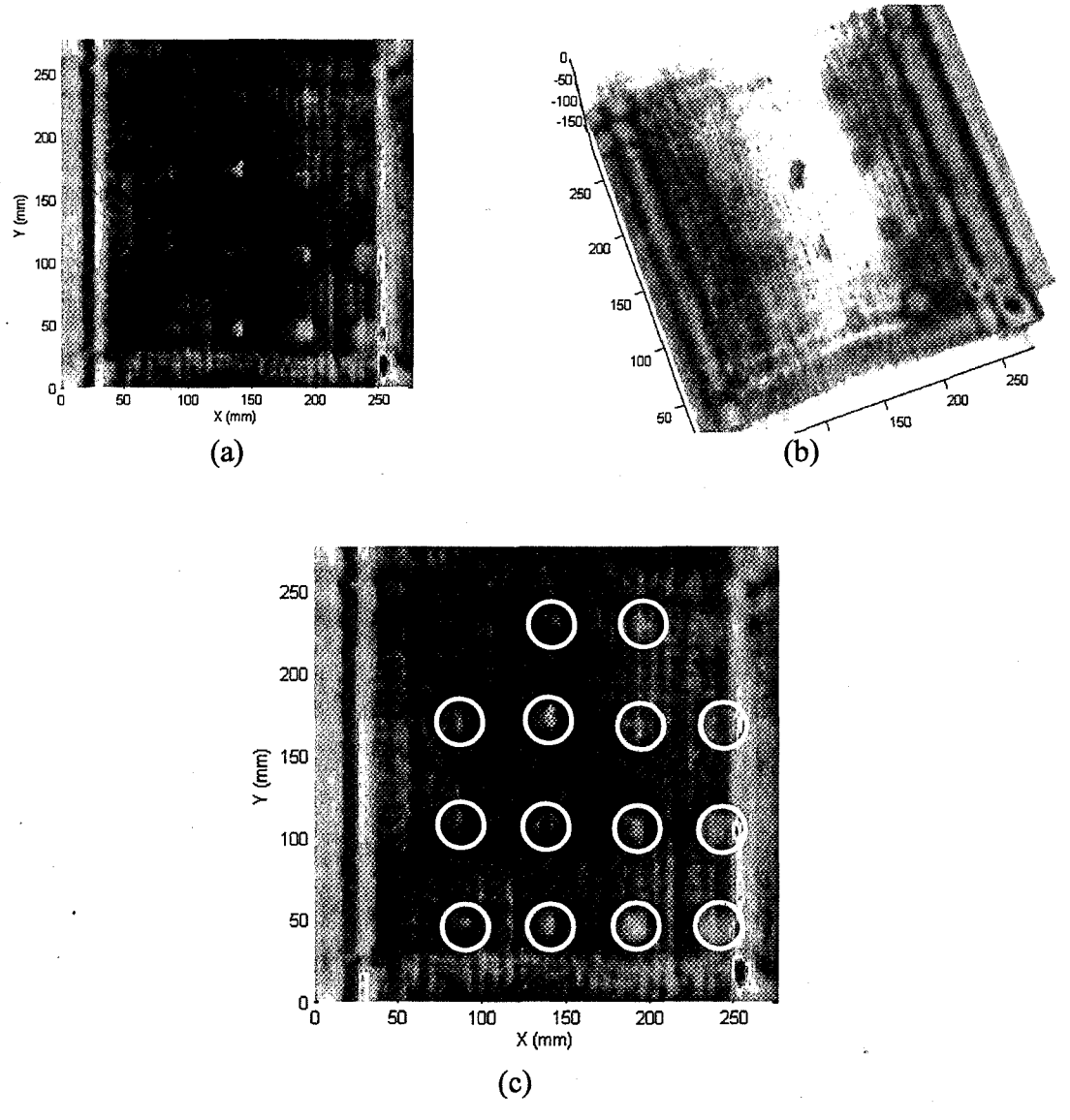

Figure 3.8. Test grid of flat-bottom holes in SOFI: (a) slice at 110 mm, (b) 3D view, (c) slice at 110 mm with defects circled.

volume of 0.01 inch^3 or 0.16 cm^3, which is smaller than the minimum hole detected by FD-SAFT that was 3/4 inch in diameter and 1/4 inch deep corresponding to a volume of 0.1 in^3 or 1.6 cm^3. As shown in Figure 3.8c, all the 1/8 inch-diameter holes were masked by the effects of the left edge. Also, it is important to note that the 1 inch-diameter and 1/8 inch-deep hole was not distinguished, but the 3/4 inch-diameter hole with the same depth was distinguished. This is due to the fact that the 1 inch-diameter hole was masked by edge effects and the 3/4 inch-deep hole was sufficiently far from the edge as to not be masked. The 3D view of the sample can be seen in Figure 3.8b where most of the holes can be seen in colors of opaque blue. In this view angle, some of the holes that blended into the blue background of Figures 3.8a and 3.8c are augmented and opaque in Figure 3.8b.

3.8. STRINGER PANEL – POD 50-R

3.8.1. Description/Purpose. The previous two sections demonstrated how wide-band microwave holography can augment small signals and outperform FD-SAFT for the same cases. This section and the next go a step further to demonstrate the capabilities of range resolution to distinguish specific parts of the stringer panels at different depths. As before in Section 2.8, the specimen selected for this experiment was referred to as the POD 50-R panel, which was designed to resemble a region on the external tank where either the liquid oxygen tank or the liquid hydrogen tank joins the intertank, as shown in Figure 2.12. The panel contained stringers, flanges, their corresponding bolts, and several embedded voids in the SOFI. The measurements were performed at the NASA facilities using a K-band rectangular waveguide probe sweeping through 201 frequency points

between 18 and 26.5 GHz, a scanning increment of $\Delta x = 4$ mm, a liftoff of 10 mm, and a power level of 0 dBm. The scan was performed for two orientations of the probe: one where the signal polarization of the probe was parallel to the length of the stringer or stringer axes and another perpendicular to that.

3.8.2. Results. Results are organized so that the next slice of the hologram is deeper than the previous. The first slice was taken 48 mm away from the measurement plane, which corresponds to the hats of the stringers. These appear as bright red rectangles in Figure 3.9a where the signal is parallel to the stringer axes. The edge effects on the smaller sides of the stringer hats can also be seen. In Figure 3.9b where the signal is perpendicular to the stringer axes, the stringer hat appears as yellow-green rectangles. It is important to note that the rectangles are made up of four closely spaced bright lines corresponding to the dominant edges on the larger sides of the stringer hats. It is also important to note that only the stringer hats show bright in this image since the range resolution is approximately 18 mm as given in Equation 25. However, the top of the flange can be distinguished as a subtle blue rectangle.

A slice of the hologram at 64 mm shows an image corresponding to the top of the flange extending from the top of the image to the bottom, which was not evident in corresponding FD-SAFT images, as shown in Figure 2.13 and 3.9c. This distance is only 16 mm away from the previous slice, which distance is less than the range resolution. For this reason, the stringer hats appear in the same image as the top of the flange, but they are far less pronounced. Figure 3.9c shows the top flange as the brightest feature. It is important to note that the flange is actually four bright lines spaced closely together due to the incident wavefront being cross-polarized to the flange edge. Also, seen in this

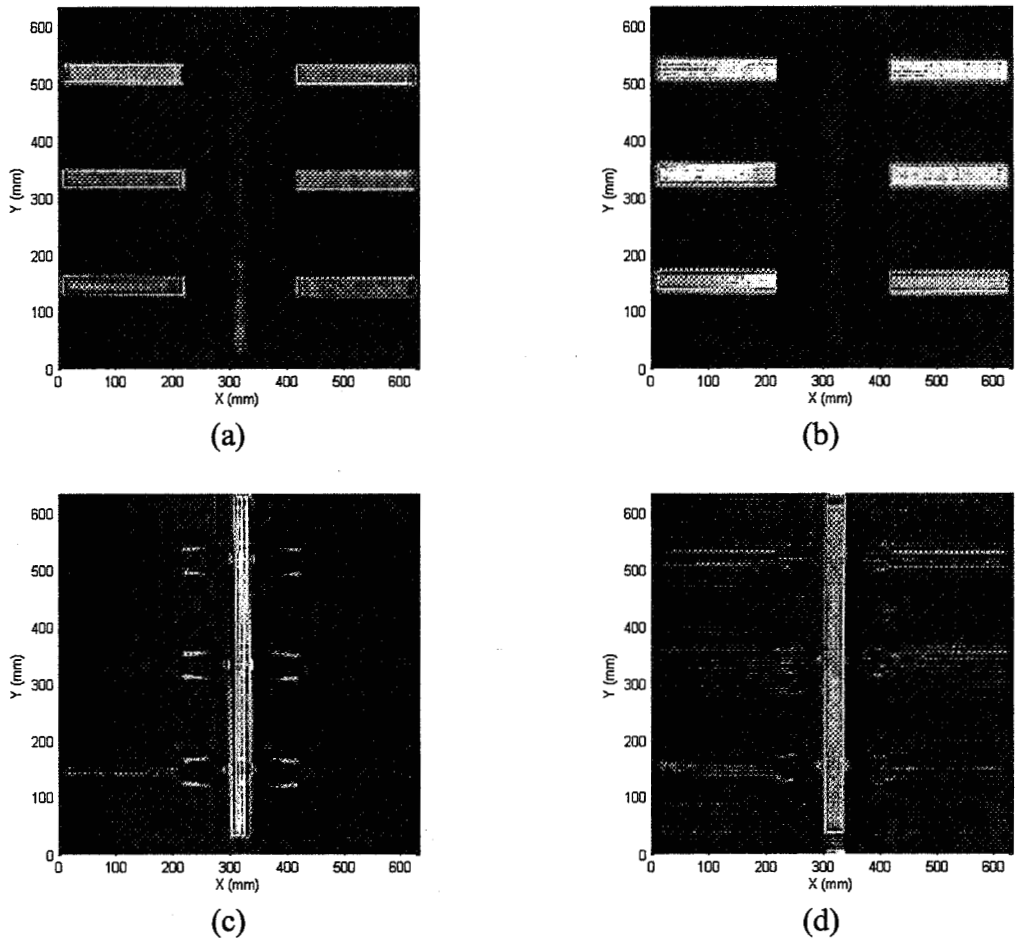

Figure 3.9. Stringer sample POD 50-R holography results: top of hats, slice at 48 mm, (a) parallel to stringer axes, (b) perpendicular to stringer axes; hat openings and flange top, slice at 64 mm, (c) parallel to stringer axes, (d) perpendicular to stringer axes.

image are traces of the flange bolts and stringer openings, which are within the range resolution. Figure 3.9d shows the top of the flange where the signal is perpendicular to the stringer axes. The flange appears flat in color except for the edge effects caused at the top and bottom of the image. The flange bolts appear in this image as well, however, their signal is low due to the polarization of the incident wavefront.

The next slice of the hologram was taken at 76 mm corresponding to the flange bolts, which is only 12 mm from the last slice and within the range resolution. This explains why the bolts can be seen in previous images of the flange top and why the

flange top can be seen here. Direct evidence of the bolts was not evident in corresponding FD-SAFT images, as seen in Figure 2.13. The bolts at this slice are the brightest scatterers, as shown in Figure 3.10a and 3.10b. The stringer hats can also be seen in these figures even though the separation between this slice and the slice of the stringer hats is greater than the range resolution. However, the bolts are relatively low scatterers as compared to other features present because of their size, which allows strong scatterers in close proximity to affect this slice even beyond the range resolution.

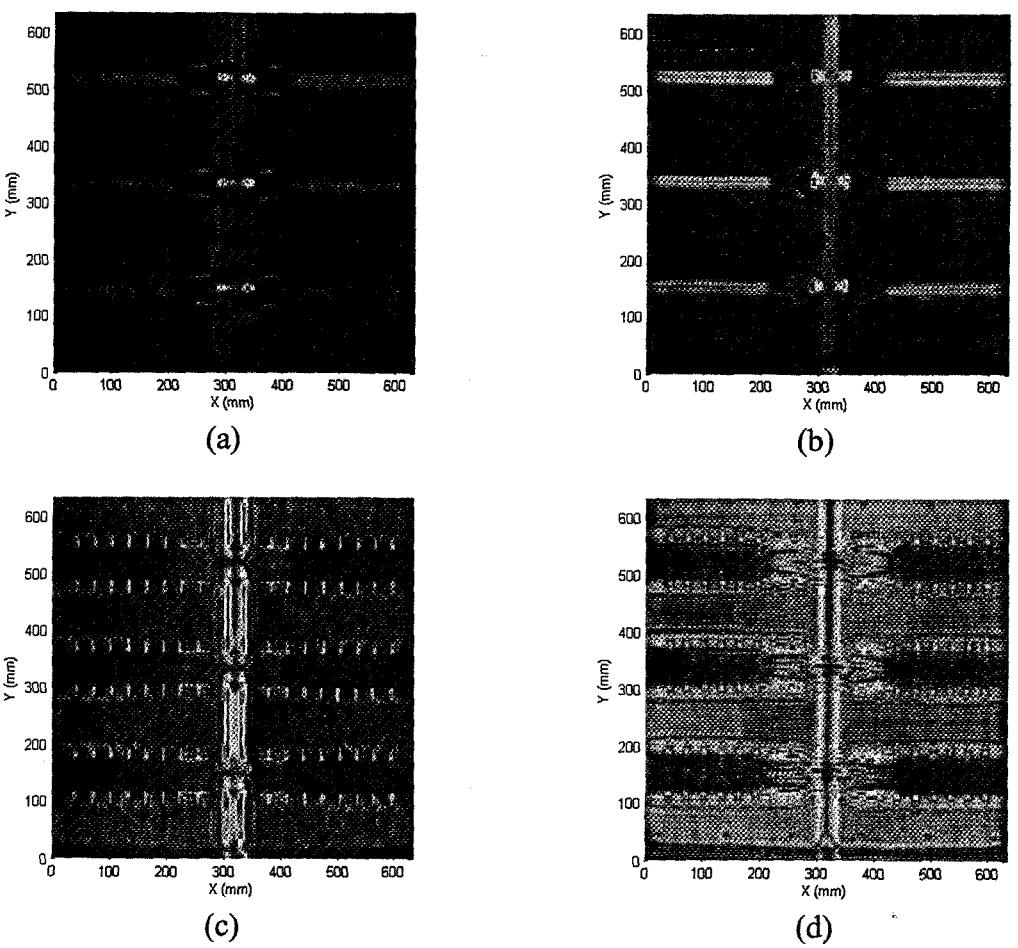

Figure 3.10. Stringer sample POD 50-R holography results: flange bolts, slice at 76 mm, (a) parallel to stringer axes, (b) perpendicular to stringer axes; substrate, slice at 112 mm; (c) parallel to stringer axes, (d) perpendicular to stringer axes.

The last slice of the hologram was taken at 112 mm corresponding to the substrate, which is 36 mm away from the last slice. For the polarization of the signal parallel to the stringer axes the edge where the flange joins the substrate is very bright, as shown in Figure 3.10c. The flange bolts seem to interfere with the image of the flange edge. The flange edge is less pronounced in Figure 3.10d since the incident wave is disturbed less due to it being parallel to the flange edge. Figure 3.10d also shows the stringer openings well, and it is important to note that every stringer bolt can be distinguished in both figures. Furthermore, Figure 3.10d shows the holes at the top and the bottom of the image used to mount panel POD 50-R to the sprayer drum, which are more distinguished in Figure 3.10d as compared to Figure 3.10c.

Two 3D views of the hologram can be seen in Figure 3.11 for both polarizations. These images show the relative strength of all scatterers present. For the polarization of the signal being parallel to the stringer axes the flange edge is by far the brightest feature present, as shown in Figures 3.11a and 3.11c. For the other polarization, it is the stringer hat and the stringer openings that are the brightest, as shown in Figures 3.11b and 3.11d. Also, seen at this polarization are strong false images of stringer bolts occurring beneath the substrate and between stringers. These are created by incident waves reflecting off of the stringer sides, then reflecting off of the stringer bolts, and then adding constructively. This false image is also evident in the parallel polarization case, but it is much weaker compared to the flange edge.

This section demonstrated that range resolution aids in the separation of reflections occurring at different depths. This is beneficial because relatively low scatterers (like the flange bolts) can be separated from larger scatterers (like the

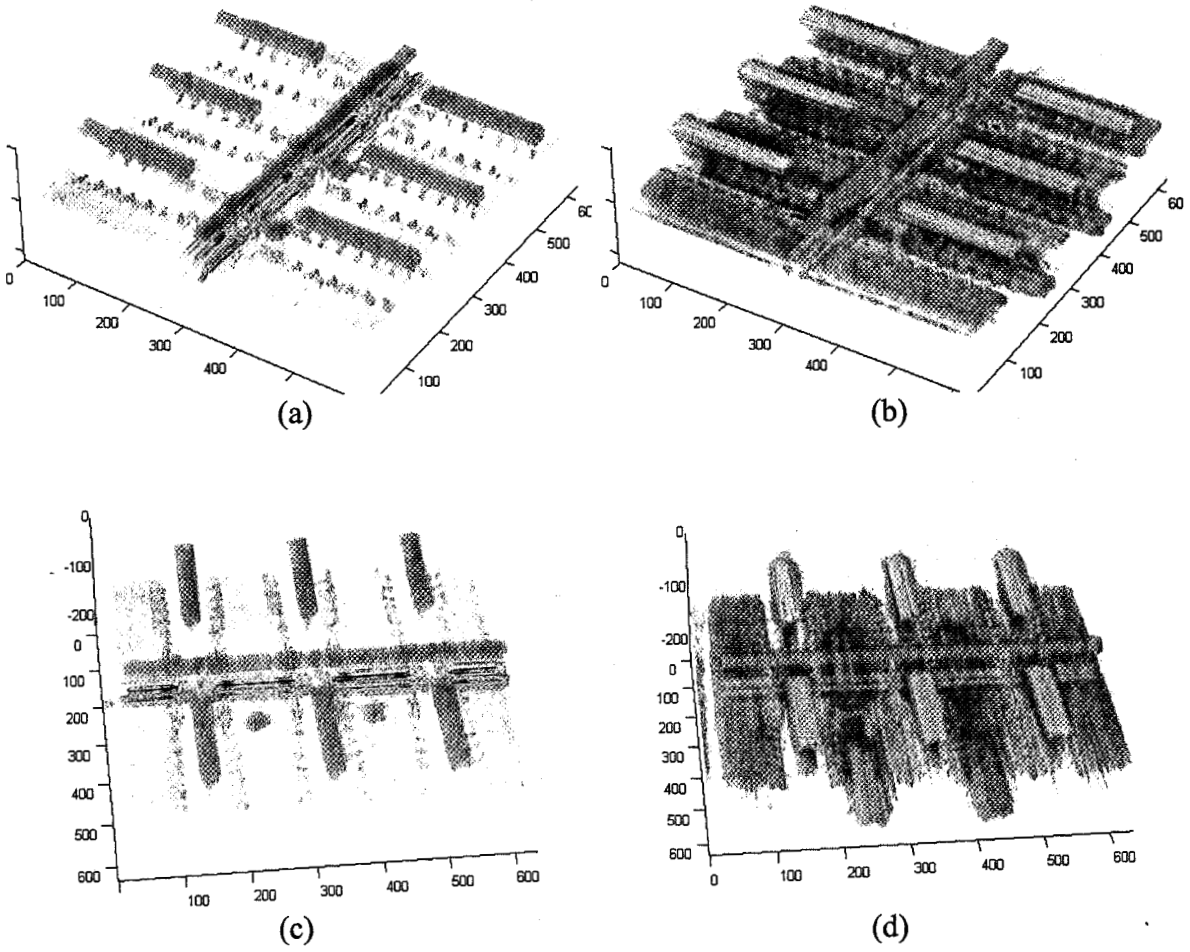

Figure 3.11. Stringer sample POD 50-R holography results: 3D view 1, (a) parallel to stringer axes, (b) perpendicular to stringer axes; 3D view2, (c) parallel to stringer axes, (d) perpendicular to stringer axes.

stringer hat) occurring at another depth. The next section will demonstrate similar results on a panel with natural voids with additional results specific to the sample.

3.9. STRINGER PANEL – NATURAL VOID

3.9.1. Description/Purpose. This sample is similar to the previous case except for the fact that this sample has a ramp of SOFI, which on one end is much thicker than the POD 50-R panel. This pushes the substrate, stringer, and flange farther from the

measurement plane, thereby reducing the strength of the reflected signal from these objects significantly. Therefore, the results of this case will be immediately comparable to the previous case. As before, the measurements were performed at the NASA facilities using a K-band rectangular waveguide probe sweeping through 201 frequency points between 18 and 26.5 GHz, a scanning increment of $\Delta x = 4$ mm, a liftoff of 10 mm, and a power level of 0 dBm. The scan was performed for two orientations of the probe: one where the signal polarization of the probe was parallel to the stringer axes and the other orientation was perpendicular to that.

3.9.2. Results. Results are primarily organized so that the next slice of the hologram is deeper than the previous. The first slice was taken at 168 mm away from the measurement plane, which corresponds to the stringer hats, as shown in Figures 3.12a and 3.12b. Note that this is 120 mm more than the corresponding slice taken of POD 50-R, as shown in Figure 3.9a and 3.9b. For the signal polarization parallel to the stringer axes, the stringer hats appear as bright red and yellow rectangles in Figure 3.12a. The edge effects on the large sides of the stringer hats can be seen in Figure 3.12b similar to before. It is important to note that between this case and the previous the background noise has not significantly increased even though the structure is 120 mm more away.

A slice of the hologram 16 mm deeper at 184 mm shows an image corresponding to the top of the flange extending from the left of the image to the right, as shown in Figures 3.12c and 3.12d. As before, the difference in depth between the slices is less than the range resolution so the stringer hats also appear, but they are far less pronounced. However, the stringer hats are brighter than the corresponding images of POD 50-R, as

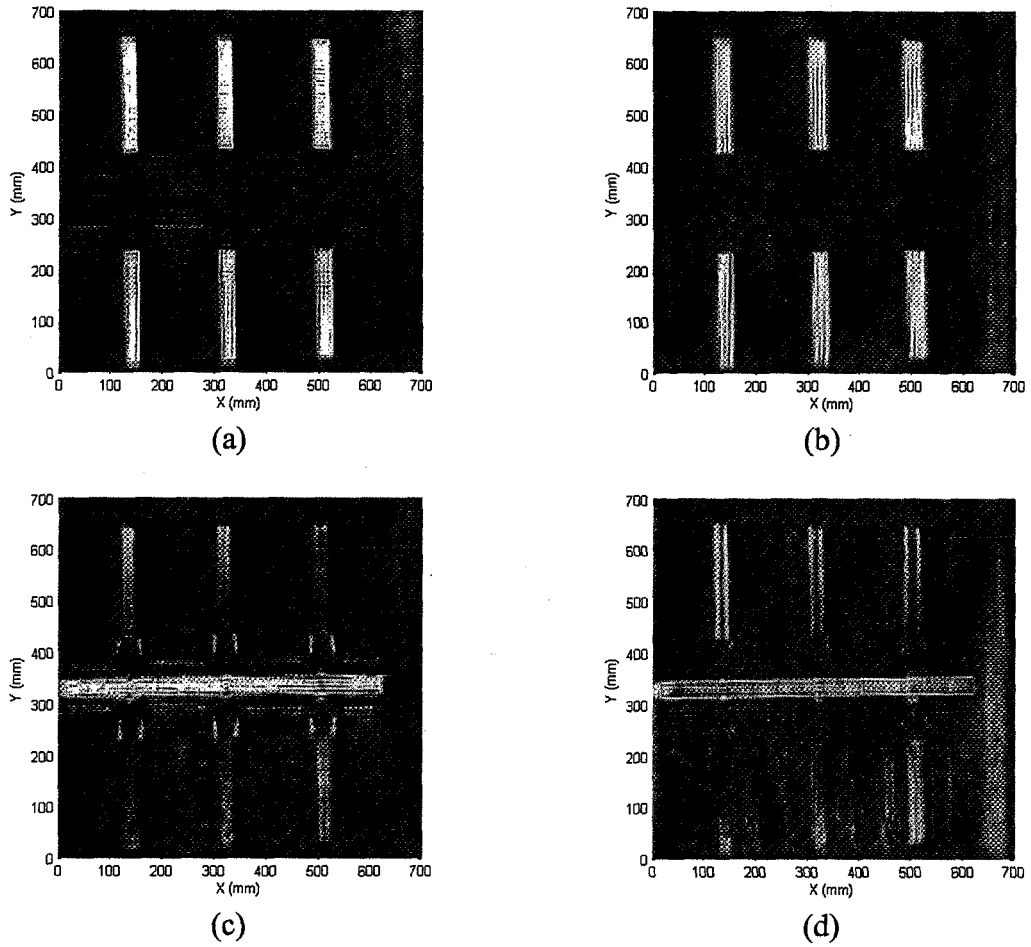

Figure 3.12. Stringer sample natural void holography results: top of hats, slice at 168 mm, (a) parallel to stringer axes, (b) perpendicular to stringer axes; hat openings and flange top, slice at 184 mm, (c) parallel to stringer axes, (d) perpendicular to stringer axes.

shown in Figure 3.9c and 3.9d. Also, seen in this image are traces of the flange bolts and stringer openings.

The next slice of the hologram is 196 mm away from the measurement plane. Figures 3.13a and 3.13b show the flange bolts very well for this slice. As compared to the previous case (Figures 3.10a and 3.10b) the bolts are the one and only strong reflection. Previously, the stringer hat was easily distinguished for the signal polarization perpendicular to the stringer axes.

The last slice directly related to the POD 50-R sample was taken 228 mm away from the measurement plane, which corresponded to the depth of the substrate. Stringer bolts and the flange edge interrupted by flange bolts can be seen in Figure 3.13c. Figure 3.13d additionally shows the stringer openings for the other polarization of the signal. Even though the measurement plane was 120 mm farther away than the previous case the current images are immediately comparable to the case of POD 50-R, as shown in Figures 3.10c and 3.10d. It is important to note that the increased height did not

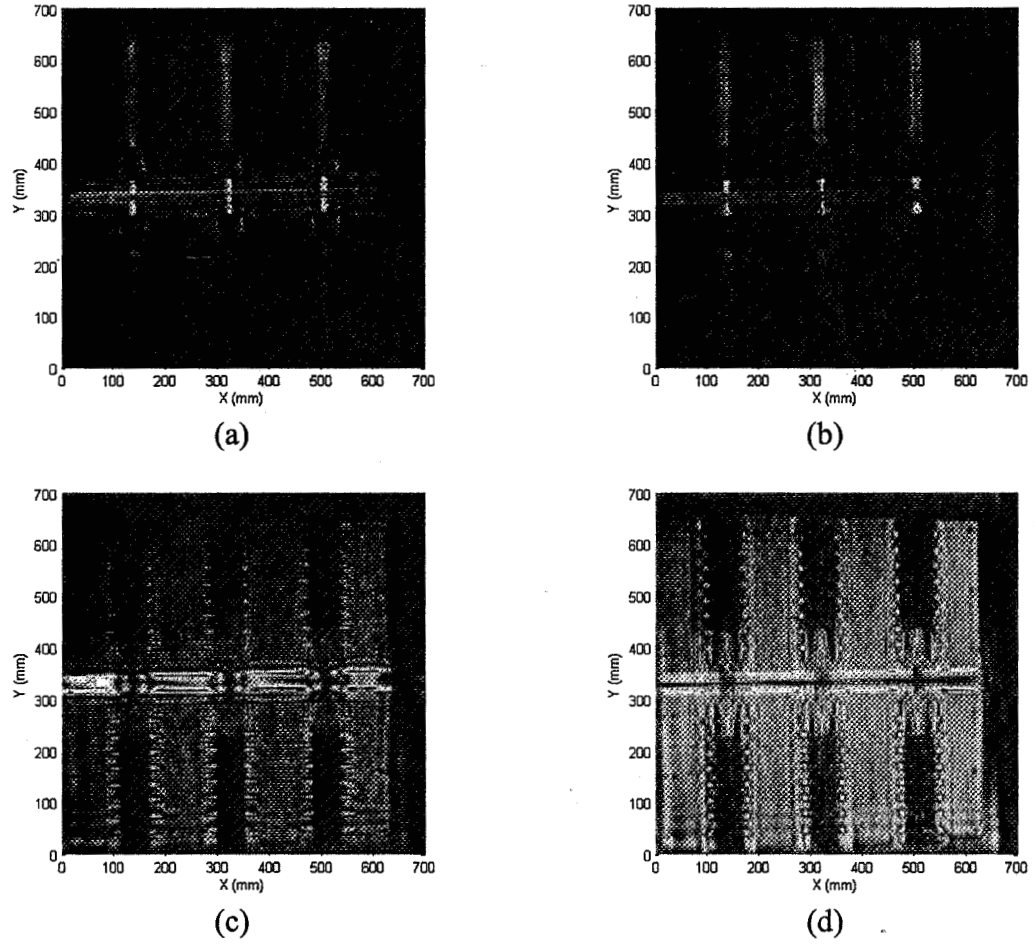

Figure 3.13. Stringer sample natural void holography results: flange bolts, slice at 196 mm, (a) parallel to stringer axes, (b) perpendicular to stringer axes; substrate, slice at 228 mm; (c) parallel to stringer axes, (d) perpendicular to stringer axes.

significantly reduce the reflected signal of the scatterers neither did it introduce much clutter into the image.

The 3D representations of the hologram show again that the dominant scatterer for the signal polarization parallel to the stringer axes is the flange edge (Figure 3.14a) and the dominant scatterers for the other polarization were the stringer tops and stringer

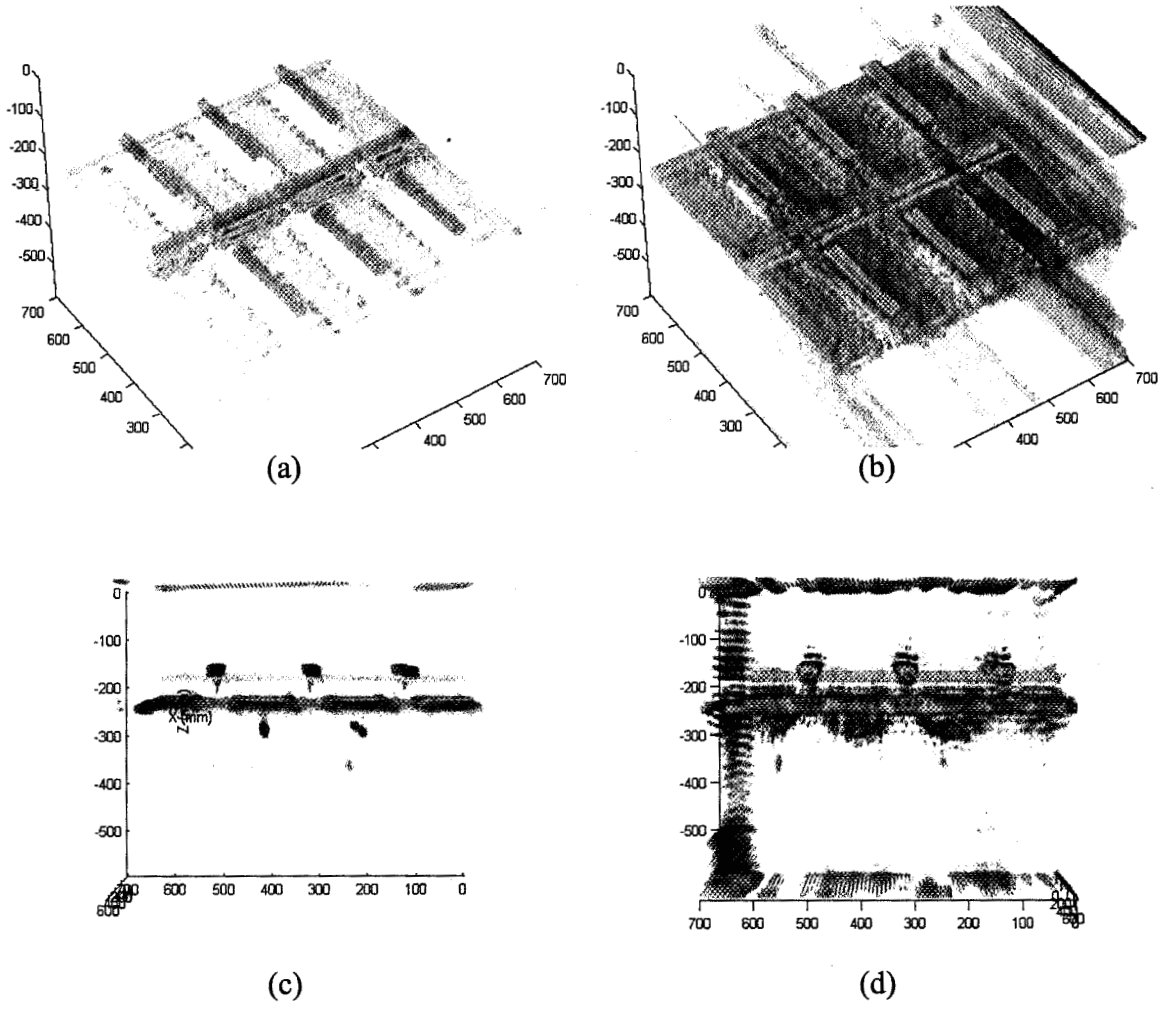

Figure 3.14. Stringer sample natural void holography results: 3D view 1, (a) parallel to stringer axes, (b) perpendicular to stringer axes; 3D view 2, (c) parallel to stringer axes, (d) perpendicular to stringer axes.

openings (Figure 3.14b). However, false images of the stringer bolts again appear between the stringers and below the substrate, as shown in Figures 3.14c and 3.14d.

Figures 3.14c and 3.14d also show the appearance of a false image seemingly occurring at about 350 mm, well below the level of the substrate. The natural void panel had no schematic indicating defects so it was not known what physical defect these reflections corresponded to. If this false image was caused by the specular reflection of a defect occurring above the substrate, the defect would have to occur at about 100 mm,

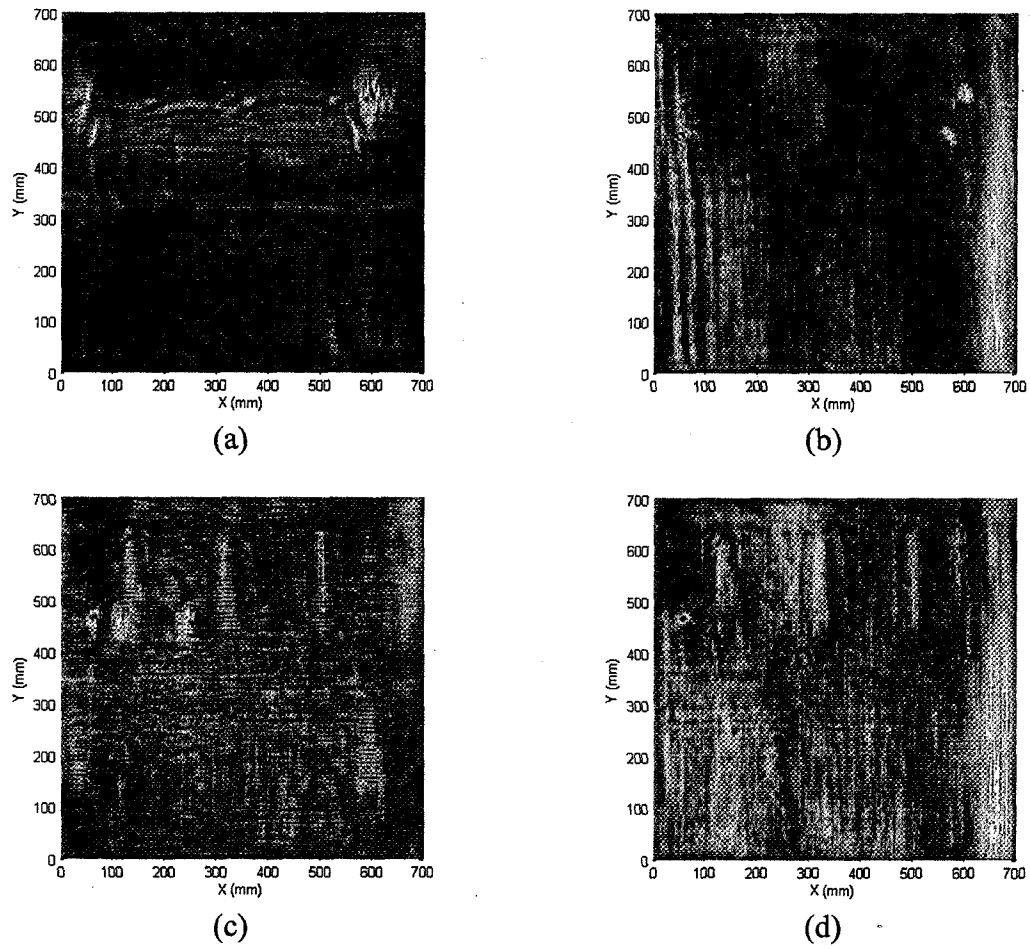

Figure 3.15. Stringer sample natural void holography results: defect observed at 36 mm, (a) parallel to stringer axes, (b) perpendicular to stringer axes; defect observed at 112 mm, (c) parallel to stringer axes, (d) perpendicular to stringer axes.

and something does occur in this general region. Two slices of the hologram are shown at 36 mm and 112 mm below the measurement plane, as shown in Figure 3.15. These images show small bright regions located toward the top of the images. They seem to exist without any order, however, the false image occurring beneath the substrate seems to provide more meaning.

Below the surface of the substrate, slices were taken at 336, 352, and 392 mm from the measurement plane, as shown in Figure 3.16. Here the false image resembles a rod or a cylinder particularly identifiable in Figures 3.16c and 3.16d. If it is caused by an object above the substrate, it scatters more for signals polarized perpendicular to the stringer axes. However, the ends of the rod-like indication appear equal in magnitude for each signal polarization. The rod-like indication blurs out of recognition if slices are taken too far above (Figures 3.16a and 3.16b) or too far below the appearance of the indication (Figures 3.16e and 3.16f).

3.10. SUMMARY

This section primarily showed how wide-band microwave holography can overcome the three main weaknesses of FD-SAFT: 1) the focus height must be known *a priori*, 2) poor performance for low signal power levels, and 3) no range resolution is associated with FD-SAFT. The first issue is resolved since wide-band holography produces a dataset at many depths by transforming the frequency sweep to information along the z-axis. The second and the third issues are resolved by range resolution. Range resolution not only allows defects to be found in three dimensions but it also compresses and strengths the signal to its source location in three dimensions.

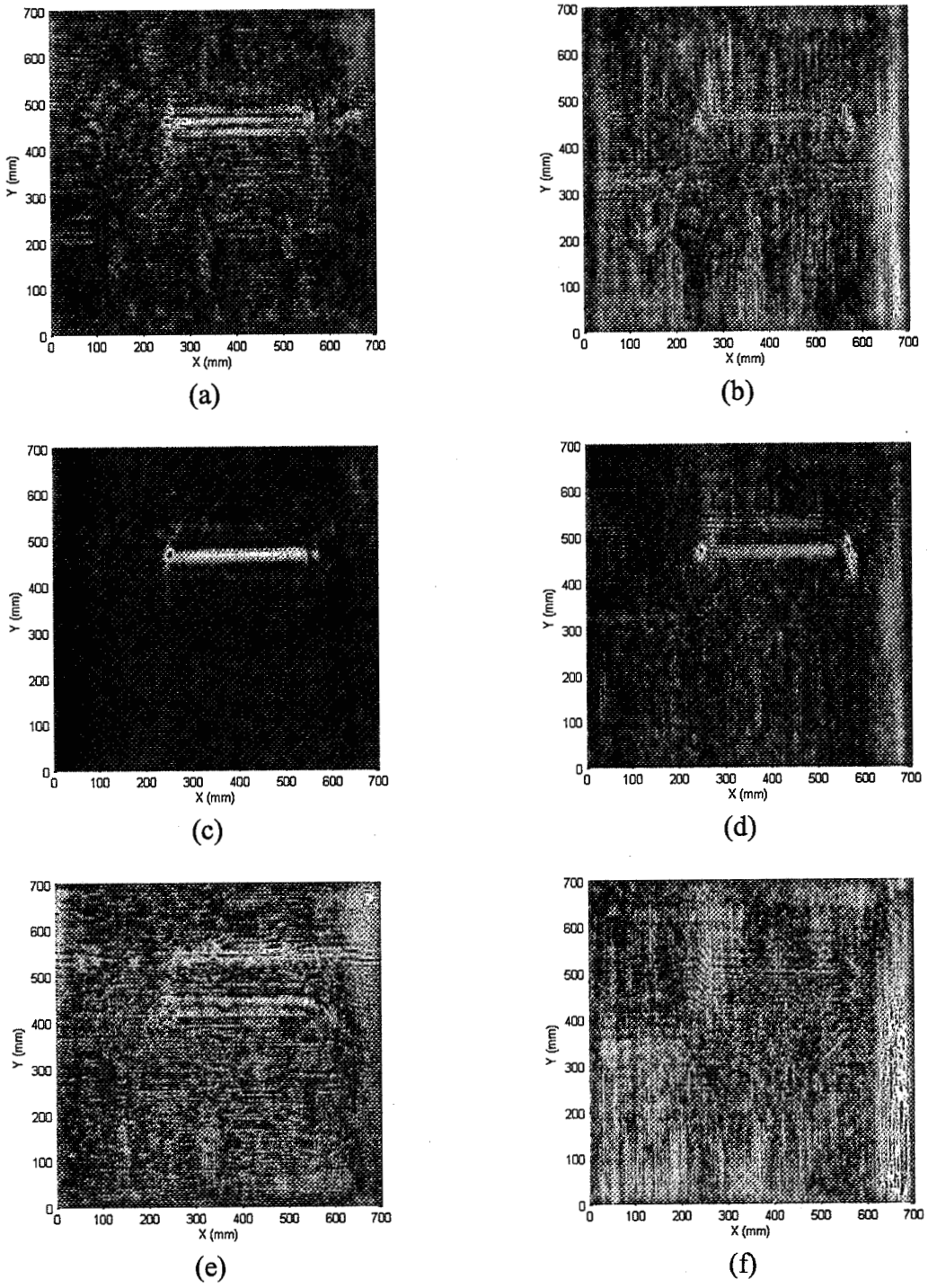

Figure 3.16. Stringer sample natural void holography results of a rod-like false image: observed at 336 mm, (a) parallel to stringer axes, (b) perpendicular to stringer axes; observed at 352 mm, (c) parallel to stringer axes, (d) perpendicular to stringer axes; observed at 392 mm, (e) parallel to stringer axes, (f) perpendicular to stringer axes.

The several cases described in Sections 3.5 – 3.9 illustrated the specific advantages that wide-band microwave holography has over FD-SAFT. The scans of SOFI cubes showed how microwave holography suppresses background noise. The case of 1 inch-diameter flat-bottom holes showed that air voids could be seen in SOFI for long distances. The scan on the flat-bottom hole test grid showed that the smallest detectable volume was a 0.01 in^3 (0.16 cm^3) volume with a 1/4 inch (6 mm) diameter and depth of 1/4 inch (6 mm) using a frequency sweep of 201 points from 18 to 26.5 GHz, a K-band rectangular waveguide probe, the substrate 86 mm away, and a scan dimension w of 305 mm. The last two cases included stringer panels modeled after the external tank of the Space Shuttle where one panel had embedded voids (POD 50-R) and the other had natural voids. These cases showed that range resolution could provide much more detail about the sample under test. Features observed directly and distinguished at different levels in the image include the stringer hats, flange top, flange bolts, stringer openings, stringer bolts, and substrate. The next section will discuss the advantages and disadvantages of both methods with a description of future work to improve detection of small scatterers.

4. SUMMARY AND DISCUSSION

4.1. BACKGROUND

Microwave and millimeter wave nondestructive testing and evaluation (NDT&E) methods have shown great potential for determining material composition in composite structures, determining material thickness or debond thickness between two layers, and determining the location and size of flaws, defects, and anomalies. For example, microwave NDT&E methods have been used to detect the presence of chlorides in concrete, the effects of loading in concrete, grout in masonry, and corrosion under paint to name a few.

The same testing methods have also shown great potential to produce relatively high-resolution images of voids inside Spray On Foam Insulation (SOFI) test panels using real focused methods employing lens antennas. SOFI is used as part of the Thermal Protection System on the external tank of the Space Shuttle to insulate and protect the fuel tanks and critical sections. An alternative to real focusing methods are synthetic focusing methods. The essence of synthetic focusing is to match the phase of the signal originating at an arbitrarily located target to measured points spaced regularly on a plane. For a signal originating at that target processed signals add constructively and for all surrounding points they add destructively, consequently providing significant spatial discrimination and resulting in a high-resolution image.

At times it is more advantageous to use synthetic focused methods as opposed to real focused methods, and vice versa. For instance, one may use synthetic focused methods to produce a hologram using inexpensive rectangular waveguide probes as opposed to using an expensive lens antenna capable of generating a two dimensional

image. However, it may be advantageous to use the lens antenna since it does not require image processing. Many variations of synthetic focusing methods have already been developed for radars, ultrasonic testing applications, and microwave concealed weapon detection. For this Thesis, two synthetic focusing methods were investigated; namely, a) frequency-domain synthetic aperture focusing technique (FD-SAFT), and b) wide-band microwave holography. These methods were applied towards materials whose defects were of low dielectric contrast (i.e., weakly scattering); namely, an air void in SOFI.

It is important to note that this investigation used relatively low frequencies in X-band (8.2-12.4 GHz), Ku-band (12.4-18 GHz), and K-band (18-26.5 GHz) that are not conducive for direct imaging of the SOFI. However, as was shown, the image processing methods produced reasonably high resolution images even at these relatively low frequencies. The ultimate goal of this work has been to demonstrate the capability of these methods before they are applied to much higher frequencies such as the millimeter wave frequency spectrum (e.g., 30-300 GHz).

4.2. MICROWAVE MEASUREMENTS

Two different measurement facilities were used in the course of this investigation: one at the Applied Microwave Nondestructive Testing Laboratory (*amntl*) and the other at the NASA Marshall Space Flight Center. The first setup included a scanning table in conjunction with a HP8510C Vector Network Analyzer capable of making full vector measurements up to 18 GHz. The second setup included a moving head scanner in conjunction with an Agilent E8361A PNA Series Network Analyzer capable of making measurements up to 325 GHz, but scanning was limited to frequencies in K-band.

Measurements were taken of five increasing complex cases used to investigate the capabilities of both processing methods. FD-SAFT processing provided images focused at a specified distance away from the measurement plane known *a priori*. Microwave holography provided full three dimensional holograms of the data. Additionally, slices of the hologram were extracted at specified distances away from the measurement plane. The first case was of SOFI cubes arranged on a substrate which showed that the network analyzer could detect the boundary between air and SOFI. FD-SAFT processing showed that the cubes could be resolved and microwave holography also showed that the cubes could be resolved. Furthermore, it was shown that the method suppressed the background noise variations. The second case was of five 1 inch-diameter flat bottom holes in SOFI with depths varying between 1/8 inch and 1 inch. FD-SAFT could not distinguish the holes at a long distance, however, microwave holography could distinguish four of the five holes at a long distance, which shows clearly that the method can detect small signals well. To further investigate the performance of the methods on small signals, the third case was of a SOFI sample with 20 holes of diameters between 1/8 inch and 1 inch and depths 1/8 inch and 3/4 inch. The smallest hole that could be distinguished by the two methods were for FD-SAFT a diameter of 3/4 inch (19 mm) and depth of 1/4 inch (6 mm) and for microwave holography a diameter of 1/4 inch (6 mm) and depth of 1/4 inch (6 mm). The last two cases were of SOFI samples similar to the external tank of the Space Shuttle, namely; the POD 50-R panel and the natural void panel. Results for both cases using FD-SAFT processing showed that the substrate, stringer hats, flange edge, stringer bolts, and indirect evidence of the flange bolts could be distinguished. Microwave holography also showed the stringer hats, flange edge, and stringer bolts, and

it additionally showed the stringer openings and direct evidence of the flange bolts. Furthermore, the method also resulted in the background noise variations being suppressed.

The advantages and disadvantages of both methods were studied through the investigation of these cases. FD-SAFT has an advantage over wide-band microwave holography in that it only requires a single frequency reflection measurement. Also, the method requires little processing time (less than 100 ms) since it extensively utilizes the Fast Fourier transform algorithm. Microwave holography is slower since it requires longer processing times, however, it possesses range resolution. Range resolution allows scatterers to be separated from others in three dimensional space so that small scatterers can be distinguished from large scatterers. Range resolution also provides for the augmentation of small signals at their origin in three dimensional space lifting them far above the noise level. FD-SAFT has no range resolution so that the signal is effectively blurred along the z-axes and the signal is weaker.

4.3. FUTURE WORK

The microwave frequencies utilized in this investigation were between 8.2 GHz and 26.5 GHz, which have relatively long wavelength. The same methods with no modification can be applied to data obtained at higher frequencies. Facilities at NASA's Marshall Space Flight Center will soon provide for a scanning table capable of measurements using the WR03 rectangular waveguide probe operating at frequencies from 220 GHz to 325 GHz. The increased frequency and bandwidth will provide previously unobtainable spatial and range resolutions.

The analysis software of FD-SAFT images and holographic slices may be improved by enhancing the contrast of the image locally. An attempt was made to crop the dataset prior to synthetic focusing, however, this reduced the effective array aperture size and reduced the image resolution. Enhancing the image after processing could provide the means to better distinguish small scatterers from large scatterers.

The analysis of holograms could be improved if a fly-through program were made, such that the user could move in and out of the hologram, rotate, and zoom at will. This would enable the user to move through the hologram and omit obstructions of view to expose more interesting locations of the hologram. Also, possible with this fly-through program is local contrast enhancement of color and transparency values so that small scatterers may be augmented in the user's view. One could also cause a section of a volumetric object to be omitted such that a cross section of the object could be seen as if the object were sliced in two.

Rather than improving the analysis software, an attempt could be made to improve the methods themselves and possibly develop an original method. As described in the Thesis, both FD-SAFT and wide-band microwave holography methods only produce images of the same x and y dimensions as that of the measurement plane. If processed images could extend beyond that of the size of the measurement plane, then much more information could be gained from a single measurement. However, computed points beyond the size of the measurement plane would suffer in resolution and signal detection since the signal will not contribute to all measured locations. However, the resultant image is still powerful since it would resemble an image generated by the human eye. Detailed information available at the center of the image produced by the

eye's retina could correspond to the detailed portion of the data generated by this method. The additional information surrounding this central image would give the indication of objects that could be brought into view at the center of the image at the will of the user. Therefore, the method could provide an extended field of view with detailed information located at the center of the image. Its usefulness would be better realized in a real time scanning system.

APPENDIX.
PROGRAM CODE FOR (EMSAF)

The following is the Matlab programming code for EMSAF, which stands for electromagnetic synthetic aperture focusing. This is a program written for Matlab that utilizes the graphical user interface (GUI), which was edited in the GUI developer environment (GUIDE). However, the code is not shown in its totality, rather, only the most important functions are shown including functions for variable definitions, workspace generation, calculation, and rendering. Some functions shown are edited to omit extensive GUI references.

```
%% Variable definitions and initialization
% --------------------------------------------------------------------
function emsaf_OpeningFcn(hObject, eventdata, handles, varargin)
% This function has no output args, see OutputFcn.
% hObject    handle to figure
% eventdata  reserved - to be defined in a future version of MATLAB
% handles    structure with handles and user data (see GUIDATA)
% varargin   command line arguments to emsaf_export (see VARARGIN)

% Choose default command line output for emsaf_export
handles.output = hObject;

% Update handles structure
workspace.strProgramName = 'Electromagnetic SAF';
workspace.strProgramVersion = '0.3';
workspace.strProgramDate = '2005/06/29';
workspace.strProgramAuthor = 'Toby Case';
workspace.strProgramTitle = [workspace.strProgramName, ' v',
workspace.strProgramVersion];
set(handles.SAFProgram, 'Name', workspace.strProgramTitle);
workspace.strWorkspaceFileName = '';
workspace.strWorkspacePathName = '';

% Define Workspace Variables
workspace.constant.dC_mmGHz = 3e2;
workspace.constant.dC_mmHz = 3e11;
workspace.strFileName = '';
workspace.strPathName = '';
workspace.dIncrX = 2.5; % mm
workspace.dIncrY = 2.5; % mm
workspace.dFocusHeight = 100; % mm
workspace.dFocusHeightRange = 200; % mm
workspace.dApertureSizeX = 10; % mm % 7.9; % 10.16; % mm
workspace.dApertureSizeY = 10; % mm % 15.8; % 22.86; % mm
workspace.strCalculationMethod = 'FDSAFTBusse'; % DirectSingleFrequency, FDSAFTBusse,
MFSAFTBusse

workspace.iX = 0;
workspace.iY = 0;
workspace.iZ = 0;
workspace.iF = 0;
```

```
workspace.acData = zeros(0,0,0); % iX, iY, iF
workspace.mcImg = zeros(0,0); % iX, iY
workspace.mcSAF = zeros(0,0); % iX, iY
workspace.vdF = zeros(0,0); % iF
workspace.vdX = zeros(0,0); % iX
workspace.vdY = zeros(0,0); % iY
workspace.vdZ = zeros(0,0); % iZ
workspace.vdXImg = zeros(0,0); % iX
workspace.vdYImg = zeros(0,0); % iY
workspace.vdXSAF = zeros(0,0); % iX
workspace.vdYSAF = zeros(0,0); % iY

workspace.strInterpolate = 'linear';
workspace.strSubtractConstant = 'mean'; % zero, mean, upperleft, upperright, lowerleft,
lowerright, custom
workspace.strEnforceSpotSize = 'off';
workspace.bAutomaticallyCalculate = 1;
workspace.bShowPlotUnits = 1;
workspace.bShowPlotTitles = 1;
workspace.bShowPlotAxesLabels = 1;
workspace.dTitleFontSize = 18;
workspace.dSAFSampling = 1;
workspace.dDataSampling = 1;
workspace.dCurrentPlot = 1;

% define plots in workspace
% upperleft = 1
workspace.Plot(1).strContent = 'orgmag'; % orgmag, orgphs, safmag, safphs
workspace.Plot(1).aContent = zeros(0,0);
workspace.Plot(1).strColorMap = 'default'; % many
workspace.Plot(1).strType = 'bitmap'; % bitmap, surface, contour
workspace.Plot(1).strTitle = 'Original Magnitude';
workspace.Plot(1).vdX = zeros(0,0);
workspace.Plot(1).vdY = zeros(0,0);
workspace.Plot(1).vdZ = zeros(0,0);
workspace.Plot(1).strMagnitudeUnit = 'linear';
workspace.Plot(1).strPhaseUnit = 'deg180';
workspace.Plot(1).figAxes = handles.PlotUpperLeft;
workspace.Plot(1).ContextMenu = uicontextmenu('Callback',
['emsaf(''ContextPlotMenu_Callback'',gcbo,[],guidata(gcbo), 1)']);
workspace.Plot(1).figSurface = contour(zeros(0,0));


% upperright = 2
workspace.Plot(2) = workspace.Plot(1);
workspace.Plot(2).strContent = 'safmag';
workspace.Plot(2).strTitle = 'SAF Magnitude';
workspace.Plot(2).figAxes = handles.PlotUpperRight;
workspace.Plot(2).ContextMenu = uicontextmenu('Callback',
['emsaf(''ContextPlotMenu_Callback'',gcbo,[],guidata(gcbo), 2)']);
workspace.Plot(2).figSurface = contour(zeros(0,0));

% lowerleft = 3
workspace.Plot(3) = workspace.Plot(1);
workspace.Plot(3).strContent = 'orgphs';
workspace.Plot(3).strTitle = 'Original Phase';
workspace.Plot(3).figAxes = handles.PlotLowerLeft;
workspace.Plot(3).ContextMenu = uicontextmenu('Callback',
['emsaf(''ContextPlotMenu_Callback'',gcbo,[],guidata(gcbo), 3)']);
workspace.Plot(3).figSurface = contour(zeros(0,0));

% lowerright = 4
workspace.Plot(4) = workspace.Plot(1);
workspace.Plot(4).strContent = 'safphs';
workspace.Plot(4).strTitle = 'SAF Phase';
workspace.Plot(4).figAxes = handles.PlotLowerRight;
workspace.Plot(4).ContextMenu = uicontextmenu('Callback',
['emsaf(''ContextPlotMenu_Callback'',gcbo,[],guidata(gcbo), 4)']);
workspace.Plot(4).figSurface = contour(zeros(0,0));

% sweep definition
```

```
workspace.sweep.vdX = zeros(0,0); % iX
workspace.sweep.vdY = zeros(0,0); % iY
workspace.sweep.vdZ = zeros(0,0); % iZ
workspace.sweep.vdF = zeros(0,0); % iF
workspace.sweep.acData = zeros(0,0,0,0); % iX, iY, iZ, iF


handles.workspace = workspace;
guidata(hObject, handles);
handles = MFRefreshPlotMenus(handles, 1);
handles = MFRefreshPlotMenus(handles, 2);
handles = MFRefreshPlotMenus(handles, 3);
handles = MFRefreshPlotMenus(handles, 4);
handles = MFSynchronizeWorkspace(handles, handles.workspace);
handles = MFSynchronizeAllPlots(handles);

%% MFCalculateSAF(...) prepare SAF data using handles defined algorithm
% --------------------------------------------------------------------
function [handles, bComplete] = MFCalculateSAF(handles, bShowProgress)

% Prepare (robustly) for calculation of SAF
bComplete = 0;
% copy the workspace for later abuse
workspace = handles.workspace;

if min(size(workspace.vdF)) == 0
    return;
end

if (min(size(handles.workspace.mcImg)) == 0)
    handles = MFStatusLine(handles, 'ERROR ''MFCalculate SAF'' mcImg is not defined.
Retrieve or generate data to initialize and then calculate.');
    return;
elseif (bShowProgress)
    handles = MFStatusLine(handles, 'Calculating SAF...');
end

dLambda = workspace.constant.dC_mmGHz/(workspace.vdF(workspace.iF)); % in mm
dBeta = 2*pi/dLambda;

iXSAF = max(size(workspace.vdXSAF));
iYSAF = max(size(workspace.vdYSAF));

if (bShowProgress)
    tic
end

if (iXSAF*iYSAF > 1) & bShowProgress & ~(strcmpi(handles.workspace.strCalculationMethod,
'FDSAFTBusse') | strcmpi(handles.workspace.strCalculationMethod, '3DHOLSheen')) % if the
calculation involves more than one element, produce a waitbar for the calculation
    dP = 0;
    dP_old = 0;
    dT = toc;
    dT_old = toc;
    handles.dlgWaitbar = waitbar(dP, 'Preparing for SAF Calculation...', 'Name', 'SAF
Progress Meter', 'CreateCancelBtn',
['emsaf(''MenuCancelCalculation'',gcbo,[],guidata(gcbo))']);
    guidata(handles.dlgWaitbar, handles);
end

% initialize mcSAF to zeros of proper size (iXSAF, iYSAF)
workspace.mcSAF = zeros(iXSAF, iYSAF);

% prepare for Enforce Spot Size
dXTheta =
workspace.constant.dC_mmGHz/workspace.vdF(workspace.iF)/workspace.dApertureSizeX; % mm
dYTheta =
workspace.constant.dC_mmGHz/workspace.vdF(workspace.iF)/workspace.dApertureSizeY; % mm

%% Subtract constant from original data for multiple frequency or single
% depending on method
```

```
handles = MFStatusLine(handles, ['Subtract constant ''' workspace.strSubtractConstant '''
from acData']);

if (strcmpi(handles.workspace.strCalculationMethod, '3DHolSheen') |
strcmpi(handles.workspace.strCalculationMethod, 'MFSAFTBusse') |
strcmpi(handles.workspace.strCalculationMethod, 'MFAFTYamani'))
    acData = handles.workspace.acData;

    switch (workspace.strSubtractConstant)
        case 'zero'
            vdcSubtractConstant = acData(1, 1, :)*0;
        case 'mean'
            vdcSubtractConstant = squeeze(mean(mean(acData)));
        case 'upperleft'
            vdcSubtractConstant = acData(1, size(acData, 2), :);
        case 'upperright'
            vdcSubtractConstant = acData(size(acData, 1), size(acData, 2), :);
        case 'lowerleft'
            vdcSubtractConstant = acData(1, 1, :);
        case 'lowerright'
            vdcSubtractConstant = acData(size(acData, 1), 1, :);
    end

    iFSAF = length(handles.workspace.vdF);
    for iF = 1:iFSAF
        acData(:,:,iF) = acData(:,:,iF) - vdcSubtractConstant(iF);
    end

else % single frequency subtraction

    mcImg = workspace.mcImg;

    % set image data to subtract constant
    switch (workspace.strSubtractConstant)
        case 'zero'
            dcSubtractConstant = 0;
        case 'mean'
            dcSubtractConstant = squeeze(mean(mean(mcImg)));
        case 'upperleft'
            dcSubtractConstant = mcImg(1, size(mcImg, 2));
        case 'upperright'
            dcSubtractConstant = mcImg(size(mcImg, 1), size(mcImg, 2));
        case 'lowerleft'
            dcSubtractConstant = mcImg(1, 1);
        case 'lowerright'
            dcSubtractConstant = mcImg(size(mcImg, 1), 1);
    end

    mcImg = mcImg - dcSubtractConstant;
end

%% OK, now let's calculate the SAF image
% enter switch
switch (handles.workspace.strCalculationMethod)

%% DirectSingleFrequency - Process SAF image using direct phase matching methods
    case 'DirectSingleFrequency'   % Calculate For DirectSingleFrequency
        % make (allocate) phase correction table
        [mX, mY] = ndgrid(handles.workspace.vdXImg, handles.workspace.vdYImg);

        for iX = 1:iXSAF

            if strcmpi(workspace.strEnforceSpotSize, 'off')
                for iY = 1:iYSAF
                    workspace.mcSAF(iX, iY) =
sum(sum(mcImg.*exp(2.0*(j*dBeta*sqrt((workspace.vdXSAF(iX) - mX).^2+(workspace.vdYSAF(iY)
- mY).^2+(workspace.dFocusHeight).^2)))));
                end
            else % enforce spot size mask
                for iY = 1:iYSAF
                    dXPhi = atan((mX-workspace.vdXSAF(iX))/workspace.dFocusHeight);
```

```
                    dYPhi = atan((mY-workspace.vdYSAF(iY))/workspace.dFocusHeight);
                    mMask = (dXPhi.^2/(dXTheta/2)^2 + dYPhi.^2/(dYTheta/2)^2) < 1;
                    workspace.mcSAF(iX, iY) =
sum(sum(mcImg.*mMask.*exp(2.0*(j*dBeta*sqrt((workspace.vdXSAF(iX) -
mX).^2+(workspace.vdYSAF(iY) - mY).^2+(workspace.dFocusHeight).^2)))));
                end
            end

            if (iXSAF ~= 1) & bShowProgress
                dP_old = dP;
                dT_old = dT;

                dP = (iX-1)/(iXSAF-1);
                dT = toc;

                if (dP - dP_old) ~= 0
                    dTimeRemain = (1-dP)*(dT-dT_old)/(dP-dP_old);
                    try
                        handles.dlgWaitbar = waitbar(dP, handles.dlgWaitbar,
[num2str(round(dP*100)) '% Complete... ' MFTime2Str(dTimeRemain) ' left ('
MFTime2Str(toc) ' of ' MFTime2Str(dTimeRemain+toc) ')']);
                    catch
                        handles = MFStatusLine(handles, 'Calculation canceled');
                        return;
                    end % try
                end % if
            end % if iXSAF
        end % for iX

        if (bShowProgress)
            handles = MFStatusLine(handles, ['Calculation method '
handles.workspace.strCalculationMethod ' complete at '
num2str(handles.workspace.vdF(handles.workspace.iF)) ' GHz (' MFTime2Str(toc) ')']);
        end

%% DirectSingleFrequencyExt - Process SAF image using direct phase matching methods
% - uses external function call to ExtDirectSF.dll (a Matlab MEX file)
    case 'DirectSingleFrequencyExt'   % Calculate For DirectSingleFrequency
        % make (allocate) phase correction table
        [mX, mY] = ndgrid(handles.workspace.vdXImg, handles.workspace.vdYImg);

        for iX = 1:iXSAF

            if strcmpi(workspace.strEnforceSpotSize, 'off')
                for iY = 1:iYSAF
                    workspace.mcSAF(iX, iY) =
sum(sum(mcImg.*exp(2.0*(j*dBeta*sqrt((workspace.vdXSAF(iX) - mX).^2+(workspace.vdYSAF(iY)
- mY).^2+(workspace.dFocusHeight).^2)))));
                end
            else % enforce spot size mask
                for iY = 1:iYSAF
                    dXPhi = atan((mX-workspace.vdXSAF(iX))/workspace.dFocusHeight);
                    dYPhi = atan((mY-workspace.vdYSAF(iY))/workspace.dFocusHeight);
                    mMask = (dXPhi.^2/(dXTheta/2)^2 + dYPhi.^2/(dYTheta/2)^2) < 1;
                    workspace.mcSAF(iX, iY) =
sum(sum(mcImg.*mMask.*exp(2.0*(j*dBeta*sqrt((workspace.vdXSAF(iX) -
mX).^2+(workspace.vdYSAF(iY) - mY).^2+(workspace.dFocusHeight).^2)))));
                end
            end

            if (iXSAF ~= 1) & bShowProgress
                dP_old = dP;
                dT_old = dT;

                dP = (iX-1)/(iXSAF-1);
                dT = toc;

                if (dP - dP_old) ~= 0
                    dTimeRemain = (1-dP)*(dT-dT_old)/(dP-dP_old);
                    try
```

```
                        handles.dlgWaitbar = waitbar(dP, handles.dlgWaitbar,
[num2str(round(dP*100)) '% Complete... ' MFTime2Str(dTimeRemain) ' left ('
MFTime2Str(toc) ' of ' MFTime2Str(dTimeRemain+toc) ')']);
                    catch
                        handles = MFStatusLine(handles, 'Calculation canceled');
                        return;
                    end % try
                end % if
            end % if iXSAF
        end % for iX

        if (bShowProgress)
            handles = MFStatusLine(handles, ['Calculation method '
handles.workspace.strCalculationMethod ' complete at '
num2str(handles.workspace.vdF(handles.workspace.iF)) ' GHz (' MFTime2Str(toc) ')']);
        end

%% FDSAFTBusse - Calculate SAF image using Busse's algorithm (FFT's)
% Single frequency only
    case 'FDSAFTBusse'  % Calculate For FDSAFTBusse

        vdXImg = workspace.vdXImg;
        vdYImg = workspace.vdYImg;

        [mIntermediate, vdKx, vdKy] = MFcfft2(mcImg, vdXImg, vdYImg);
        [mdKx, mdKy] = ndgrid(vdKx, vdKy);
        mIntermediate = mIntermediate .* exp(j*2.0*dBeta*workspace.dFocusHeight*sqrt(1.0
- (mdKx/(2.0*dBeta)).^2 - (mdKy/(2.0*dBeta)).^2));
        [mIntermediate, vdXImg, vdYImg] = MFcifft2(mIntermediate, vdKx, vdKy);
        workspace.vdXSAF = vdXImg;
        workspace.vdYSAF = vdYImg;
        workspace.mcSAF = mIntermediate;

        if (bShowProgress)
            handles = MFStatusLine(handles, ['Calculation method '
handles.workspace.strCalculationMethod ' complete at '
num2str(handles.workspace.vdF(handles.workspace.iF)) ' GHz (' MFTime2Str(toc) ')']);
        end

%% MFSAFTBusse - Calculate SAF image using Busse multifrequency algorithm
% It's just like FDSAFTBusse but it performs the same algorithm for all
% frequencies singly and then averages them together in the spatial
% frequency domain.
    case 'MFSAFTBusse'

        % prepare mItermediate to contain SAF data
        [vdXImg, vdYImg, mcImg] = MFSetSampling(handles, handles.workspace.dDataSampling,
handles.workspace.vdX, handles.workspace.vdY,
squeeze(handles.workspace.acData(:,:,handles.workspace.iF)));
        iFSAF = length(handles.workspace.vdF);
        mIntermediate = zeros(length(vdXImg), length(vdYImg), iFSAF);

        [mcTemp, vdKx, vdKy] = MFcfft2(mcImg, vdXImg, vdYImg);
        [mdKx, mdKy] = ndgrid(vdKx, vdKy);

        for iF = 1:iFSAF
            dLambda = workspace.constant.dC_mmGHz/workspace.vdF(iF); % in mm
            dBeta = 2*pi/dLambda;

            mIntermediate(:,:,iF) = fft2(mcImg);
            mIntermediate(:,:,iF) =
fftshift(mIntermediate(:,:,iF))/(length(vdXImg)*length(vdYImg));

            mIntermediate(:,:,iF) = mIntermediate(:,:,iF) .*
exp(j*2.0*dBeta*workspace.dFocusHeight*sqrt(1.0 - (mdKx/(2.0*dBeta)).^2 -
(mdKy/(2.0*dBeta)).^2));

            % update progress meter
            if (iFSAF ~= 1) & bShowProgress
                dP_old = dP;
                dT_old = dT;
```

```
                dP = (iF-1)/(iFSAF-1);
                dT = toc;

                if (dP - dP_old) ~= 0
                    dTimeRemain = (1-dP)*(dT-dT_old)/(dP-dP_old);
                    try
                        handles.dlgWaitbar = waitbar(dP, handles.dlgWaitbar,
[num2str(round(dP*100)) '% Complete... ' MFTime2Str(dTimeRemain) ' left ('
MFTime2Str(toc) ' of ' MFTime2Str(dTimeRemain+toc) ')']);
                    catch
                        handles = MFStatusLine(handles, 'Calculation canceled');
                        return;
                    end % try
                end % if
            end % if iFSAF

        end % for iF

        mIntermediate = squeeze(mean(mIntermediate, 3));
        mIntermediate = ifftshift(mIntermediate)*(length(vdXImg)*length(vdYImg));
        mIntermediate = ifft2(mIntermediate);
        workspace.mcSAF = mIntermediate;
        handles = MFStatusLine(handles, ['Calculation method '
handles.workspace.strCalculationMethod ' complete (' MFTime2Str(toc) ')']);

%% MFAFTYamani - compute the multi frequency auto-focusing technique derived by Ahmed
Yamani
    case 'MFAFTYamani'

        % implement MFSetSampling and place into alternate data set
        % apply ifft
        handles = MFStatusLine(handles, 'apply ifft');
        [acData, vdT] = icfft(acData, handles.workspace.vdF);

        % shift to do processing along x and y
        handles = MFStatusLine(handles, 'shift to do processing along x and y');
        acData = shiftdim(acData, 1);

        % calculate 2D fft
        handles = MFStatusLine(handles, 'calculate 2D fft');
        [acData, vdKx, vdKy] = MFcfft2(acData, vdXImg, vdYImg);
        [adKx, adKy, adT] = ndgrid(vdKx, vdKy, vdT);

        % apply back propagator
        handles = MFStatusLine(handles, 'apply back propagator');
        dF = squeeze(mean(workspace.vdF));
        dLambda = handles.workspace.constant.dC_mmGHz/dF; % in mm
        acData = acData .* exp(-i*2*pi*dF*adT.*(1-(adKx*dLambda/2).^2 -
(adKy*dLambda/2).^2));

        % shift data to do processing along t
        handles = MFStatusLine(handles, 'shift data to do processing along t');
        acData = shiftdim(acData, 2);

        %  compute fft
        handles = MFStatusLine(handles, 'compute fft');
        [acData, vdF] = cfft(acData, vdT);

        % shift data back
        handles = MFStatusLine(handles, 'shift data back');
        acData = shiftdim(acData, 1);

        % assign mcSAF to the middle frequency
        handles = MFStatusLine(handles, 'assign mcSAF to the middle frequency and
output');
        iF = round(iFSAF/2);
        mcSAF = squeeze(acData(:, :, iF));
        mcSAF = ifftshift(mcSAF, 2);
        mcSAF = ifftshift(mcSAF, 1)*(length(vdXImg)*length(vdYImg));
        mcSAF = ifft2(mcSAF);
```

```
        workspace.mcSAF = mcSAF;
        handles = MFStatusLine(handles, ['Calculation method '
handles.workspace.strCalculationMethod ' complete (' MFTime2Str(toc) ')']);

%% 3DHOLSheen - compute the 3D Holography algorithm authored by David Sheen
    case '3DHOLSheen'
        % find vdX and vdY for spatial positioning information
        vdXImg = handles.workspace.vdX;
        vdYImg = handles.workspace.vdY;

        % clear out to save RAM
        workspace.sweep.acData = [];
        workspace.acData = [];

        % implement MFSetSampling and place into alternate data set
        handles = MFStatusLine(handles, 'implement MFSetSampling and place into alternate
data set');

        % transform acData(x,y,f) to acData(kx,ky,f)
        handles = MFStatusLine(handles, 'transform x,y to kx,ky');
        % perform fft2 internally to save RAM and prevent the creation of copies
        acData = fft(fft(acData,[],2),[],1);
        % make the center of acData(kx,ky,f) correspond to kx=0, ky=0
        acData = fftshift(acData, 1);
        acData = fftshift(acData, 2);
        dL = vdXImg(2) - vdXImg(1);
        vdKx = ([0:(length(vdXImg)-1)] - ceil((length(vdXImg)-1)/2)) /
(length(vdXImg)*dL/(2*pi));
        vdKy = ([0:(length(vdYImg)-1)] - ceil((length(vdYImg)-
1)/2))/(length(vdYImg)*dL/(2*pi));

        vdF = handles.workspace.vdF;

        % resample data onto Kz rather than w (omega or 2*pi*f)
        % range of Kz is from 0 to max(dependent on z sampling)
        handles = MFStatusLine(handles, 'resample data onto Kz rather than w (omega or
2*pi*f)');
        if (workspace.dFocusHeightRange <= 0)
            errordlg('dFocusHeight cannot be < 0 for 3D Holography');
        end
        iLength = round(workspace.dFocusHeightRange/dL);
        vdKz = ([0:(iLength-1)]) / (iLength*dL/(2*pi));

        % type cast to single to save on RAM, again
        vdKx = single(vdKx);
        vdKy = single(vdKy);
        vdKz = single(vdKz);

        % I want to resample data onto K3 coordinates in preparation for FFT3
        % arrays of actual Kx, Ky, Kz
        [adKxK3, adKyK3, adKzK3] = ndgrid(vdKx, vdKy, vdKz);


        adFK3 = handles.workspace.constant.dC_mmGHz/(4*pi)*sqrt(adKxK3.^2 + adKyK3.^2 +
adKzK3.^2);
        % delete to conserve total RAM
        clear adKxK3 adKyK3 adKzK3;

        % arrays of indices of Kx, Ky, Kz
        [aiKxK3, aiKyK3, aiKzK3] = ndgrid(uint16([1:length(vdKx)]),
uint16([1:length(vdKy)]), uint16([1:length(vdKz)]));
        adFiK3 = (iFSAF-1)/(vdF(iFSAF)-vdF(1))*(adFK3 - vdF(1)) + 1;

        acDataK3 = adFK3*0;

        truth = (adFiK3 >= 1) & (adFiK3 <= iFSAF); % truth is a vector of values
        aiKxK3 = aiKxK3(truth); % actually a vector
        aiKyK3 = aiKyK3(truth); % actually a vector
        aiKzK3 = aiKzK3(truth); % actually a vector
        adFiK3 = adFiK3(truth); % actually a vector
```

```
        % delete to conserve total RAM
        clear truth;

        for iT = 1:length(aiKxK3)
            acDataK3(aiKxK3(iT), aiKyK3(iT), aiKzK3(iT)) ...
                = acData(aiKxK3(iT), aiKyK3(iT), floor(adFiK3(iT))).*(ceil(adFiK3(iT)) -
adFiK3(iT))...
                + acData(aiKxK3(iT), aiKyK3(iT), ceil(adFiK3(iT))).*(adFiK3(iT) -
floor(adFiK3(iT)))...
                + acData(aiKxK3(iT), aiKyK3(iT), round(adFiK3(iT))).*(1-
ceil(adFiK3(iT))+floor(adFiK3(iT)));
        end

        % delete to conserve total RAM
        clear acData;

        % perform FFT3 to get Hologram
        handles = MFStatusLine(handles, 'perform FFT3 to get Hologram');
        acDataK3 = ifftshift(acDataK3,1);
        acDataK3 = ifftshift(acDataK3,2);
        acDataK3 = ifftn(acDataK3);

        workspace.sweep.acData = acDataK3;
        % delete to conserve total RAM
        clear acDataK3;
        dL = 2*pi/(length(vdKx)*(vdKx(2) - vdKx(1)));
        workspace.sweep.vdX = [0:(length(vdKx)-1)]*dL;
        dL = 2*pi/(length(vdKy)*(vdKy(2) - vdKy(1)));
        workspace.sweep.vdY = [0:(length(vdKy)-1)]*dL;
        dL = 2*pi/(length(vdKz)*(vdKz(2) - vdKz(1)));
        workspace.sweep.vdZ = [0:(length(vdKz)-1)]*dL;

        % place 3D holography data as sweep
        workspace.sweep.acData = flipdim(workspace.sweep.acData,3);
        workspace.sweep.vdZ = workspace.sweep.vdZ - max(workspace.sweep.vdZ);

        % replace workspace.acData
        workspace.acData = handles.workspace.acData;

        workspace.mcSAF = zeros(length(workspace.vdXSAF),length(workspace.vdYSAF));
        handles = MFStatusLine(handles, ['Calculation method '
handles.workspace.strCalculationMethod ' complete (' MFTime2Str(toc) ')']);
        waitfor(warndlg('Data from 3D Holography Calculation stored in SWEEP.  Sweep >
Plot > Focus Height to visualize data'));
    otherwise
        errordlg(['Calculation method ' handles.workspace.strCalculationMethod ' not
recognized']);
        return;
end

%% transfer workspace
handles.workspace = workspace;
if bShowProgress
    try
        delete(handles.dlgWaitbar);
    end
end
bComplete = 1;

%% MFcfft2(...) 2D FFT that reports spatial frequency arrays
% -----------------------------------------------------------------------
function [mcZ, vdKx, vdKy] = MFcfft2(mcZ, vdX, vdY)

% optimize for memory
mcZ = fft2(mcZ);
mcZ = fftshift(mcZ, 1);
mcZ = fftshift(mcZ, 2);

dL = vdX(2) - vdX(1);
vdKx = ([0:(length(vdX)-1)] - ceil((length(vdX)-1)/2)) / (length(vdX)*dL/(2*pi));
```

```
dL = vdY(2) - vdY(1);
vdKy = ([0:(length(vdY)-1)] - ceil((length(vdY)-1)/2))/(length(vdY)*dL/(2*pi));

%% MFcifft2(...) 2D iFFT
% ------------------------------------------------------------------------
function [mcZ, vdX, vdY] = MFcifft2(mcZp, vdKx, vdKy)
mcZp = ifftshift(mcZp, 2);
mcZp = ifftshift(mcZp, 1);

mcZ = ifft2(mcZp);

dL = 2*pi/(length(vdKx)*(vdKx(2) - vdKx(1)));
vdX = [0:(length(vdKx)-1)]*dL;
dL = 2*pi/(length(vdKy)*(vdKy(2) - vdKy(1)));
vdY = [0:(length(vdKy)-1)]*dL;

% MFSyncrhonizePlot(...) Plot information to workspace
% ------------------------------------------------------------------------
function [handles] = MFSynchronizePlot(handles, dCurrentPlot)

axes(handles.workspace.Plot(dCurrentPlot).figAxes);

if strcmpi(handles.workspace.Plot(dCurrentPlot).strContent, 'orgmag') |
strcmpi(handles.workspace.Plot(dCurrentPlot).strContent, 'safmag')
    switch handles.workspace.Plot(dCurrentPlot).strMagnitudeUnit
        case 'linear'
            aContent = handles.workspace.Plot(dCurrentPlot).aContent;
            strUnit = 'linear';
        case 'log'
            aContent = log10(handles.workspace.Plot(dCurrentPlot).aContent);
            strUnit = 'log';
        case 'dB'
            aContent = 20*log10(handles.workspace.Plot(dCurrentPlot).aContent);
            strUnit = 'dB';
        otherwise
            errordlg('Magnitude unit not recognized');
    end
end

if strcmpi(handles.workspace.Plot(dCurrentPlot).strContent, 'orgphs') |
strcmpi(handles.workspace.Plot(dCurrentPlot).strContent, 'safphs')
    switch handles.workspace.Plot(dCurrentPlot).strPhaseUnit
        case 'deg180'
            aContent = handles.workspace.Plot(dCurrentPlot).aContent*180/pi;
            strUnit = 'deg';
        case 'deg360'
            aContent = handles.workspace.Plot(dCurrentPlot).aContent +
(handles.workspace.Plot(dCurrentPlot).aContent < 0)*pi;
            aContent = aContent*180/pi;
            strUnit = 'deg';
        case 'radpi'
            aContent = handles.workspace.Plot(dCurrentPlot).aContent;
            strUnit = 'rad';
        case 'rad2pi'
            aContent = handles.workspace.Plot(dCurrentPlot).aContent +
(handles.workspace.Plot(dCurrentPlot).aContent < 0)*pi;
            strUnit = 'rad';
        otherwise
            errordlg('Phase unit not recognized');
    end
end


if (min(size(handles.workspace.Plot(dCurrentPlot).aContent)) ~= 0)
    if strcmpi(handles.workspace.Plot(dCurrentPlot).strType, 'bitmap')
        handles.workspace.Plot(dCurrentPlot).figSurface =
pcolor(handles.workspace.Plot(dCurrentPlot).vdX,
handles.workspace.Plot(dCurrentPlot).vdY, aContent');
        shading('flat');
    elseif strcmpi(handles.workspace.Plot(dCurrentPlot).strType, 'surface')
```

```
        handles.workspace.Plot(dCurrentPlot).figSurface =
surf(handles.workspace.Plot(dCurrentPlot).vdX, handles.workspace.Plot(dCurrentPlot).vdY,
aContent');
        shading('interp');
    elseif strcmpi(handles.workspace.Plot(dCurrentPlot).strType, 'contour')
        handles.workspace.Plot(dCurrentPlot).figSurface =
contour(handles.workspace.Plot(dCurrentPlot).vdX,
handles.workspace.Plot(dCurrentPlot).vdY, aContent');
    end
else
    handles.workspace.Plot(dCurrentPlot).figSurface = contour(zeros(0,0));
end

if (handles.workspace.bShowPlotTitles)
    if (handles.workspace.bShowPlotUnits)
        title([handles.workspace.Plot(dCurrentPlot).strTitle ' (' strUnit ')'],
'FontSize', handles.workspace.dTitleFontSize);
    else
        title(handles.workspace.Plot(dCurrentPlot).strTitle, 'FontSize',
handles.workspace.dTitleFontSize);
    end
end

if (handles.workspace.bShowPlotAxesLabels)
    xlabel('X (mm)');
    ylabel('Y (mm)');
end

colormap(handles.workspace.Plot(dCurrentPlot).strColorMap);
guidata(handles.workspace.Plot(dCurrentPlot).figAxes, handles);
handles = MFRefreshPlotMenus(handles, dCurrentPlot);
handles = MFSynchronizeWorkspace(handles, handles.workspace);

%% MenuImportBIN_Callback(...) Import BIN (binary) file from disk
% --------------------------------------------------------------------
function MenuImportBIN_Callback(hObject, eventdata, handles)
% hObject    handle to MenuImportBIN (see GCBO)
% eventdata  reserved - to be defined in a future version of MATLAB
% handles    structure with handles and user data (see GUIDATA)

% .bin - binary file all inclusive containing all frequency information
% Input data into temporary workspace variable
workspace = handles.workspace;

handles = MFStatusLine(handles, 'Importing data file...');

% if strcmpi('', handles.workspace.strFileName)
    [workspace.strFileName, workspace.strPathName] = uigetfile({'*.bin';'*.*'}, 'Import
binary (BIN) complex data file');
% else
%     [workspace.strFileName, workspace.strPathName] =
uigetfile([handles.workspace.strPathName handles.workspace.strFileName], 'Import binary
(BIN) complex data file');
% end

if workspace.strFileName == 0
    handles = MFStatusLine(handles, 'Import data cancled');
    return;
else
    handles = MFStatusLine(handles, 'Processing data...');
end

% open data file
fidData = fopen([workspace.strPathName workspace.strFileName], 'r');

% if opening fails...
if fidData == -1
    handles = MFStatusLine(handles, 'ERROR opening data file');
    return;
end
```

```
% read in header
iXlimit = fread(fidData, 1, 'int16');
iYlimit = fread(fidData, 1, 'int16');
iFlimit = fread(fidData, 1, 'int16');
fStart = fread(fidData, 1, 'float32');
fStop = fread(fidData, 1, 'float32');

workspace.vdF = fStart + [0:(iFlimit-1)]*(fStop-fStart)/(iFlimit - 1);

% read in data
workspace.acData = single(zeros(iXlimit, iYlimit, iFlimit));

for iY = 1:iYlimit
    for iX = 1:iXlimit

        [vfReal, Count] = fread(fidData, iFlimit, 'float32');
        if (Count == 0)
            handles = MFStatusLine(handles, ['ERROR importing data file'
workspace.strFileName]);
            fclose(fidReal);
            return;
        end
        [vfImag, Count] = fread(fidData, iFlimit, 'float32');
        if (Count == 0)
            handles = MFStatusLine(handles, ['ERROR importing data file'
workspace.strFileName]);
            fclose(fidReal);
            return;
        end
        workspace.acData(iX, iY, :) = single(vfReal + j*vfImag);
    end
end

% close file
fclose(fidData);

% adjust workspace
workspace.vdX = [0:(iXlimit-1)]*workspace.dIncrX;
workspace.vdY = [0:(iYlimit-1)]*workspace.dIncrY;
workspace.iF = round(iFlimit/2);

% length(workspace.vdX)
% length(workspace.vdY)
% workspace.iF

% set default image
workspace.mcImg = squeeze(workspace.acData(:, :, workspace.iF));
% size(workspace.mcImg)
[workspace.vdXImg, workspace.vdYImg, workspace.mcImg] = MFSetSampling(handles,
workspace.dDataSampling, workspace.vdX, workspace.vdY, workspace.mcImg);
[workspace.vdXSAF, workspace.vdYSAF] = MFSetSampling(handles, workspace.dSAFSampling,
workspace.vdX, workspace.vdY);

% clear invalid SAF data
workspace.mcSAF = zeros(0,0);

% getting this far means success!!
% assign new workspace to present workspace
% handles.workspace = workspace;
workspace.strWorkspaceFileName = '';
workspace.strWorkspacePathName = '';
handles = MFSynchronizeWorkspace(handles, workspace);

handles = MFUpdateAllPlots(handles);
handles = MFStatusLine(handles, ['Import of file ' workspace.strFileName ' completed
sucessfully']);

% if Autocalc enabled, calculate
if (handles.workspace.bAutomaticallyCalculate == 1)
    handles = MFCalculateAll(handles);
else
```

```
    handles = MFStatusLine(handles, 'WARNING: Out of date');
end

%% MenuImportSCW_Callback(...) Import SCW (scanner workspace) from disk
%--------------------------------------------------------------------
function MenuImportSCW_Callback(hObject, eventdata, handles)
% hObject    handle to MenuImportSCW (see GCBO)
% eventdata  reserved - to be defined in a future version of MATLAB
% handles    structure with handles and user data (see GUIDATA)

% .mat - Scanner workspace (nonexclusive extension)

% Input data into temporary workspace variable
tempworkspace = handles.workspace;

handles = MFStatusLine(handles, 'Importing data file...');

% if strcmpi('', handles.workspace.strFileName)
    [tempworkspace.strFileName, tempworkspace.strPathName] = uigetfile({'*.mat';'*.*'},
'Import Scanner workspace (MAT) file');
% else
%     [workspace.strFileName, workspace.strPathName] =
uigetfile([handles.workspace.strPathName handles.workspace.strFileName], 'Import binary
(BIN) complex data file');
% end

if tempworkspace.strFileName == 0
    handles = MFStatusLine(handles, 'Import data cancled');
    return;
else
    handles = MFStatusLine(handles, 'Processing data...');
end

try
    % open data file
    load([tempworkspace.strPathName tempworkspace.strFileName]);
catch
    % if opening fails...
    handles = MFStatusLine(handles, 'ERROR opening data file');
    return;
end

% read in header
tempworkspace.vdX = workspace.data.scan.vdX;
tempworkspace.vdY = workspace.data.scan.vdY;
tempworkspace.vdF = workspace.data.scan.vdF;
tempworkspace.dIncrX = tempworkspace.vdX(2) - tempworkspace.vdX(1);
tempworkspace.dIncrY = tempworkspace.vdY(2) - tempworkspace.vdY(1);

tempworkspace.iF = round(length(tempworkspace.vdF)/2);

% read in data
% tempworkspace.acData = double(workspace.data.c.s11);
tempworkspace.acData = workspace.data.c.s11;

% set default image
tempworkspace.mcImg = squeeze(tempworkspace.acData(:, :, tempworkspace.iF));
% size(workspace.mcImg)
[tempworkspace.vdXImg, tempworkspace.vdYImg, tempworkspace.mcImg] =
MFSetSampling(handles, tempworkspace.dDataSampling, tempworkspace.vdX, tempworkspace.vdY,
tempworkspace.mcImg);
[tempworkspace.vdXSAF, tempworkspace.vdYSAF] = MFSetSampling(handles,
tempworkspace.dSAFSampling, tempworkspace.vdX, tempworkspace.vdY);

% clear invalid SAF data
tempworkspace.mcSAF = zeros(0,0);

% getting this far means success!!
% assign new workspace to present workspace
% handles.workspace = workspace;
tempworkspace.strWorkspaceFileName = '';
```

```
tempworkspace.strWorkspacePathName = '';
handles = MFSynchronizeWorkspace(handles, tempworkspace);

handles = MFUpdateAllPlots(handles);
handles = MFStatusLine(handles, ['Import of file ' tempworkspace.strFileName ' completed
sucessfully']);

% if Autocalc enabled, calculate
if (handles.workspace.bAutomaticallyCalculate == 1)
    handles = MFCalculateAll(handles);
else
    handles = MFStatusLine(handles, 'WARNING: Out of date');
end

%% MenuSweepPlot_Callback(...) Plot a sweep information in 3D
% --------------------------------------------------------------------
function MenuSweepPlot_Callback(hObject, eventdata, handles, strType)
% hObject    handle to MenuSweepPlotFrequencyRaw (see GCBO)
% eventdata  reserved - to be defined in a future version of MATLAB
% handles    structure with handles and user data (see GUIDATA)

switch(strType)
    case 'FocusHeight_Isosurface'
        handles = MFStatusLine(handles, 'Preparing plot...');
        sweep = handles.workspace.sweep;
        MFPlot3D(abs(sweep.acData), sweep.vdX, 'X (mm)', sweep.vdY, 'Y (mm)', sweep.vdZ,
'Z (mm)', 'isosurface');
        handles = MFStatusLine(handles, 'Result plotted');
    case 'FocusHeight_Voxel'
        handles = MFStatusLine(handles, 'Preparing plot...');
        sweep = handles.workspace.sweep;
        MFPlot3D(abs(sweep.acData), sweep.vdX, 'X (mm)', sweep.vdY, 'Y (mm)', sweep.vdZ,
'Z (mm)', 'voxel');
        handles = MFStatusLine(handles, 'Result plotted');
    case 'FocusHeight_Sliced'
        handles = MFStatusLine(handles, 'Preparing plot...');
        sweep = handles.workspace.sweep;
        MFPlot3D(abs(sweep.acData), sweep.vdX, 'X (mm)', sweep.vdY, 'Y (mm)', sweep.vdZ,
'Z (mm)', 'sliced');
        handles = MFStatusLine(handles, 'Result plotted');
    case 'FocusHeight_Layer'
        workspace = handles.workspace; % backup workspace
        handles.workspace.bShowPlotUnits = 0;
        handles.workspace.dTitleFontSize = 12;

        % add new plots to workspace
        iP = length(handles.workspace.Plot);

        if strcmp(handles.workspace.Plot(1).strContent, 'safmag')
            handles.workspace.Plot(iP+1) = handles.workspace.Plot(1);
        elseif strcmp(handles.workspace.Plot(2).strContent, 'safmag')
            handles.workspace.Plot(iP+1) = handles.workspace.Plot(2);
        elseif strcmp(handles.workspace.Plot(3).strContent, 'safmag')
            handles.workspace.Plot(iP+1) = handles.workspace.Plot(3);
        elseif strcmp(handles.workspace.Plot(4).strContent, 'safmag')
            handles.workspace.Plot(iP+1) = handles.workspace.Plot(4);
        else
            handles.workspace.Plot(iP+1) = handles.workspace.Plot(1);
            handles = MFSynchronizeWorkspace(handles, handles.workspace);
            handles = MFAssignPlot(handles, iP+1, 'safmag');
        end

        figPlot = figure;
        handles.workspace.Plot(iP+1).figAxes = gca;
        handles = MFSynchronizeWorkspace(handles, handles.workspace);

        axesText = axes('Position',[0 0 1 1],'Visible','off');
        % set(figAnimate,'EraseMode', 'background');

        %determine iZ
        vdZ = abs(handles.workspace.sweep.vdZ);
```

```
        iZ = round( (length(vdZ) - 1)/(vdZ(length(vdZ)) -
vdZ(1))*(handles.workspace.dFocusHeight - vdZ(1)) + 1 );
        if iZ > length(vdZ)
            iZ = length(vdZ);
        elseif iZ < 1
            iZ = 1;
        end

        handles.workspace.mcSAF = double(squeeze(handles.workspace.sweep.acData(:, :,
iZ)));
        handles = MFSynchronizeWorkspace(handles, handles.workspace);
        handles = MFAssignPlot(handles, iP+1, handles.workspace.Plot(iP+1).strContent);
        figPlot;
        axis equal tight;

        set(gcf,'CurrentAxes',axesText);
        text(.85,.96,['(' num2str(handles.workspace.sweep.vdZ(iZ)) ' mm)
'],'FontSize',handles.workspace.dTitleFontSize, 'BackgroundColor', get(figPlot, 'Color'),
'VerticalAlignment', 'middle', 'HorizontalAlignment', 'left');

        % restore previous workspace
        handles = MFSynchronizeWorkspace(handles, workspace);

    otherwise
        errordlg(['Sweep of type ' strType ' not recognized']);
end
colormap(handles.workspace.Plot(1).strColorMap);

%% MFPlot3D(...) put in customizations for 3D plot
% --------------------------------------------------------------------
function [] = MFPlot3D(aData, vdX, strX, vdY, strY, vdZ, strZ, strType)

switch (strType)
    case 'isosurface'
        aData = smooth3(aData);
        dMin = min(min(min(aData)));
        aData = aData - dMin;
        dMax = max(max(max(aData)));
        aData = aData / dMax;

        dZLength = size(aData, 3);
        aData = shiftdim(aData, 2);
        aDataTemp = zeros(size(aData, 1), size(aData, 3), size(aData, 2));
        for iZ = 1:dZLength
            aDataTemp(iZ, :, :) = squeeze(aData(iZ, :, :))';
        end
        aData = shiftdim(aDataTemp, 1);

        dIncr = .1;
        figure;
        set(gcf, 'Renderer', 'opengl');
        colormapsaf = colormap;
        dColorMapLength = size(colormapsaf, 1);

        h(1) = subplot(1, 2, 1);
        for dLevel = [dIncr:dIncr:1]
            p = patch(reducepatch(isosurface(vdX, vdY, vdZ, aData, dLevel), 1000),
'FaceColor', colormapsaf(round(dLevel*dColorMapLength),:), 'EdgeColor', 'none',
'FaceAlpha', .2);
        end
        axis vis3d equal tight;
        xlabel(strX);
        ylabel(strY);
        zlabel(strZ);

        h(2) = subplot(1, 2, 2);
        for dLevel = [dIncr:dIncr:1]
            p = patch(reducepatch(isosurface(vdX, vdY, vdZ, aData, dLevel), 400),
'FaceColor', colormapsaf(round(dLevel*dColorMapLength),:), 'EdgeColor', 'none',
'EraseMode', 'none');
```

```
        end
        axis vis3d equal tight;
        xlabel(strX);
        ylabel(strY);
        zlabel(strZ);

        hlink = linkprop(h,{'CameraPosition','CameraUpVector'});
        key = 'graphics_linkprop';
        % Store link object on first subplot axes
        setappdata(h(1),key,hlink);

    case 'voxel'
        figure;
        h = MFVol3D('cdata',aData,'texture','3D');
        view(3);
        % Update view since 'texture' = '2D'
        MFVol3D(h);
        alphamap('rampup');
        alphamap(.06 .* alphamap); % 0.06
        axis vis3d equal tight;
        xlabel(strX);
        ylabel(strY);
        zlabel(strZ);

    case 'sliced'

        figure;
        MFVolSlice(aData, vdX, vdY, vdZ);
        axis vis3d equal tight;
        xlabel(strX);
        ylabel(strY);
        zlabel(strZ);

    otherwise
        errordlg('MFPlot strType not recognized');
end

%% MFVolSlice(...) Plots the volumetric data by slices in x, y, z planes
% --------------------------------------------------------------------
function MFVolSlice(adC, vdX, vdY, vdZ)

% bCropZ = (-vdZ < 100) .* (-vdZ > 10);
bCropZ = 1+vdZ*0;
mTemp = adC(:,:,1)*0;

for iTemp = 1:length(vdZ)
    if (bCropZ(iTemp) == 0)
        adC(:,:,iTemp) = mTemp;
    end
end

dHighThreshold = 1;
dLowThreshold = 0;

if nargin == 1
    vdX = [0:size(adC,1)-1];
    vdY = [0:size(adC,2)-1];
    vdZ = [0:size(adC,3)-1];
    dRelSize = 1;
end

if length(vdX) > 1
    dX = vdX(2) - vdX(1);
else
    dX = 1;
end

if length(vdY) > 1
    dY = vdY(2) - vdY(1);
else
    dY = 1;
```

```
end

if length(vdZ) > 1
    dZ = vdZ(2) - vdZ(1);
else
    dZ = 1;
end

adNorm = adC;
adNorm = adNorm - min(min(min(adNorm)));
adNorm = adNorm / max(max(max(adNorm)));

if (dHighThreshold ~= 1) | (dLowThreshold ~= 0)
    adNorm = (adNorm >= dHighThreshold)*dHighThreshold + (adNorm <
dHighThreshold).*adNorm;
    adNorm = (adNorm <= dLowThreshold)*dLowThreshold + (adNorm > dLowThreshold).*adNorm;
    adNorm = adNorm - min(min(min(adNorm)));
    adNorm = adNorm / max(max(max(adNorm)));
end

adNorm = single(adNorm);
adC = uint8(adNorm*255);

dXMin = min(vdX) - dX/2;
dXMax = max(vdX) + dX/2;
dYMin = min(vdY) - dY/2;
dYMax = max(vdY) + dY/2;
dZMin = min(vdZ) - dZ/2;
dZMax = max(vdZ) + dZ/2;

dScale = 1;
dPower = 2;

hold on;

% draw X axis slices
for iI = 1:length(vdX)
    mdData = squeeze(adC(iI,:,:));
    mdAlpha = single(squeeze(adNorm(iI,:,:)).^dPower*dScale);
    h(1,iI) = surf([0,0;0,0]+vdX(iI), [dYMin,dYMin;dYMax,dYMax],
[dZMin,dZMax;dZMin,dZMax], [0,0;0,0]);

set(h(1,iI),'CData',mdData,'FaceColor','texturemap','FaceAlpha','texturemap','AlphaDataMa
pping','none','AlphaData',mdAlpha,'EdgeColor','none');
end

% draw Y axis slices
for iI = 1:length(vdY)
    mdData = squeeze(adC(:,iI,:));
    mdAlpha = single(squeeze(adNorm(:,iI,:)).^dPower*dScale);
    h(2,iI) = surf([dXMin,dXMin;dXMax,dXMax], [0,0;0,0]+vdY(iI),
[dZMin,dZMax;dZMin,dZMax],[0,0;0,0]);

set(h(2,iI),'CData',mdData,'FaceColor','texturemap','FaceAlpha','texturemap','AlphaDataMa
pping','none','AlphaData',mdAlpha,'EdgeColor','none');
end

% draw Z axis slices
for iI = 1:length(vdZ)
    mdData = squeeze(adC(:,:,iI));
    mdAlpha = single(squeeze(adNorm(:,:,iI)).^dPower*dScale);
    h(3,iI) = surf([dXMin,dXMin;dXMax,dXMax], [dYMin,dYMax;dYMin,dYMax],
[0,0;0,0]+vdZ(iI),[0,0;0,0]);

set(h(3,iI),'CData',mdData,'FaceColor','texturemap','FaceAlpha','texturemap','AlphaDataMa
pping','none','AlphaData',mdAlpha,'EdgeColor','none');
end
camproj('perspective');
```

BIBLIOGRAPHY

[1] Bois, K., A. Benally and R. Zoughi, "Microwave Near-Field Reflection Property Analysis of Concrete for Material Content Determination," *IEEE Transactions on Instrumentation and Measurement*, vol. 49, no. 1, pp. 49-55, 2000.

[2] Bois, K., A. Benally, P.S. Nowak and R. Zoughi, "Microwave Nondestructive Determination of Sand to Cement (s/c) Ratio in Mortar," *Research in Nondestructive Evaluation*, vol. 9, no. 4, pp. 227-238, 1997.

[3] Bakhtiari, S., S. Ganchev, N. Qaddoumi and R. Zoughi, "Microwave Non-Contact Examination of Disbond and Thickness Variation in Stratified Composite Media", *IEEE Transactions on Microwave Theory and Techniques*, 42, pp. 389-395, March 1994.

[4] Case, J., R. Zoughi, K. Donnell, D. Hughes, and K.E. Kurtis, "Microwave Analysis of Mortar Prepared with Type I/II, III and V Cement and Subjected to Cyclical Chloride Exposure," *Proceedings of the Twenty-eighth Annual Review of Progress in Quantitative Nondestructive Evaluation*, vol. 21, pp. 498-505, Brunswick, Maine, July 29-August 3, 2001.

[5] Bois, K., A. Benally and R. Zoughi, "Near-Field Microwave Non-Invasive Determination of NaCl in Mortar," *IEE proceedings on Science, Measurement and Technology*, vol. 148, no. 4, pp. 178-182, July 2001.

[6] Hu, C., A. Benally, T. Case, R. Zoughi and K. Kurtis, "Influence on the Near-Field Microwave Reflection Properties of Chloride in Mortar Specimens Made of Cement Types II, III and V at X- and S-Bands," *Proceedings of the SPIE'2000 Conference*, vol. 4129, pp. 31-38, San Diego, CA, 2000.

[7] Hu, C., T. Case, M. Castle, R. Zoughi and K. Kurtis, "Microwave Evaluation of Accelerated Chloride Ingress in Mortar," *Proceedings of the Twenty-seventh Annual Review of Progress in Quantitative Nondestructive Evaluation*, vol. 20A, pp. 467-473, Ames, IA, 2000.

[8] Case, J.T., S. Peer, and R. Zoughi, "Microwave Reflection Properties of Concrete Periodically Exposed to Chloride Solution of 3% Salinity and Compression Force," *IEEE Transactions on Instrumentation and Measurement*, vol. 53, no. 4, pp. 1000-1004, August 2004.

[9] Peer, S., J.T. Case, E. Gallaher, K.E. Kurtis and R. Zoughi, "Microwave reflection and Dielectric Properties of Mortar Subjected to Compression Force and Cyclically Exposed to Water and Sodium Chloride Solution," *IEEE Transactions on Instrumentation and Measurement*, vol. 52, no. 1, pp. 111-118, February 2003.

[10] R. Zoughi, S. Peer, J.T. Case, E.B. Gallaher, and K.E. Kurtis, "Microwave Near-Field Evaluation of the Effects of Cyclical Chloride Exposure and Compressive Loading on Mortar," Structural health Monitoring: The Demands and Challenges, CRC Press, 2001, pp. 575-583.

[11] Bois, K., H. Campbell, A. Benally, P.S. Nowak and R. Zoughi, "Microwave Noninvasive Detection of Grout in Masonry," *Masonry Journal*, vol. 16, no. 1, pp. 49-54, 1998.

[12] Hughes, D., N. Wang, T. Case, K. Donnell, R. Zoughi, R. Austin and M. Novack "Microwave Nondestructive Detection of Corrosion Under Thin Paint and Primer in Aluminum Panels," *Special Issue of Subsurface Sensing Technologies and Applications: on Advances and Applications in Microwave and Millimeter Wave Nondestructive Evaluation*, vol. 2, no. 4, pp. 435-451, 2001.

[13] S. Kharkovsky, F. Hepburn, J. Walker, and R. Zoughi, "Nondestructive Testing of the Space Shuttle External Tank Foam Insulation using Near-Field and Focused Millimeter Wave Techniques," *Materials Evaluation*, Vol. 63, No. 5, pp. 516-522, 2005.

[14] S. Shrestha, S. Kharkovsky, R. Zoughi, and F. Hepburn, "Microwave and Millimeter Wave Nondestructive Testing of the Space Shuttle External Tank Insulating Foam," *Materials Evaluation*, Vol. 63, No. 3, pp. 339-344, 2005.

[15] F.T. Ulaby, R.K. Moore, and A.K. Fung, "Microwave Remote Sensing, Active and Passive," Vol. II, Artech House, Norwood, MA, 1986.

[16] L.J. Busse, "Three-Dimensional Imaging Using a Frequency-Domain Synthetic Aperture Focusing Technique," *IEEE Transactions on Ultrasonics, Ferroelectrics, and Frequency Control*, Vol. 39, No. 2, pp. 174-179, March 1992.

[17] D.M. Sheen, D.L. McMakin, and T.E. Hall, "Three-Dimensional Millimeter-Wave Imaging for Concealed Weapon Detection," *IEEE Transactions on Microwave Theory and Techniques*, Vol. 49, No. 9, September 2001.

[18] J. Tuovinen, T.M. Hirvonen, and A.V. Raisanen, "Near-Field Analysis of a Thick Lens and Horn Combination: Theory and Measurements," *IEEE Transactions on Antennas and Propagation*, Vol. 40, No. 6, pp. 613-619, June 1992.

[19] S. Cornbleet, "Dielectric Corrected Plane Reflector: An Unusual Solution," *IEE Proceedings H Microwaves, Antennas and Propagation*, Vol. 136, No. 5, pp. 377-380, October 1989.

[20] T. Uckan, "Design of a Hyperbolic Microwave Metallic Lens," *Review of Scientific Instruments*, Vol. 52, No. 1, pp. 21-23, January 2001.

[21] M. Tanaka and S. Sato, "Focusing Properties of Liquid Crystal Lens Cells With Stack-Layered Structure in the Millimeter-Wave Region," *IEEE Microwave and Wireless Components Letters*, Vol. 12, No. 5, pp. 163-165, May 2002.

[22] E. Cubukcu, K. Aydin, E. Ozbay, S. Foteinopolou, and C. M. Soukoulis, "Subwavelength Resolution in a Two-Dimensional Photonic-Crystal-Based Superlens," *Physical Review Letters*, Vol. 91, No. 20, November 2003.

[23] A.A. Houck, J.B. Brock, I.L. Chuang, "Experimental Observatons of a Left-Handed Material That Obeys Snell's Law," *Physical Review Letters*, Vol. 90, No. 13, April 2003.

[24] J.B. Pendry, "Negative Refraction Makes a Perfect Lens," *Physical Review Letters*, Vol. 85, No. 18, pp. 3966–9, October 2000.

[25] J.B. Pendry and D.R. Smith, "Reversing Light : Negative Refraction," *Physics Today*, Vol. 57, No. 6, pp. 37, June 2004.

[26] F. Castro and B. Nabet, "Continuous Variation in Fresnel Lens Focal Length," *IEEE Lasers and Electro-Optics Society Annual Meeting. LEOS '94 Conference Proceedings*, Vol. 1, pp. 136-137, November 1994.

[27] W.B. Dou, "Analysis of Frequency Dependence and Focusing Performance of Diffractive Lens," *Optics Express*, Vol. 10, No. 19, pp. 1018-1027, September 2002.

[28] P.-S. Kildal and M.M. Davis, "Characterisation of Near-Field Focusing With Application to Low Altitude Beam Focusing of the Arecibo Tri-Reflector System," *IEE Proceedings on Microwaves, Antennas and Propagation*, Vol. 143, No. 4, pp. 284-292, August 1996.

[29] L. Shafai, A.A. Kishk, and A. Sebak, "Near Field Focusing of Apertures and Reflector Antennas," *IEEE WESCANEX 97: Communications, Power and Computing. Conference Proceedings*, pp. 246-251, May 1997.

[30] E. Ongareau, E. Marouby, and J.R. Levrel, "Charts for a Quick Design of Spot-Focusing Corrugated Horn Lens Antennas," *Antennas and Propagation Society International Symposium*, Vol. 2, pp. 986-989, June 1994.

[31] Y. Ishikawa, T. Tanizaki, H. Nishida, and Y. Taguchi, "60 GHz Band FM-Pulse Automotive Radar Front End Using New Type NRD Guide and Dielectric Lens Antenna," *Topical Symposium on Millimeter Waves*, pp. 155-158, July 1997.

[32] A.D. Olver and B. Philips, "Integrated Lens With Dielectric Horn Antenna," *Electronics Letters*, Vol. 29, No. 13, pp. 1150-1152, June 1993.

[33] M. Tabib-Azar, P.S. Pathak, G. Ponchak, and S. LeClair, "Nondestructive Superresolution Imaging of Defects and Nonuniformities in Metals, Semiconductors, Dielectrics, Composites, and Plants Using Evanescent Microwaves," *Review of Scientific Instruments*, Vol. 70, No. 6, pp. 2783-2792, June 1999.

[34] M. Tabib-Azar, D.P. Su, A. Pohar, S. LeClair, and G. Ponchak, "0.4μm Spatial Resolution With 1 GHz(λ=30cm) Evanescent Microwave Probe," *Review of Scientific Instruments*, Vol. 70, No.3, pp. 1725-1729, March 1999.

[35] J. Kim, K. Lee, B. Friedman, and D. Cha, "Near-Field Scanning Microwave Microscope Using a Dielectric Resonator," *Applied Physics Letters*, Vol. 83, No. 5, pp. 1032-1034, August 2003.

[36] N. Karnik, B.P. Kumar, and G.R. Branner, "Conformal K-band 5 Element Waveguide Array for Near-Field Applications," *IEEE Antennas and Propagation Society International Symposium*, Vol. 1, pp. 266-269, July 2001.

[37] C.-C. Chang, C. Liang, B. Deng, C.W. Domier, N.C. Luhmann Jr., Hyeon Park, and T. Munsat, "A Millimeter Wave Beam Shaping Phased Antenna Array," *Proceedings of the 3rd Int. Conference on Microwave and Millimeter Wave Technology*, pp. 11-16, August 2002.

[38] L. Huang, J.-C. Chiao, and M.P. De Lisio, "An Electronically Switchable Leaky Wave Antenna," *IEEE Transactions on Antennas and Propagation*, Vol. 48, No. 11, pp. 1769-1772, November 2000.

[39] Y.J. Kim, L. Jofre, F. De Flaviis, and M.Q. Feng, "Microwave Reflection Tomography Array for Damage Detection in Concrete Structures," *IEEE MTT-S International Microwave Symposium Digest*, Vol. 2, pp. 651-654, June 2002.

[40] M. Bogosanovic and A.G. Williamson, "Antenna Array with Beam Focused in Near-Field Zone," *Electronics Letters*, Vol. 39, No. 9, pp. 704-705, May 2003.

[41] R. Benjamin, I.J. Craddock, G.S. Hilton, S. Litobarski, E. McCutcheon, R. Nilavalan, and G.N. Crisp, "Microwave Detection of Buried Mines Using Noncontact, Synthetic Near-Field Focusing," *Radar, Sonar and Navigation, IEE Proceedings*, Vol. 148, No. 4, pp. 233-240, August 2001.

[42] R. Ludwig and D. Roberti, "A Nondestructive Ultrasonic Imaging System for Detection of Flaws in Metal Blocks," *IEEE Transactions on Instrumentation and Measurement*, Vol. 38, No. 1, pp. 113-118, February 1989.

[43] K. McClatchey, M.T. Reiten, and R.A, Cheville, "Time Resolved Synthetic Aperture Terahertz Impulse Imaging," *Applied Physics Letters*, Vol. 79, No. 27, pp. 4485-4487, December 2001.

[44] W.J. Graham, "Focused Synthetic Phased Array for Subsurface Imaging," *IEEE Antennas and Propagation Society International Symposium*, Vol. 2, pp. 986-989, June 1998.

[45] M.S. D'Errico, B.L. Douglas, and H. Lee, "Subsurface Microwave Imaging for Nondestructive Evaluation of Civil Structures," *IEEE International Conference on Acoustics, Speech, and Signal Processing (ICASSP-93)*, Vol. 5, pp. 453-456, April 1993.

[46] I.L. Morrow and P. van Genderen, "Effective Imaging of Buried Dielectric Objects," *IEEE Transactions on Geoscience and Remote Sensing*, Vol. 40, No. 4, pp. 943-949, April 2002.

[47] T.-H. Chu, N.H. Farhat, "Frequency-Swept Microwave Imaging of Dielectric Objects," *IEEE Transactions on Microwave Theory and Techniques*, Vol. 36, No. 3, pp. 489-493, March 1998.

[48] D.A. Hill, "Electromagnetic Scattering by Buried Objects of Low Contrast," *IEEE Transactions on Geoscience and Remote Sensing*, Vol. 26, No. 2, pp. 195-203, March 1988.

[49] N. Osumi and, K. Ueno, "Microwave Holographic Imaging Method with Improved Resolution," *IEEE Transactions on Antennas and Propagation*, Vol. 32, No. 10, pp. 1018-1026, October 1984.

[50] M.G. Guler and E.B. Joy, "High Resolution Spherical Microwave Holography," *IEEE Transactions on Antennas and Propagation*, Vol. 43, No. 5, pp. 464-472, May 1995.

[51] *Columbia Accident Investigation Board Report*, NASA, August 2003.

[52] A. Yamani, "Three-Dimensional Imaging Using a New Synthetic Aperture Focusing Technique," *IEEE Transactions on Ultrasonics, Ferroelectrics, and Frequency Control*, Vol. 44, No. 4, July 1997.

[53] K. Bois, L. Handjojo, A. Benally, K. Mubarak, and R. Zoughi, "Dielectric Plug-Loaded Two-Port Transmission Line Measurement Technique for Dielectric Property Characterization of Granular and Liquid Materials," *IEEE Transactions on Instrumentation and Measurement*, Vol. 48, No. 6, pp. 1141-1148, December 1999.

[54] J.W. Goodman, *Introduction to Fourier Optics*, New York: McGraw-Hill, 1968.

[55] C.A. Balanis, *Antenna Theory: Analysis and Design*, 2nd Ed., John Wiley & Sons, Inc., New York, 1997.

VITA

Joseph Tobias Case, a.k.a. Toby, was born in [redacted] along with his twin brother Gabe to two happy parents, John and Barbara Case. He graduated from Edward S. Marcus High School in Flower Mound, Texas in 1998. After attending Northern Arizona University in Flagstaff, Arizona in good standing for one year, life led him to Colorado State University in Fort Collins, Colorado where he began work in the Applied Microwave Nondestructive Testing Laboratory (*amntl*) in fall 1999. In January 2001, life led Dr. Reza Zoughi, the director of the *amntl*, to the University of Missouri-Rolla, and Toby followed suit. He received dual bachelors degrees from the University of Missouri-Rolla in Electrical Engineering and Physics and a minor in Mathematics in December 2003.

Toby began his graduate studies in January 2004 at the University of Missouri-Rolla. For the first semester he was a Graduate Teaching Assistant for the Electromagnetics Laboratory course. Later he received an award for his efforts titled the Outstanding Graduate Teaching Assistant of the Year by the UMR Parent's Association. For the summer of 2004 and the eight months beginning January 2005, Toby helped begin to build a microwave nondestructive evaluation lab at the NASA Marshall Space Flight Center in Huntsville, AL.

Toby Case received his MS in Electrical Engineering in May 2006.